



TECHNICAL REPORT 0-6878-4
TXDOT PROJECT NUMBER 0-6878

Development of a Three-Dimensional Laser Scanning Prototype for Pavement Preservation Applications

Sareh Kouchaki
Hossein Roshani
Yorguo G. El Hachem
Joaquin Bernardo Hernandez
Jorge A. Prozzi

August 2018; Published August 2019

<http://library.ctr.utexas.edu/ctr-publications/0-6878-4.pdf>



Technical Report Documentation Page

1. Report No. FHWA/TX-19/0-6878-4		2. Government Accession No.		3. Recipient's Catalog No.	
4. Title and Subtitle Development of a Three-Dimensional Laser Scanning Prototype for Pavement Preservation Applications				5. Report Date August 2018; Published August 2019	
				6. Performing Organization Code	
7. Author(s) Sareh Kouchaki, Hossein Roshani, Yorguo G. El Hachem, Joaquin Bernardo Hernandez, and Jorge A. Prozzi				8. Performing Organization Report No. 0-6878-4	
9. Performing Organization Name and Address Center for Transportation Research The University of Texas at Austin 3925 W. Braker Lane, 4 th Floor Austin, TX 78759				10. Work Unit No. (TRAIS)	
				11. Contract or Grant No. 0-6878	
12. Sponsoring Agency Name and Address Texas Department of Transportation Research and Technology Implementation Office P.O. Box 5080 Austin, TX 78763-5080				13. Type of Report and Period Covered Technical Report	
				14. Sponsoring Agency Code	
15. Supplementary Notes Project performed in cooperation with the Texas Department of Transportation and the Federal Highway Administration.					
16. Abstract The connection between the pavement friction and surface macro- and micro-texture makes pavement texture a vital topic for highway agencies and state Departments of Transportation to address. Accordingly, measuring surface texture is of prime importance in pavement preservation applications. Currently, most highway agencies rely on subjective measuring methods of pavement texture that are not reliable. With the recent advancements in laser technologies, highway agencies are gearing towards employing such developments that could potentially contribute towards better pavement surface texture characterization. With better surface texture characterization, they can better assess, monitor, and improve the pavement texture to provide better skid resistance for their highway network with the aim of ensuring safer roads for the public. This report proposes a laser scanning prototype for the characterization of the micro- and macro-texture of road surfaces. This prototype system has the advantage of capturing 3D data on pavement surfaces using an automatic, simple, and quick operation. This prototype is able to work in laboratory and in field. The development stages of this prototype are provided in this report. In addition, this report discusses different applications of the prototype created. The findings of this research are provided in three parts. Part I involves the feasibility of the prototype in characterizing the micro-texture of aggregates. Part II involves developing an algorithm to measure the mean texture depth of pavement surfaces. Part III involves finding the connection between the pavement friction and texture. Other applications of this prototype are in chip seal design. The results study and findings regarding the chip seal design are provided in the appendix.					
17. Key Words Friction, Micro-texture, Line Laser Scanner, Discrete Fourier Transform, Power Spectral Density, Root Mean Square Roughness, Depth of Surface Smoothness				18. Distribution Statement No restrictions. This document is available to the public through the National Technical Information Service, Springfield, Virginia 22161; www.ntis.gov.	
19. Security Classif. (of report) Unclassified		20. Security Classif. (of this page) Unclassified		21. No. of pages 102	
				22. Price	



**THE UNIVERSITY OF TEXAS AT AUSTIN
CENTER FOR TRANSPORTATION RESEARCH**

Development of a Three-Dimensional Laser Scanning Prototype for Pavement Preservation Applications

Sareh Kouchaki
Hossein Roshani
Yorguo G. El Hachem
Joaquin Bernardo Hernandez
Jorge A Prozzi

CTR Technical Report:	0-6878-4
Report Date:	August 2018; Published August 2019
Project:	0-6878
Project Title:	Accelerating Innovation in Partnered Pavement Preservation
Sponsoring Agency:	Texas Department of Transportation
Performing Agency:	Center for Transportation Research at The University of Texas at Austin

Project performed in cooperation with the Texas Department of Transportation and the Federal Highway Administration.

Center for Transportation Research
The University of Texas at Austin
3925 W. Braker Lane, 4th Floor
Austin, TX 78759

<http://ctr.utexas.edu/>

Disclaimers

Author's Disclaimer: The contents of this report reflect the views of the authors, who are responsible for the facts and the accuracy of the data presented herein. The contents do not necessarily reflect the official view or policies of the Federal Highway Administration or the Texas Department of Transportation (TxDOT). This report does not constitute a standard, specification, or regulation.

Patent Disclaimer: There was no invention or discovery conceived or first actually reduced to practice in the course of or under this contract, including any art, method, process, machine manufacture, design or composition of matter, or any new useful improvement thereof, or any variety of plant, which is or may be patentable under the patent laws of the United States of America or any foreign country.

Notice: The United States Government and the State of Texas do not endorse products or manufacturers. If trade or manufacturers' names appear herein, it is solely because they are considered essential to the object of this report.

Engineering Disclaimer

NOT INTENDED FOR CONSTRUCTION, BIDDING, OR PERMIT PURPOSES.

Research Supervisor: Dr. Jorge Prozzi

Acknowledgments

The authors express appreciation to the TxDOT Project Director, members of the Project Monitoring Committee and personnel from the Maintenance and Construction Divisions and the Austin, Bryan, Houston, San Antonio and Waco Districts for their valuable contribution during field testing.

Table of Contents

Chapter 1. Introduction	1
1.1 Pavement Skid Resistance and Texture	1
1.2 Measuring Pavement Texture	3
1.3 The Need for Objective Quantitative Methods	4
1.4 Previous Studies on Developing Micro-Texture Measurement.....	5
1.5 Previous Studies on Developing Macro-Texture Measurement	6
1.6 Research Goal and Objectives	7
1.7 Report Organization.....	8
Chapter 2. Development of the Scanner Prototype	9
2.1 Introduction.....	9
2.2 Line Laser Scanner Prototype.....	9
2.3 The LLS Range of Measurement.....	10
2.4 Block Measurement	12
2.5 Scanning Interval	14
2.6 LabVIEW Program	15
2.6.1 Linear Laser Scanner (LLS).....	15
2.6.2 Translation Stage	17
2.6.3 User Interface.....	18
2.7 Repeatability of the LLS.....	18
2.8 Tilt and Error Issues.....	19
2.8.1 Background Color and Ambient Light	20
2.8.2 Adjusting the Settings of LJ-Navigator 2	22
2.8.3 Test #1.....	22
2.8.4 Test #2.....	23
2.8.5 Test #3.....	25
2.8.6 Test #4.....	26
2.9 Combining Two Scan Datasets.....	27
Chapter 3. Investigating the Aggregate Texture.....	29
3.1 Introduction.....	29
3.2 Material Preparation and Data Collection	29
3.3 Numerical Methods.....	31
3.3.1 Continuous and Discrete Signals	32
3.3.2 Analog and Digital Signals	32
3.3.3 Fourier Transform.....	34
3.3.4 Discrete Fourier Transforms (DFT).....	35
3.3.5 Power Spectral Density (PSD).....	35
3.3.6 Root Mean Square Roughness and Depth of Surface Smoothness.....	36
3.4 Result and Discussion.....	36
3.4.1 Effect of Orientation	36
3.4.2 Comparison of PSD Results.....	37
3.4.3 Paired t-test	38
3.4.4 Evaluation of Root Mean Square Roughness and Depth of Surface Smoothness.....	39

Chapter 4. An Automatic Method for Measuring Pavement Macro-Texture	43
4.1 Introduction.....	43
4.2 Research Methodology	43
4.2.1 Field-Data Collection.....	43
4.2.2 Sand Patch Test Computer Simulation	44
4.3 Results and Discussions.....	47
4.3.1 Variability of the SPT	47
4.3.2 Finding the Reference Plane	51
4.3.3 Repeatability of the Developed MTD Prototype versus the SPT	52
Chapter 5. Pavement Friction and Texture Correlation.....	53
5.1 Introduction.....	53
5.1.1 Measurement of Skid Resistance	53
5.1.2 Measurement of Pavement Surface Texture	57
5.2 Data Collection	58
5.3 Results and Discussions.....	60
5.3.1 Repeatability of Developed LLS Prototype	60
5.3.2 Grip-Tester Results	61
5.3.3 Relationship between the Texture and Friction	64
Chapter 6. Summary and Conclusions	66
6.1 Part 1: Aggregate Texture Measurement	66
6.2 Part 2: An Automatic Method for Measuring Pavement Macro-Texture.....	67
6.3 Part 3: Correlation between Pavement Texture and Friction.....	67
References	69
Appendix A: Enhancing Chip Seal Design Using the LLS Prototype	74

List of Figures

Figure 1.1 The effect of texture on the coefficient of friction with varying velocity (Hogervorst, 1974).....	3
Figure 1.2 SPT demonstration and equipment (Chamberlin and Amsler, 1982).....	4
Figure 1.3 Schematic representation of the MTD calculation (a) utilized in the ARAN software, (b) developed by Hao et al., 2015	7
Figure 2.1 a) The triangulation system of a laser, and b) the prototype including the frame and mounted laser	10
Figure 2.2 The LLS Measurement Range in X and Z-direction	11
Figure 2.3 Schematic of laser’s scan area	11
Figure 2.4 Gage block placement in laser’s scanning line.....	13
Figure 2.5 Laser’s LabVIEW process flowchart	17
Figure 2.6 User interface of LLS program.....	18
Figure 2.7 Height profile of aggregate along y-direction (top), and corresponding standard deviation (bottom)	19
Figure 2.8 a) Unfiltered 3D scan of an aggregate, b) 3D scan of an aggregate after removing the errors at the edges, c) unfiltered 3D scan of a pavement surface, and d) 3D scan of a pavement surface after removing the errors at the edges	20
Figure 2.9 Spectral range of light (http://karnikakapoor.blogspot.com/2016/04/weirdness-colour-spectrum.html).....	21
Figure 2.10 Using different background colors in measurement.....	21
Figure 2.11 a) Scanning an aggregate from left to right, b) X-Y view of the scanned aggregate, c) Scanning an aggregate from right to left, d) X-Y view of the scanned aggregate	23
Figure 2.12 Three interpolation modes in the LJ-Navigator 2.....	24
Figure 2.13 Comparing one X-direction profile of aggregate surface in dead zone and invalid modes	26
Figure 2.14 Comparing one Y-direction profile of aggregate surface in different processing time	27
Figure 2.15 Metal plate	28
Figure 2.16 Black and white view of the first scan, second scan, and the two datasets on top of each other.....	28
Figure 3.1 Aggregate particles	30

Figure 3.2 Microscopic view of texture surfaces of a) “intensity” of aggregate A, b) “intensity” of aggregate B, c) “range” of aggregate A, and d) “range” of aggregate B	30
Figure 3.3 Graphical example of (a) continuous- and (b) discrete-time signals (Hsu, 1995).....	32
Figure 3.4 Example of analog and digital sampling (Alazartech)	33
Figure 3.5 Example of a periodic continuous signal (Hsu, 1995)	33
Figure 3.6 A non-periodic (top) and a periodic signal (bottom) (Hsu, 1995).....	34
Figure 3.7 Scan of A1 in different angles a) 0°, b) 90°, c) 180°, and d) 270°	37
Figure 3.8 PSD of Aggregate A1 in different angles.....	37
Figure 3.9 Comparison of PSD values of all aggregates	38
Figure 3.10 The profile of aggregate A1 with the micro-scale filtered profile.....	40
Figure 3.11 Root mean square roughness values in different sub-bands of wavelengths	41
Figure 3.12 Values of depth of surface smoothness in different sub-bands of wavelengths.....	41
Table 4.1 Selected Test Locations	43
Figure 4.1 3D Laser scanner and sand patch test.....	44
Figure 4.2 Laser measurement data a) before and b) after the filtering process.....	44
Figure 4.3 Schematic representation of a) the area of the sand patch on a pavement and b) the fitted rectangle on the corresponding 3D pavement model, and c) the data within the rectangle.....	45
Figure 4.4 3D representation of the uniform, horizontal plane intersecting the pavement model at 50th, 99th, and 100th percentiles and 2D view of the simulated area between the crossing plane and the lower data points filled by sand	46
Figure 4.5 Box plots of the measured diameters by the different operators on two sections.....	48
Table 4.2 ANOVA Outputs of the Sand Patch Measurements.....	50
Table 4.3 MTD Values	51
TABLE 4.4 Repeatability Analysis Results.....	52
Table 5.1 Comparison of the LFC Measuring Devices (Descornet et al., 2006; Do and Roe, 2008; Andriejauskas et al., 2014).....	54
Figure 5.1 a) The Grip-Tester attached to a vehicle, b) bottom view of the DFT, and c) the DFT connected to a water tank and DCC measuring the friction at the lane center path.....	57
Figure 5.2 a) The CTM powered by a battery measuring the texture at the right wheel path, and b) bottom view of the CTM.....	58
Figure 5.3 Graphical illustration of MPD calculation (ASTM E1845)	58
Figure 5.4 Illustration of test section and test location	59

Figure 5.5 a) Comparison of mean MPD values obtained from developed LLS prototype and CTM, b) Standard deviation of MPD values measured by developed LLS prototype and CTM at six test sections.....	61
Figure 5.6 Correlation between GN and DFT values at two speeds of 50 and 70 km/h	63
Figure 5.7 Plotted texture-friction data points including GN, DFT values, and MPD value	65
Figure A.1 a) ALD machine developed in South Africa, b) Jackson ALD nomograph.....	76
Figure A.2 LD values of a particle at different orientations	79
Figure A.3 a) 100 particles spread in the developed LLS prototype scanning area, and b) making measurement using a caliper	80
Figure A.4 Plot of LD values of 100 particles captured by the developed LLS prototype and digital caliper.....	80
Figure A.5 Change in the proportion of voids with time.....	81
Figure A.6 Voids in the chip seal structure.....	83
Figure A.7 a) Scanned surface b) Raw data c) Filtered data d) De-trended surface e) Surface with reference plane f) 2D view of the surface texture voids in one square	85
Figure A.8 Simulated texture voids filled by binder up to four different reference planes	88

List of Tables

Table 2. 1 Scanning Interval for Varying Gage Blocks.....	12
Table 2.2 Scanning Interval for a 5.0 mm Gage Block at Varying Locations.....	14
Table 2. 3 Results of Test #2, Dead Zone and Interpolation Modes	25
Table 3. 1 Aggregates Properties (BRSQC, 2016)	31
Table 3. 2 Sub-bands of Classification of Wavelengths	39
Table 3. 3 Side-by-side Comparison of Texture Parameters in Different Wavelength Ranges.....	42
Table A.1 Common Aggregate Gradations for Texas Chip Seal (TxDOT, 1995)	77
Table A.2 Side-by-Side Comparison of the Measurement Results of LLS and Digital Caliper.....	78
Table A.3 Volume of voids in existing surface textures.....	87

Chapter 1. Introduction

1.1. Pavement Skid Resistance and Texture

According to the Federal Highway Administration, in 2015 there were 18,695 fatalities in the United States resulting from roadway departure. Poor roadway conditions, especially due to wet weather, have been identified as a major contributing factor in roadway accidents. A vehicle's loss of traction on wet pavements, and the poor visibility resulting from splash-and-spray, stem from the pavement having inadequate cross-slope and surface texture. Skidding alone contributes to 15 to 35% of accidents that occur under wet conditions (Hoerner and Smith, 2002). Tire-pavement interaction therefore dictates the safety of motorists. The direct force developed in the tire-pavement interface is known as *skid resistance*, which is defined by the properties of the tire, the vehicle speed, and the pavement condition and texture. Pavement texture determines the resistance of the pavement surface to a vehicle sliding and skidding (Asi, 2007; Wang and Wang, 2013). The extent of skid resistance on any given pavement is dependent on the design of the surface texture, specifically its micro- and macro-texture, as this can affect the skid resistance, splash-and-spray, rolling resistance, and tire wear (Henry, 2000). Pavement design can therefore adjust surface pavement properties to provide the safety needed (Hoerner and Smith, 2002).

Pavement surface texture is influenced by many factors, such as aggregate type and size, mixture gradation, and texture orientation, among others. By definition, pavement texture is the result of the deviations of the surface layer from an actual planar surface (ASTM E867). The World Road Association has categorized pavement texture by its range of wavelengths (λ) and amplitudes (A). The standard specification organizations, such as the American Society for Testing Materials (ASTM E867), International Organization for Standardization (ISO 13473-1), and German Institute for Standardization (DIN on ISO 13473-1), have accepted and incorporated these definitions. The ISO 13473-1 refined the terms incorporating typical amplitudes (Sandberg, 1998) as follows:

- Micro-texture ($\lambda < 0.5$ mm, $A = 1$ to 500 μm) (where λ is wavelength and A is amplitude)
- Macro-texture (0.5 mm $< \lambda < 50$ mm, $A = 0.1$ to 20 mm)
- Mega-texture (50 mm $< \lambda < 500$ mm, $A = 0.1$ to 50 mm)

Micro-texture refers to the small-scale texture of the aggregate surface, which controls the contact between the tire rubber and the pavement surface. Micro-texture is a function of aggregate particle mineralogy, petrology, and source (natural or manufactured), and is affected by environmental effects and the action of traffic (Kogbara et al., 2016). *Macro-texture* refers to the large-scale texture of the pavement surface due to the aggregate particle size and arrangement. In asphalt pavements, the mixture properties (aggregate shape, size, and gradation), which define the type of mixture, control the macro-texture (Hall et al., 2009). Macro-texture provides drainage paths for

water entrapped between the pavement surface and tire imprint. Therefore, it controls the thickness of the water film on the pavement surface, and therefore the potential of hydroplaning (Huang, 2003). *Mega-texture* has wavelengths in the same order of size as the tire/pavement interface. Examples of mega-texture include ruts, potholes, and major joints and cracks. These affect vibration in the tire walls but not the vehicle suspension, and therefore are strongly associated with noise and rolling resistance (Hall et al., 2009). Mega-texture is out of the scope of the current study.

Pavement friction is the result of a complex interplay between two principal frictional force components: adhesion and hysteresis. Although there are other components of pavement friction, such as tire rubber shear, they are insignificant when compared to the adhesion and hysteresis force components (Henry, 2000; Hall et al., 2009). Thus, friction can be viewed as the sum of adhesion and hysteresis. *Adhesion* is the friction that results from the small-scale bonding/interlocking of the vehicle tire rubber and the pavement surface. It is a function of the interface shear strength and contact area (Hall et al., 2009; Gunaratne et al., 2000). The *hysteresis* component of the frictional forces results from the energy loss created within the tire as it responds to the texture. Because the adhesion force is developed at the tire-pavement interface, it is most responsive to the micro-level asperities (micro-texture) of the aggregate particles. In contrast, the hysteresis force developed within the tire is most responsive to the macro-level asperities (macro-texture) formed in the pavement surface (Henry, 2000; Hall et al., 2009).

According to Hogervorst both the macro and micro-texture of the pavement surface affect the skid resistance changes with vehicle speed. Figure 1.1 illustrates the effect of micro-texture and macro-texture in defining the magnitude and the rate of change of skid with velocity. The micro-texture defines the magnitude of skid resistance, and macro-texture controls the slope of reduction of skid resistance as speed increases. Macro-texture contributes to reducing the friction-speed gradient and helping mitigate the effects of water by providing drainage paths for water on pavements at high speed, but it has little effect at low speed. On the other hand, the dominant factor at low speeds that defines the level of friction is micro-texture (Hogervorst, 1974).

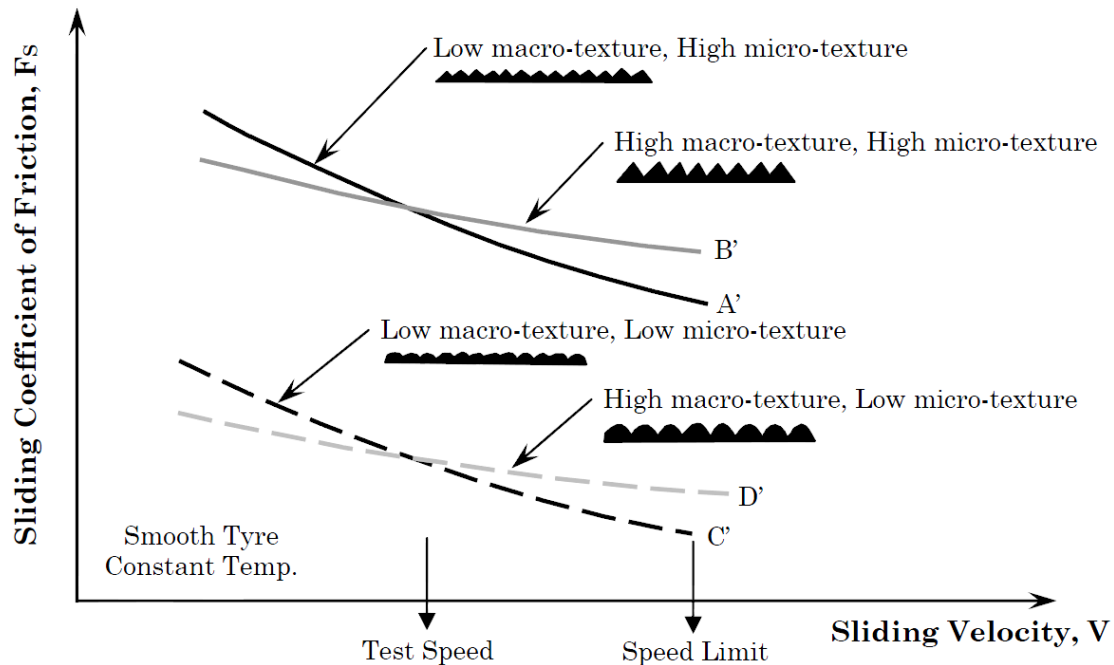


Figure 1.1 The effect of texture on the coefficient of friction with varying velocity (Hogervorst, 1974)

1.2. Measuring Pavement Texture

The connection between the pavement friction and surface macro- and micro-texture makes pavement texture a vital topic for highway agencies and state Departments of Transportation (DOTs) to address; pavement texture issues are of particular importance in wet conditions. Accordingly, measuring surface texture is of prime importance in pavement preservation applications.

Measuring Micro-texture

Currently, there is no direct method to measure the full range of the pavement micro-texture in the field. Highway agencies mainly use the indirect measurement techniques related to low slip speed friction, such as the British Pendulum Testet (BPT) and Dynamic Friction Tester (DFT), to estimate the micro-texture level of the constructed pavements (Flintsch et al., 2003).

Measuring Macro-texture

In order to measure the adequacy of the pavement macro-texture, most of highway agencies rely on the sand patch test (SPT). This test (Figure 1.2) consists of circularly spreading a volume, not less than 25 ml, of dry, uniformly-graded, fine sand on the pavement surface. Without applying pressure, a small hand-held spreading tool is used to circularly spread the sand. Four different diameters are measured along different axes, 45° apart. As expressed in Equation 1.1, the mean texture depth (MTD) is calculated using the bulk sand volume (V) and the average diameter (D) of the circular sand patch. The results of the test can be used to assess the adequacy of the surface

texture compared to the required specifications and improve construction practices, where required.

$$\text{MTD} = \frac{V}{\frac{\pi D^2}{4}} \quad \text{Equation 1.1}$$

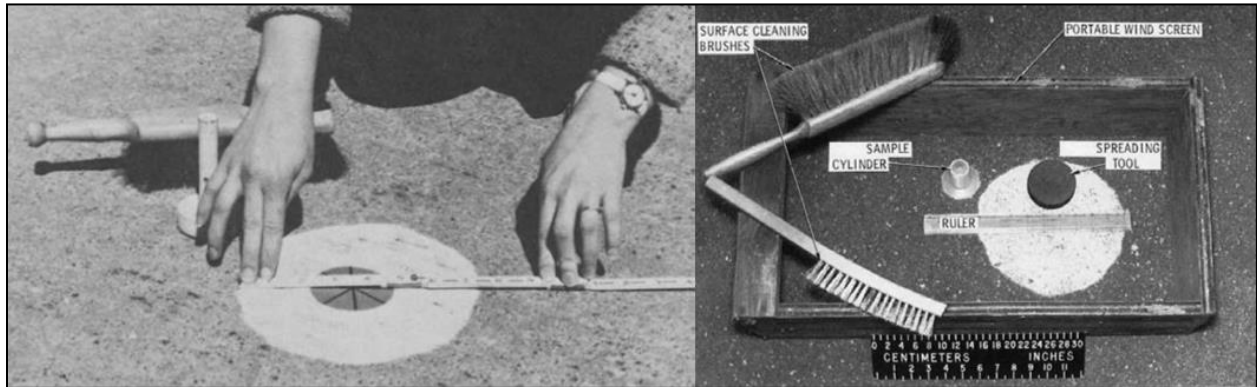


Figure 1.2 SPT demonstration and equipment (Chamberlin and Amsler, 1982)

Although the SPT is relatively simple and inexpensive, this test is subject to human errors and is affected by low repeatability and reproducibility. The errors mainly arise from volume and diameter measurements. In addition, this test relies on the operator's ability to spread the material into a circular patch. Operator error could result in a circle that overestimates the area formed by sand and underestimates the MTD. Furthermore, the SPT can be affected by wind, as losing sand throughout the testing process can skew the results and likewise overestimate the available texture. In addition, several research studies (Chamberlin and Amsler, 1982; Rose, 1975) have shown that the SPT is operator-dependent and subjective, and no two operators will have the same sand spread. One operator may also conduct the test differently at any time. If the factors promoting human error can be eliminated from the MTD measurements, the reliability of the results would improve tremendously and hence the decisions taken based on them.

1.3. The Need for Objective Quantitative Methods

Characterizing pavement texture is valuable for transportation agencies and engineers to provide proper pavement maintenance and better design of pavement mixtures. It can decrease the costs of maintenance and most importantly, the rate of accidents. However, the challenge in studying the pavement texture lies in the lack of a proper method for measuring micro-texture and using subjective methods for measuring pavement macro-texture.

With the advancement recently in both the digital image processing on one hand and the laser technologies on the other hand, state highway agencies, DOTs, and research institutes are gearing towards improving and employing such developments that could potentially contribute towards better pavement surface texture characterization. With better surface texture characterization, stakeholders can better assess, monitor, and improve the pavement texture to provide better skid

resistance for their highway network with the aim of ensuring and providing safer roads for the public.

1.4. Previous Studies on Developing Micro-Texture Measurement

Pavement surface micro-texture closely relates to the type of aggregate particles used in the pavement surface mixture; hence, texture properties of aggregate particles could predetermine the level of the pavement micro-texture. Aggregate texture measurement is one of the challenges the highway engineers deal with to ensure adequate skid resistance and safety for travelers. Motivated by advances in sensor and imaging technologies as well as signal processing techniques, several techniques have been developed to quantify the texture properties of aggregates (Slimane et al., 2008; Wang et al., 2017; Cafiso and Taormina, 2007; Masad, 2003; Anochie-Boateng et al., 2013).

Fourier transform (FT) analysis and power spectral density (PSD) analysis are the commonly used signal processing methods to evaluate aggregates surface texture. Fourier analysis provides an alternative representation of a waveform in which its frequency components can be observed and analyzed. According to the Fourier theory, all signals, whether real or arbitrary, can be represented as the sum of sinusoidal waves of various amplitudes and frequencies. The FT helps to find the amplitudes and frequencies of these constituent sinusoids. The surface roughness power spectrum, or PSD, can be derived using the FT from the measured height profile, which is the most important parameter of randomly rough surfaces.

In 2008, Slimane et al. in France sought to develop a new method to measure and characterize road surface micro-texture using image analysis. The PSD of the high-frequency information obtained from surface cartography was studied. The PSD values were normalized and the aggregate surfaces were compared considering the PSD's standard deviation. The researchers then successfully used a combined method of geometric and frequential criteria to find a meaningful relationship between friction values and roughness descriptions (Slimane et al., 2008). Researchers at the RWTH Aachen University in Germany (Wang et al., 2017) used Fourier transformation to convert the surface texture information of the aggregates to a spatial frequency domain in order to investigate the wearing behavior of the aggregates. The two-dimensional PSD (2D-PSD) was calculated before and after a polishing test to evaluate the surface roughness and the texture changes. Comparing 2D-PSD values indicated that the polishing test affects surface texture only at very short wavelengths (below 62.8 micrometer).

Cafiso and Taormina used the average of PSD values for an aggregate sample to define a specific PSD characteristic of that sample. The results showed that this average value was reliable and operationally simple. The researchers believed that a graphic comparison between the PSD curves was insufficient to investigate the behavior of different types of aggregates during polishing tests due to a lack of quantitative evaluation. Hence, additional parameters were introduced and used to appraise the position and form of PSD curves (Cafiso and Taormina, 2007). Those parameters included the area under the PSD function that represents the mean-square roughness of the

pavement; signal energy; slope of the straight-line regression of the PSD function; and PSD index obtained by modal assurance criterion parameter.

1.5. Previous Studies on Developing Macro-Texture Measurement

In recent years, the use of laser scanning techniques in engineering surveys has gained increasing interest due to the advantages of being non-contact, operator-independent, rapid, and highly accurate (Serigos et al., 2014; Wang et al., 2011). Accordingly, several attempts have been made to replace the traditional macro-texture measurement technique, the SPT, with laser-based technologies.

The Circular Texture Meter (CTM) is a laser-based device that can be used in the laboratory or in the field to measure the macro-texture of the pavement surface. According to the ASTM E2157, the CTM consists of a laser-displacement sensor that rotates over a circle with a diameter of 284.5 mm and measures the profile of pavement surface texture. The profile includes 1024 points scanned at an interval of 0.87 mm. Using the instructions provided by ASTM E 1845, the measured profile then is sectioned into eight equal parts and the mean profile depth (MPD) in each part is measured. The CTM is operator dependent. In addition, since this device can only measure the texture over a circle, it cannot collect the texture data along the wheel path. To increase the efficiency, several parts of a road section must be surveyed using the CTM to collect texture data (Pidwerbesky et al., 2006). Studies conducted by Hanson and Prowell in 2004 and 2005 showed poor repeatability and reproducibility of the CTM (Hanson and Prowell, 2004; Prowell and Hanson, 2005).

Vehicle-mounted laser devices have been developed to dynamically collect pavement macrotexture data on the go without requiring stopping. In 2012, Sengoz assessed the determination of pavement surface texture by the SPT and laser scanning. The comparison entailed using a laser scanner. The laser was mounted on a portable vehicle and connected to a personal computer. The developed prototype measured texture by means of a laser light. This study was conducted on sections exposed to the same environment but different traffic loading conditions. In this study, the standard method (ASTM E 1845), which calculates the MPD of the pavement surface texture from the surface cross-section, was applied. It was concluded that the laser scanner results are comparable with the SPT.

In 2014, Yaacob et al. conducted a study comparing the SPT results of the MTD to the sensor measured texture depth (SMTD) obtained from a vehicle-mounted multi-laser profiler. The SMTD is calculated as the standard deviation of the profile amplitudes, measured by a sensor over a 300 mm \pm 15 mm length of the road. Details of the calculation for this index are provided in the study conducted by Freitas. The researchers tested a section of about 7 km along Pagoh to Yong Peng Utara, Section 3, North-South Expressway. The SPT was performed in 64 different locations every 50 meters along the direction of traffic. In addition, laser measurements were taken in the same locations. The results showed a weak correlation between the two methods of MTD measurements.

The weakness of the correlation between the two approaches could be due to the fact that the two tests were conducted at different times, one month apart. It is likely that there was some polishing of the aggregate by vehicle tires. A study conducted by Halil et al. in 2008 contradicts the results of this study. They found a strong correlation between the sand patch and multi-laser profiler. However, the researcher covered a more extensive range of texture depths—from 0.5 mm to 2.0 mm—leading to a stronger correlation.

Currently several vehicle-mounted laser measuring devices available on the market are capable of assessing pavement texture depth. For instance, the Automatic Road Analyzer (ARAN), manufactured by Roadware of Canada, can collect the texture profile on pavement surfaces and calculate the MTD (Meegoda et al., 2002). Within the ARAN software, the MTD is estimated from a numerical integration of the area between the road profile and a horizontal line representing the highest value of that profile, as depicted in Figure 1.3(a).

In another study performed in 2015, Hao et al. used a real-time laser pavement texture meter to collect pavement surface data. The researcher developed an algorithm to calculate the MTD from the data collected along the laser line. First, as shown in Figure 1.3(b), the collected data is divided into three segments. Using the least square method, a straight line is fitted to each segment. Then, the distances between the points and the corresponding line are calculated. This process is repeated for all the scans. The MTD of the scanned pavement is equal to the average of all previously calculated distances. However, as illustrated in Figure 1.3(b), the algorithm does not remove the slope from the collected data; hence, the calculated MTD is biased.

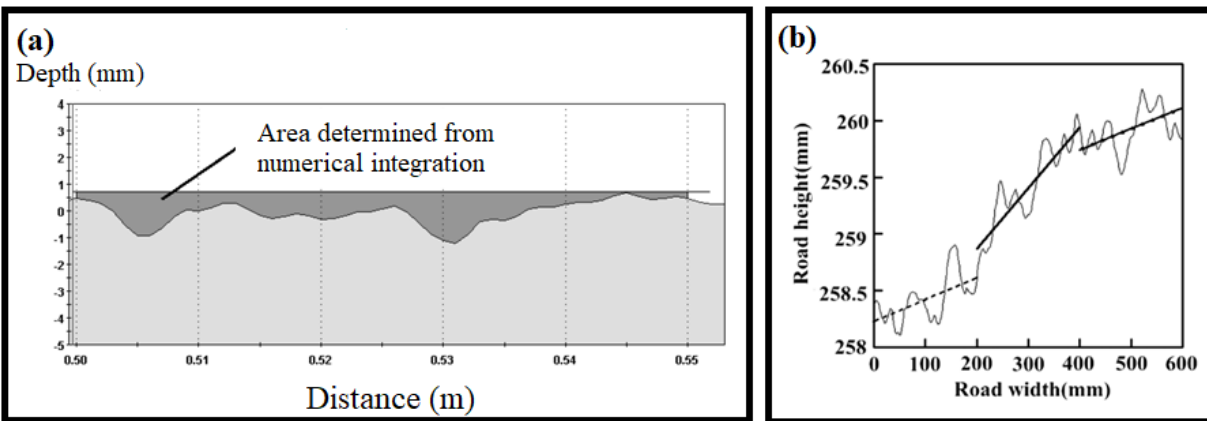


Figure 1.3 Schematic representation of the MTD calculation (a) utilized in the ARAN software, (b) developed by Hao et al., 2015

1.6. Research Goal and Objectives

Review of previous studies showed that through using imaging and sensor technologies and mathematical functions such as FT and PSD, traditional measuring methods of texture can be replaced. The study presented in this report aimed at proposing a high-resolution laser scanner prototype to measure aggregate and pavement macro- and micro-texture. This prototype system

has the advantage of capturing 3D data using an automatic, simple, and quick operation. The objectives, listed below, were considered in this research study:

1. Developing a methodology to obtain the macro- and micro-texture of aggregate particles by using the laser prototype and Fourier analysis.
2. Developing a methodology to simulate the SPT by using the laser prototype.
3. Comparing the performance of the developed laser prototype with CTM to calculate the MPD of pavements.
4. Finding the correlation between field-measured texture data obtained by the develop laser prototype and friction.

1.7. Report Organization

This report presents a complete description of the objectives, research performed, methodologies used, and the results achieved during this project. Chapter 1 provided the information on pavement skid resistance and its connection to pavement texture, problems with the current pavement texture measurement techniques, and the research goal and objectives. Chapter 2 documents the development process of a 3D non-contact laser scanner prototype at the University of Texas at Austin. This chapter presents a description of the main components of the laser system. Afterwards, the experimental setup and the laser configurations used in this research are explained. Chapter 3 describes the methodology used to measure the surface texture of aggregate particles by using the developed laser scanner prototype in order to differentiate them. The main purpose of this chapter is to determine the dominant wavelengths in the micro-texture of aggregates that significantly contribute to the pavement surface friction. Chapter 4 provides the development of an algorithm to simulate the SPT and MTD measuring process by using the developed laser prototype. Chapter 5 is dedicated to study the relationship between field-measured texture data and friction. Finally, Chapter 6 provides a summary of findings, conclusions, and recommendations. This research study also assessed the application of the developed prototype to improve chip seal design methods; those results are provided in Appendix A.

Chapter 2. Development of the Scanner Prototype

2.1. Introduction

Developments in profiling technologies have facilitated the measurement of surface texture. Nowadays, a handful contact and non-contact types of profiling techniques are available (Poon and Bhushan, 1995; Vorburger and Raja, 1990). The superiority of non-contact type profilers is that no surface scratch is caused by the device during profiling (Sherrington and Smith, 1988). This chapter documents the development process of a 3D non-contact profiler, which can be used to measure both micro- and macro-texture.

2.2. Line Laser Scanner Prototype

A line laser scanner (LLS) was utilized in this research study. This device is a two-dimensional (2D) non-contact laser sensor that projects blue light with a wavelength of 405 nm in a horizontal line. Generally, the line laser scanners available in the market work based on two different light colors: blue and red. The superiority of blue light over red light is its smaller wavelength, which results in less error and higher precision. The violet light is emitted from a source in the LLS and the reflection of the light from a given surface is then captured by a detector. If the angles between the projected light and the reflection are known then, by using triangulation, the height profile of the surface relative to the system's reference line can be calculated. Small changes in height due to the texture irregularities can also be captured using this scanner system. Figure 2.1(a) illustrates this triangulation system.

In this research study, a prototype (Figure 2.1(b)) was developed to enable the LLS to capture three-dimensional data. For this purpose, the LLS was mounted on a linear translation stage to travel over the surface and scan it. The developed LLS prototype is capable of collecting a maximum of 800 points in the transverse direction (X-direction) and a maximum of 15,000 points in the longitudinal direction (Y-direction). At each point, the LLS captures the relative height of that point, in millimeters (Z-direction). Combining the discrete height values captured in Y or X-direction provides height profiles. Therefore, the LLS is able to capture maximum 800 or 15000 parallel height profiles in Y or X-direction, respectively. While 800 points along the X-direction are captured at once and independent of time, the measurement along Y-direction depends on the speed of the scan and the frequency of the measurements. Both the linear translation stage and the laser are connected to a computer, and the scanned data are collected there in an Excel file. Each row of the Excel file contains the scanned data in X-direction and each column contains the scanned data in Y-direction.

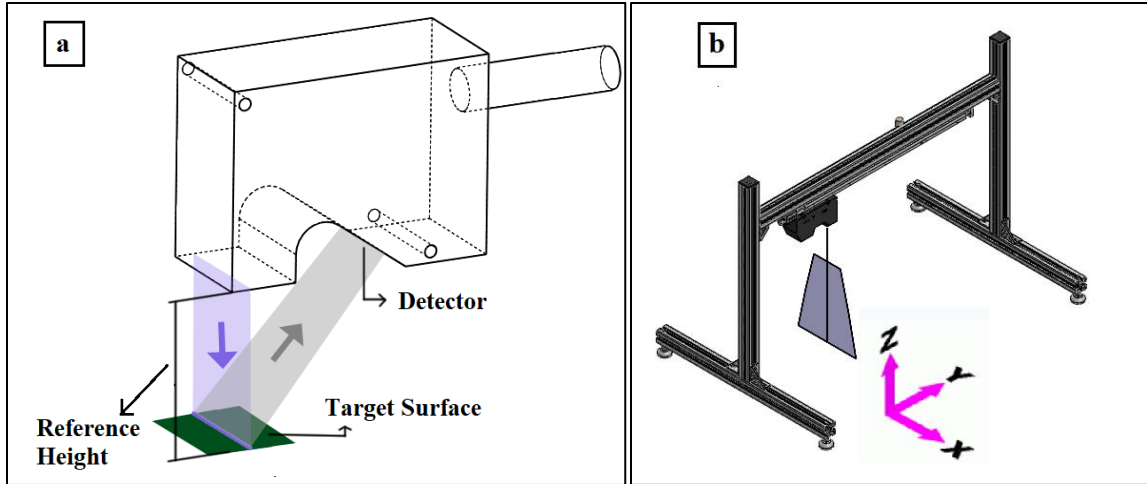


Figure 2.1 a) The triangulation system of a laser, and b) the prototype including the frame and mounted laser

During the use of the developed LLS prototype, researchers were faced with many issues regarding the measurement taking. The following explain the approaches employed to overcome those issues.

2.3. The LLS Range of Measurement

According to the laser specifications and manufacturer's instruction, the reference distance in Z-direction, which is the vertical distance between the laser and the object (Figure 2.2), is 80 mm. To achieve an acceptable measurement, the target should be close to the reference distance and within the measurement range of ± 23 mm in Z-direction. On the other hand, the measurement range in X-direction depends on the vertical distance of the target from the laser so that the closer distance to the laser, the narrower the measurement range in X-direction, as depicted in Figure 2.2. The measurement range in X-direction is 25 mm at near side, 32 mm at reference distance, and 39 mm at far side.

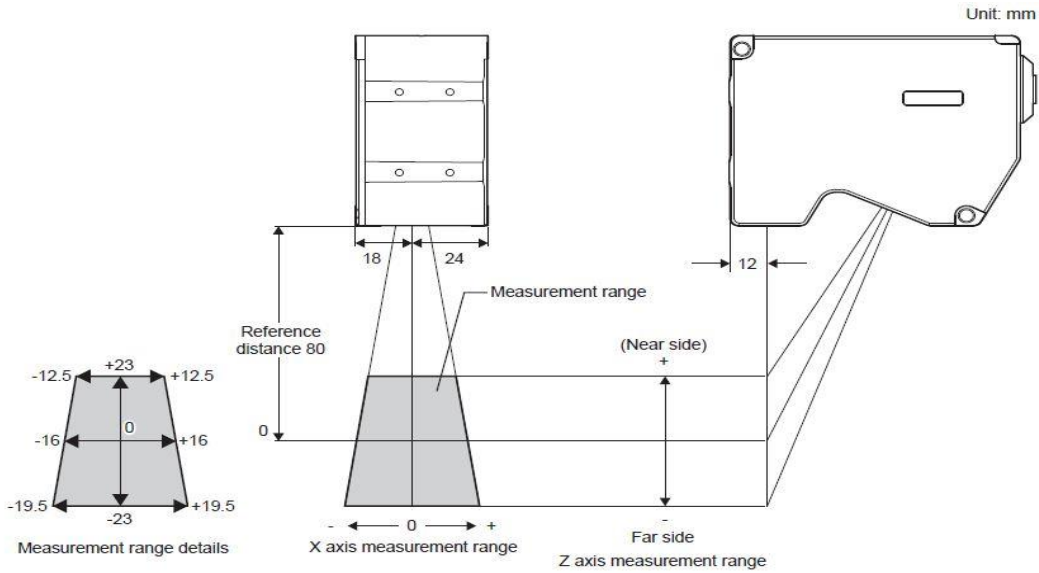


Figure 2.2 The LLS Measurement Range in X and Z-direction

After scanning, the points with extremely low values of -99.9999 mm, called *negative dropouts*, were recognized at the two sides of the laser line along with X-direction. Experiments to understand the negative dropouts at the edges of a profile were performed and it was found that the number of dropouts of the laser changed with height (Z-direction). The experiment led to the understanding of the quantity of dropouts observed as a result of different heights. As indicated in Figure 2.3, when the laser head was fixed at a height of 60 mm from the surface being measured, the number of dropouts increases. Therefore, the X-direction had approximately 220 negative dropouts. When the laser head was fixed at its reference height of 80 mm, the number of dropouts were at approximately 95–100 points. Lastly, the laser head was fixed at 100 mm and it was found that there were no dropouts and the scan line was at its full 800 points in the X-direction.

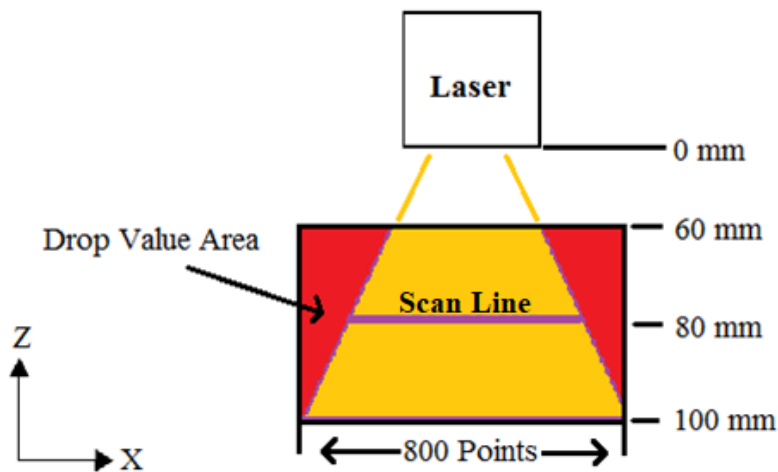


Figure 2.3 Schematic of laser's scan area

The results showed that an algorithm within the laser controller adds dropouts to the profiles based on the height. The closer the laser head is to the surface, the more dropouts appear and the scan line decreases. The opposite is true for when the laser is at approximately 100 mm: it has no dropouts and the full scan area can be used. This is done to keep the distance between two consecutive pints in the X-direction constant, i.e., 50 microns.

2.4. Block Measurement

As a result of the internal data processing done within the controller unit described above, the scanning interval in X-direction (ΔX) is fixed and equal to 50 microns. This following experiment was performed to understand how the differences in the height of the laser, the location of the object, and the object's width affected the profile data interval. Gage blocks with precisely manufactured dimensions were used as an object for this experiment. The gage blocks are certified by Fowler specifications with calibration traceable to the National Institute of Standards and Technology (NIST). Different sizes of gage blocks were used to understand how the object's width played a role in the measurement. The frame of the prototype is composed of two vertical supports that allow for the height of the laser to be adjusted. The variables in this experiment are as follows:

- Gage blocks width (mm): 5, 7.5, 10
- Height of the LLS (mm): 110, 100, 94, 80, 75, 70, 60

This experiment was performed in two parts. In the first, the focus was to see how the ΔX changed with varying gage block width. The placement of the gage blocks was in the middle of the laser's scanning line. Table 2.1 contains the ΔX for the respective gage block (5.0, 7.5 and 10.0 mm) and the reference height of the laser from the laser to the surface of the table. A single reading was taken for each experiment. To calculate the profile data interval in Excel, the following equation was used:

$$\Delta X = \frac{\text{Size of gage block (mm)}}{\text{Number of points in the measurement that make up the gage block}} \quad \text{Equation 2.1}$$

Table 2. 1 Scanning Interval for Varying Gage Blocks

Height	ΔX for 10mm	ΔX for 7.5mm	ΔX for 5mm
110 mm	0.0513	0.0500	0.0510
100 mm	0.0508	0.0500	0.0500
94 mm	0.0505	0.0497	0.0495
80 mm	0.0526	0.0503	0.0500
75 mm	0.0515	0.0500	0.0500
70 mm	0.0518	0.0500	0.0510
60 mm	0.0503		

For the second part, the focus was to see how placing an object in different parts of the laser's scanning line would affect the profile data interval. Furthermore, the height of the laser and the surface were also investigated. A single gage block with the width of 5.0 mm was used throughout this experiment. The measurements consisted of three locations of the gage block for each height: right, center, and left of the laser line. Figure 2.4 shows the placement of the 5-mm block at the center and the left of the laser line. The center location was measured with a ruler by taking the length of the scanning line and measuring the middle. The left and right locations depended on the height of the laser.

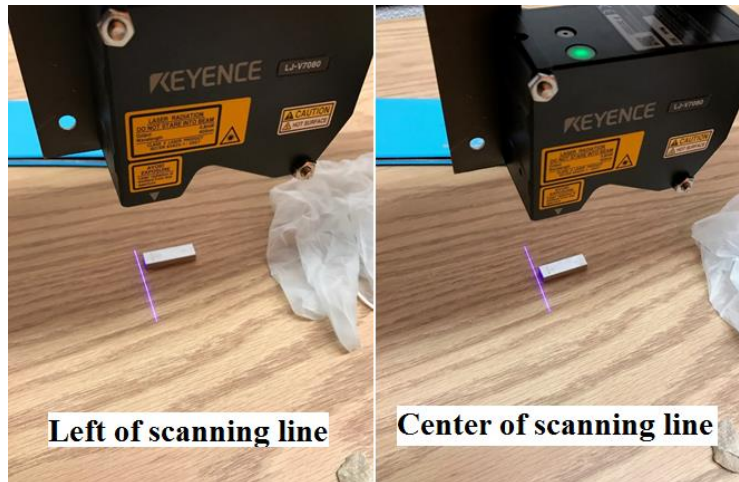


Figure 2.4 Gage block placement in laser's scanning line

Three different heights were tested: 100, 80, and 60 mm from the laser to the surface of the table, with three different scans per each location representing the left, center, and right. As seen in Table 2.2, a negative offset represents the right side and a positive offset represents the left side. Each location was scanned once.

Table 2.2 Scanning Interval for a 5.0 mm Gage Block at Varying Locations

Height (mm)	Offset from center (mm)	ΔX Right	ΔX Center	ΔX Left
100	-10	0.0515		
100	0		0.0506	
100	10			0.0512
80	-8	0.0521		
80	0		0.0503	
80	8			0.0515
60	-5	0.0518		
60	0		0.0500	
60	5			0.0506

As a result of this experiment, it was found that when the object is placed in the middle of the scanning line and the object is thin enough for the scanning line to reflect from the edges of the object, the readings are found to be close to the profile data interval of 50 μm mentioned in the laser specification. The profile data interval then varies as the object gets further away from the center of the scanning line. This is mainly due to the edge furthest away from the center not being able to reflect back to the laser, hence increasing the uncertainty and reducing the accuracy. Accordingly, the reference distance of the laser from the background was kept at 80 mm and the objects were placed in the center of the laser line during the scans.

2.5. Scanning Interval

Micro-texture refers to the surface features with wavelength less than 0.5 mm and macro-texture refers to the features with wavelength between 0.5 and 50 mm. The focus of this study was on three ranges of wavelength, including 1) the second decade of micro ($0.005 \text{ mm} < \lambda < 0.05 \text{ mm}$), 2) the first decade of micro ($0.05 \text{ mm} < \lambda < 0.5 \text{ mm}$), and 3) the first decade of macro ($0.5 \text{ mm} < \lambda < 5 \text{ mm}$). In order to capture the data in the second decade of micro-texture, based on the Shannon theorem (Nyquist theorem), the interval between scanning points must be equal to half of the smallest wavelength of interest. Hence, in this case, the scanning interval is equal to 2.5 microns. Since the scanning interval in X-direction (ΔX) is 50 microns, scanning in X-direction cannot capture the second decade of micro-texture. To study the second decade of micro texture, the researchers used the scanning data in Y-direction. According to the Equation 2.2, the scanning interval is related to both speed and the frequency of scanning so that different scanning intervals can be obtained by adjusting these two parameters in the LLS. For instance, by setting the frequency at 1 kHz and the moving speed at 2.5 mm/s, the scanning interval would be 2.5 microns.

$$\Delta y = v * \frac{1}{f}$$

Equation 2.2

where

Δy : scanning interval in Y direction

v : moving speed, mm/s

f : scanning frequency, Hz

2.6. LabVIEW Program

To operate the LLS and the linear translation stage, two corresponding computer codes were used simultaneously: LJ-Navigator 2 and Thorlabs APT User Interface, respectively. When performing a scan, the two computer codes worked independently of one another. Therefore, the APT User Interface had to start moving the LLS and then the operator had to switch quickly to the LJ-Navigator 2 to start collecting measurements from the LLS. This resulted in missing some data at the beginning of the scan and facing different start- and end-scan locations at different measurement runs.

In order to have reliable measurements, the two codes had to be merged into a single program that could start moving the laser while simultaneously collecting measurements with the LLS. This allowed the scans to be repeatable with the same start points, fixing the problems generated by having to use two independent pieces of software.

With the use of LabVIEW and instrument drivers, a program was developed. The development led to a program that operates a single laser head while also moving the translation stage. The program gives the user full control of the translation stage, similarly to the APT User Interface, allowing for conditions to be set, such as: starting position, speed, acceleration, and end position. The discussion of each separate component of the program is explained in the next paragraphs.

2.6.1. Linear Laser Scanner (LLS)

The laser program is the main focus of the code. The logic of it is composed of the following seven components listed below and can be visualized in the flowchart in Figure 2.5.

1. Communication Interface: Before running the program, the communication needs to be configured. A USB cable is used to transfer data from the laser's controller to the PC, and an Ethernet cable with sampling at rates faster than 2.0 kHz is highly recommended. The type of connection is selected in this step.
2. Start VI (Virtual Instruments): after configuring the communication with the laser, the LabVIEW VI program can be started at this time.
3. Idle: The VI runs and awaits the communication between the computer and the laser's controller. At this step, the translation stage can be configured to operate with user defined conditions. Such conditions include: speed, acceleration, start position, and end position.

4. Data Communication: A Start/Stop button was programmed to initiate and terminate the communication between the computer and the controller. Data are not stored at this point.
5. Start Monitoring: A Start/Stop button was programmed to initiate and terminate the reading and storing of the profiles by the lasers. Note: The Start/Stop button operates the motion of the translation stage as well.
6. Read Profiles: Profiles are read and saved to the computer, a height graph starts displaying batches of profiles. Indicator boxes display the profiles read and the buffer usage. The buffer usage is a percentage, which represents the temporary storage of the profiles. Warning: if the buffer usage reaches 100, the storage is saturated with profiles and data are lost.
7. Stop Reading Profiles: A Start/Stop button can be used to commence or end the profile readings. The number of readings is only restricted by the amount of capacity in the data storage and by the length of the translation stage, which is 150 mm.

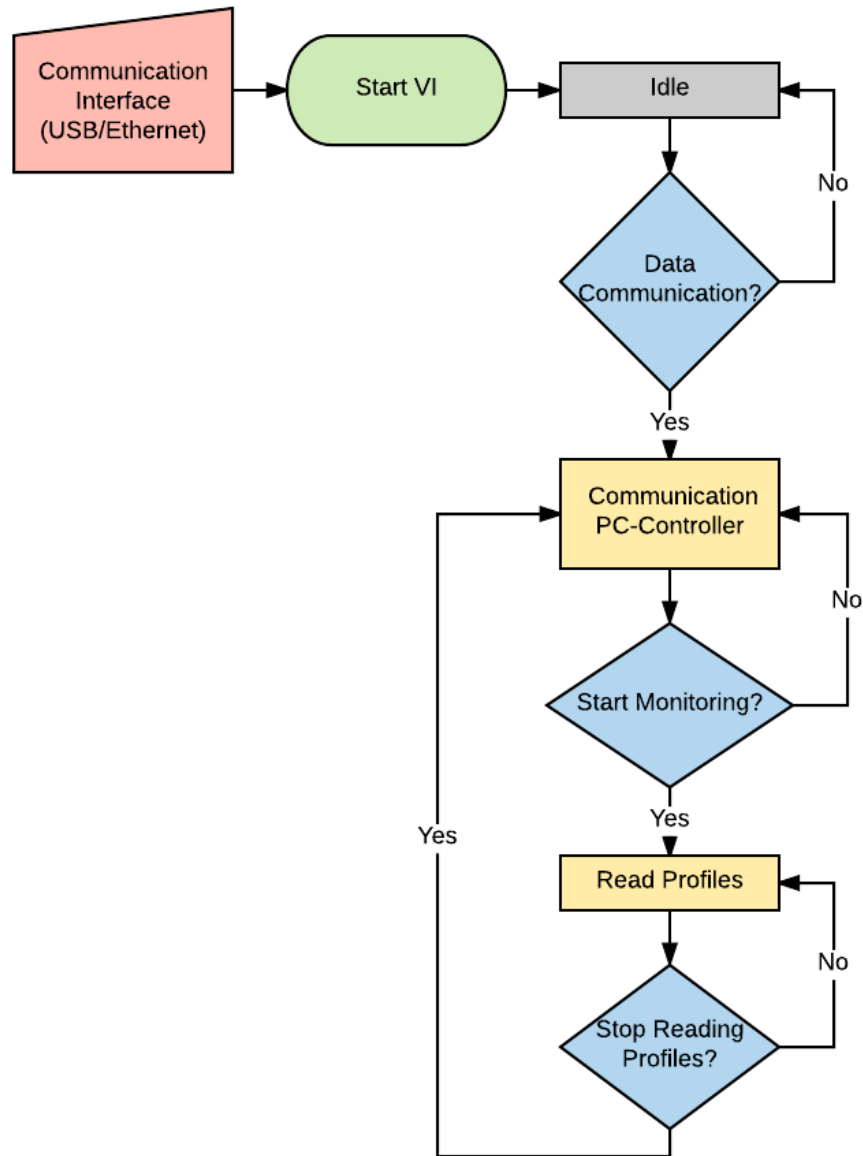


Figure 2.5 Laser’s LabVIEW process flowchart

2.6.2. Translation Stage

As mentioned, the LLS is the main focus of the program, while the translation stage is embedded within the main program and operates as a SubVI. This means that the translation stage can be operated independently of the LLS but is connected to the main program and signaled to move by step 5, as mentioned above. The configuration screen allows the user to set conditions before the program starts running. This can be defined in step 3, before the LLS starts communicating with the controller. Furthermore, after the configuration of settings, the user clicks on the “Read Profiles Start/Stop” and the translation stage SubVI receives the signal to start operating if it was given a set position to move.

2.6.3. User Interface

Figure 2.6 shows the user interface that contains seven components including the graph of the real-time grayscale image and an easy-to-use control for the translation stage. When ready to use the program, the user follows the list above to start acquiring data from the LLS. When the program starts, the graphs labeled “Height Image” displays a corresponding height image in a grayscale. While the LLS is in motion and scanning, the graph provides the user an acknowledgment that the program is running. If aggregates are scanned, a real-time image of the aggregates can be seen.

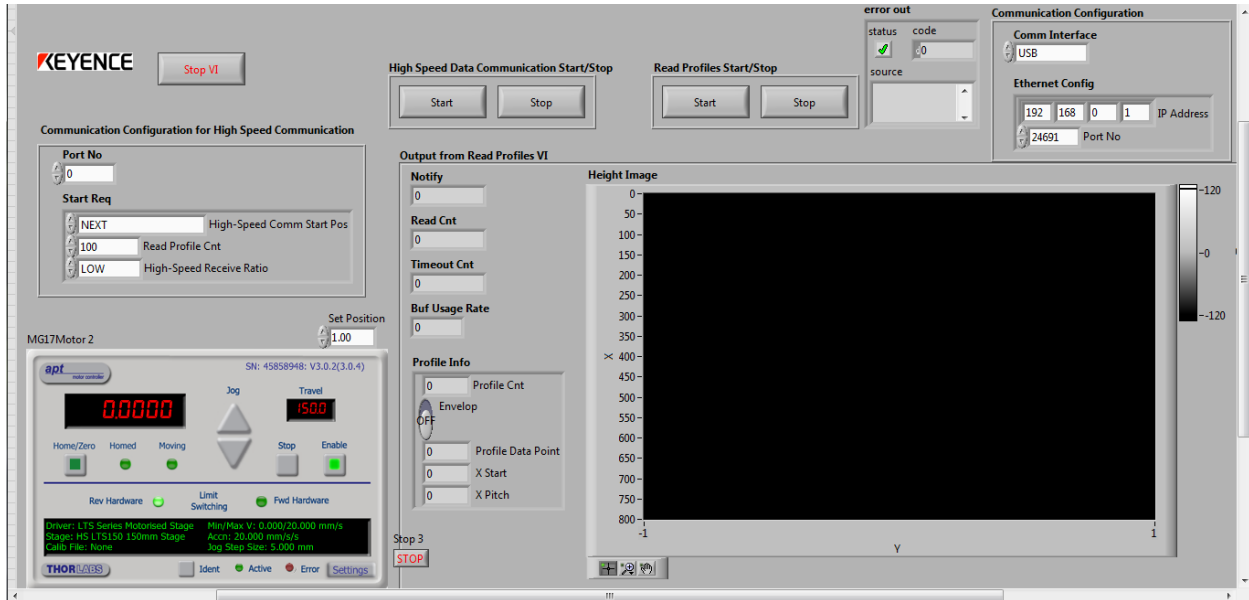


Figure 2.6 User interface of LLS program

2.7. Repeatability of the LLS

The LLS specification provides the repeatability in X and Z-direction of 10 and 0.5 microns, respectively. The repeatability of the developed prototype in Y-direction is required to ensure the accuracy of the measurements. The surface of an aggregate particle was scanned five times in Y-direction to check the repeatability of the LLS and the reliability of captured data. The repetitive scanning was performed under the same conditions without moving the developed LLS prototype or the aggregate. The height profiles located in the middle of the scanned data was selected from the five scans. As an example, a profile captured from the particle surface in Y-direction is depicted in Figure 2.7. The horizontal axis in these figures represents the number of points that were scanned in Y-direction with scanning interval of 2.5 microns and the vertical axis shows the height values. To study the repeatability, the standard deviation of five profiles was calculated and plotted along Y-direction below the height profile in Figure 2.7. According to this figure, at all scanned points the standard deviation of five height values was greater than 5 microns. In addition, higher standard deviations were observed within the areas in which the longitudinal profile was steep. Therefore, it can be concluded that the laser measurement was not reliable in the second decade of the microtexture. Hence, the research team decided to study the data within the range of the first decade of

micro- and macro-texture, which is above 50 microns. Accordingly, the scan speed and frequency were adjusted to obtain the scanning interval of 25 microns.

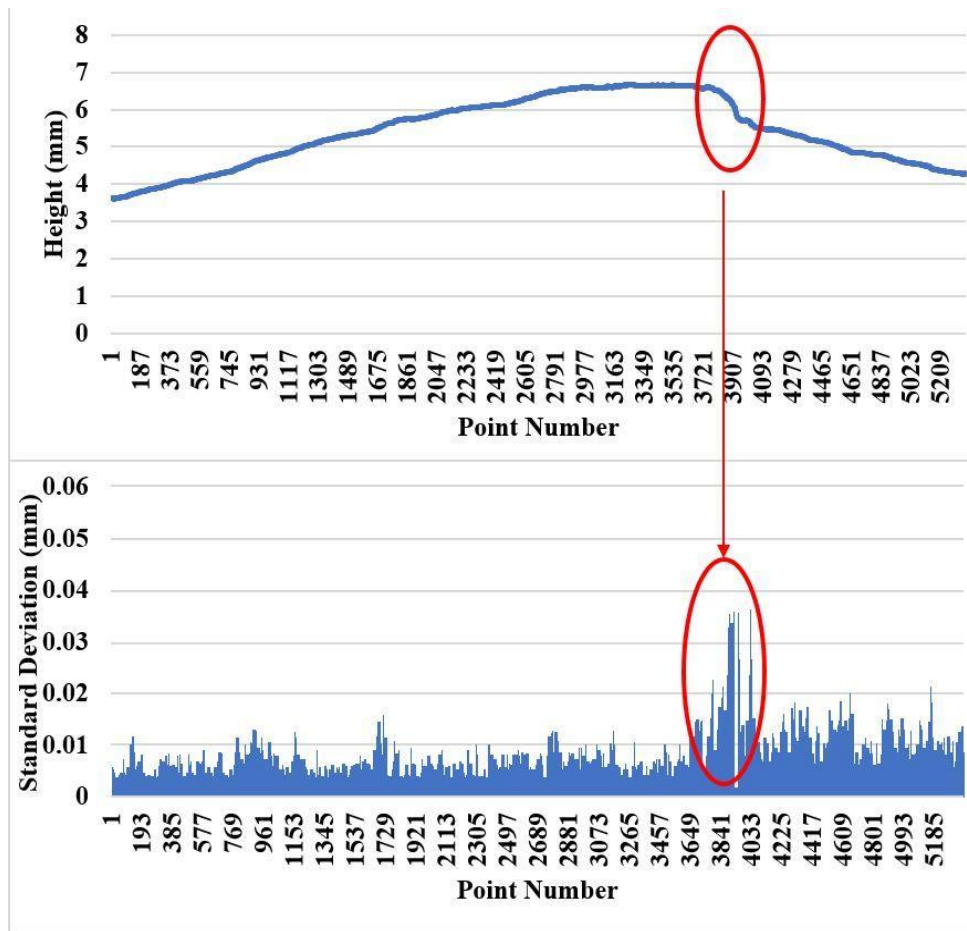


Figure 2.7 Height profile of aggregate along y-direction (top), and corresponding standard deviation (bottom)

2.8. Tilt and Error Issues

It is ideal to have a leveled surface for the measurement in order to minimize measurement errors. However, in some cases, the presence of laser line tilt in X-direction is inevitable due to the slope in the existing surface or the laser head, hence, tilt correction is required. This correction can be done automatically through the LJ-Navigator 2. In addition, before the data processing, the slope line of the scanned surface in Y-direction must be leveled to diminish the errors in the future calculations.

Dropouts, which are the points with either very high or low depth value, are recognized as errors. These errors are caused when the laser is not able to detect the light reflection. These errors are usually located at the edges of an object or at the holes. Figures 2.8(a) and 2.8(c) provide scans of an aggregate and a pavement surface, respectively. As shown in Figures 2.8(a) and 2.8(c), the

negative dropouts can be found at the two sides of the laser line along with X-direction. To remove these errors from analysis, fifty columns in each edge were trimmed out from the stored data. Thus, the final Excel data (as shown in Figure 2.8(b) and 2.8(d)) consisted of 700 points in each row. Points with high depth values mainly occurred during the scan of pavement surfaces. Using linear interpolation, those spikes were smoothed. As shown in Figure 2.8(b), dropouts exist around the aggregate edges. According to the ASTM E 1845, the number of dropouts of a profile should not exceed 10 percent of that profile (ASTM E 1845, 2009). Several factors such as background color, glossiness, ambient light, scanner settings, etc., might affect the quality of scanned data. Accordingly, researchers have studied the influence of these factors on the scanned data.

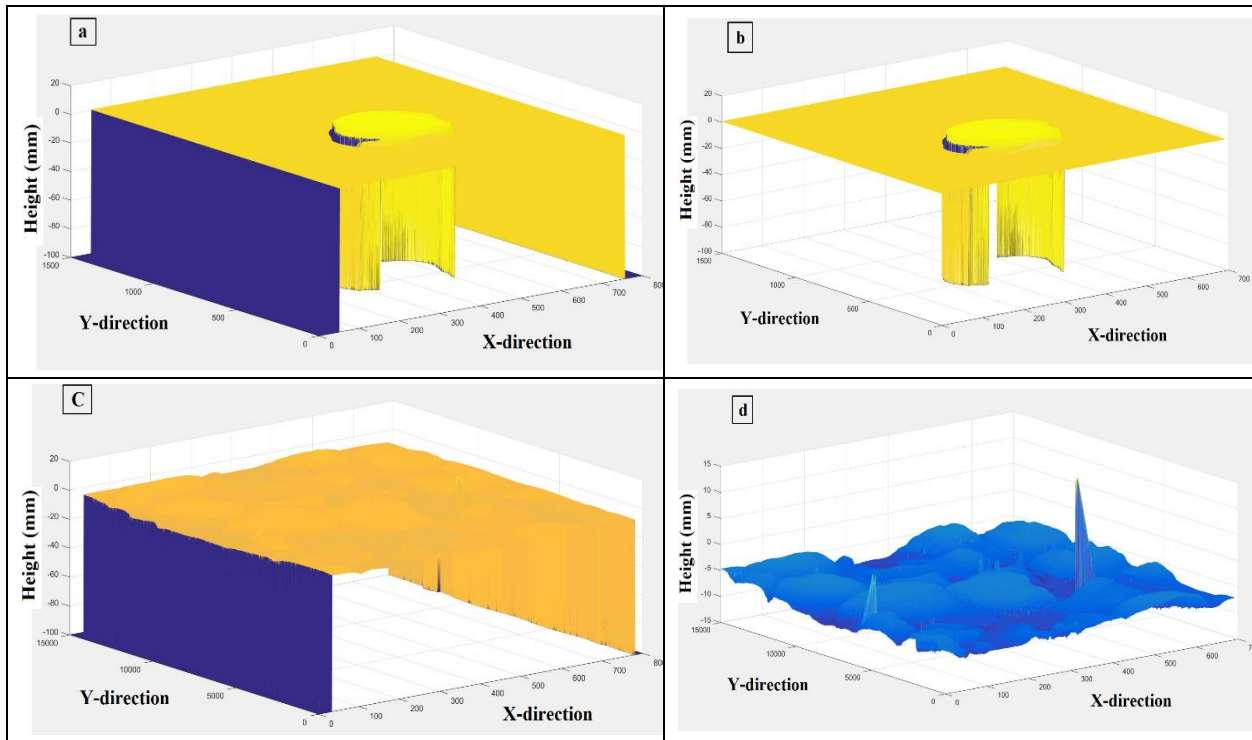


Figure 2.8 a) Unfiltered 3D scan of an aggregate, b) 3D scan of an aggregate after removing the errors at the edges, c) unfiltered 3D scan of a pavement surface, and d) 3D scan of a pavement surface after removing the errors at the edges

2.8.1. Background Color and Ambient Light

To understand how the LLS works, a basic explanation is given here as to how semiconductor lasers emit light. To start, a diode consists of two semiconductors that are either n-type or p-type. The semiconductor is doped with atoms that have different electron configuration. For an n-type, the atoms are doped with allowance for extra electrons to flow freely, as there is one extra electron in the outermost energy level. The p-type is doped with an element that has a ‘hole,’ lacking an electron in the outermost energy level. When the two materials, or semiconductors, are combined into a diode, electrons flow to the holes and vice versa. An electrical power source is used to continue this interchange of holes and electrons with the use of current. At the junction of the

semiconductors, photons are released as the electrons combine with the hole. The wavelength is dependent on the semiconductor material; the different materials can have different energies from the electron-hole interaction and the photon energy is inversely proportional to wavelength. Spectral range of light is presented in Figure 2.9. For the case of the LLS, the photon has a 405-nm wavelength, which is in the visible spectrum of light and seen as the color violet/blue to the human eye. The violet light is emitted from the LLS and then the reflection of the light from a given surface is captured by a detector. In order to evaluate the effect of background color on the accuracy of laser measurement, different color papers were placed beneath an aggregate particle (as can be seen in Figure 2.10) and tests were performed.

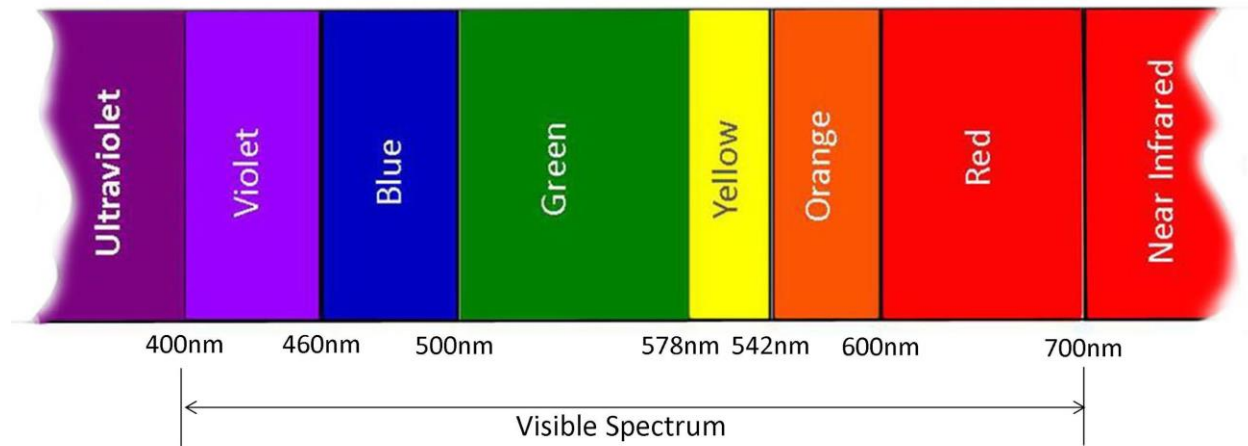


Figure 2.9 Spectral range of light (<http://karnikakapoor.blogspot.com/2016/04/weirdness-colour-spectrum.html>)



Figure 2.10 Using different background colors in measurement

The measurements were compared to each other with respect to the number of dropouts that occurred for each color paper used in the test. The results showed that the effect of background color is negligible on the data measured by the laser. This might be due to the short wavelength of the LLS photon, which is violet, compared to the other colors.

In addition, in order to detect how the scanning results differ by changing the intensity of external lights, an aggregate particle was placed on a selected background and scanned twice: in a bright room and in a dark room with a covering box on the laser. The test was performed by comparing

the number of dropouts. Note that the other conditions were kept the same for both tests. It was found that in the laboratory, the laser can be operated in the room light. However, in the field, the laser must be covered by a box to avoid the direct sunlight. As provided in the LLS manual, the maximum illuminance resistance is 10,000 lux. The illuminance is used as the intensity of light that hit a surface. An illuminance of 10,000 lux corresponds to a full daylight with a non-direct sun which means that the laser should not be exposed to a direct sun. Accordingly, during the field measurement, direct sunlight could affect the measurement of the laser, since the illuminance can exceed the maximum resistance. Therefore, for all the measurements taken in the field, a covering box was used.

2.8.2. Adjusting the Settings of LJ-Navigator 2

The LJ-Navigator 2 offers several features to deal with the negative dropouts during the scanning. Several tests were performed to get a better understanding of the effect of these features on the measurement.

2.8.3. Test #1

As shown in Figures 2.11(a) and 2.11(c), an aggregate particle was placed in the scanning area of the laser and scanned in two different directions, from left to right and then from right to left, to see whether the direction of scanning affects the negative dropouts at the edges of aggregate. Figures 2.11(b) and 2.11(d) illustrates the X-Y view of the scanned aggregate. The result obtained from these two tests is that the black area (undetectable parts by the laser) occurred at the same location in two scans. Therefore, the performance of the laser is similar in both directions.

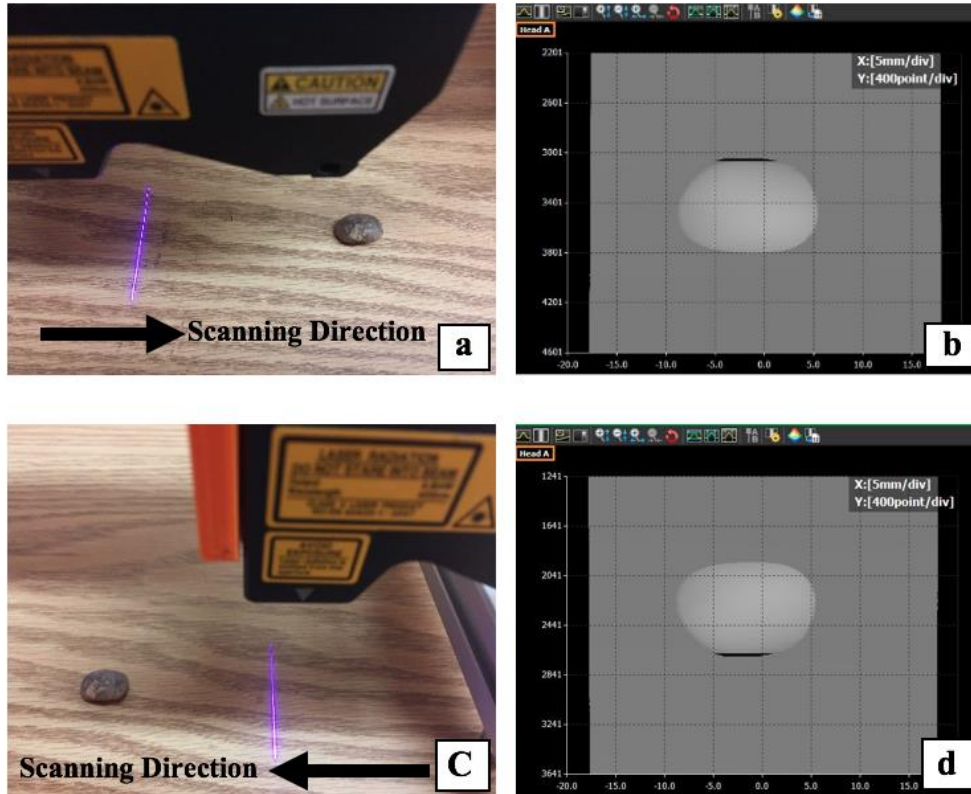


Figure 2.11a) Scanning an aggregate from left to right, b) X-Y view of the scanned aggregate, c) Scanning an aggregate from right to left, d) X-Y view of the scanned aggregate

2.8.4. Test #2

According to the LLS manual, the negative dropouts can be considered as either dead zones or invalid data. In this test, negative dropouts were considered as dead zones. An aggregate particle was scanned three times. The variable in these three scans was the interpolation mode shown in Figure 2.12. Three interpolation modes including no interpolation, linear interpolation, vertical interpolation are offered by the LJ-Navigator 2. Figure 2.12 depicts how a profile changes by choosing the different interpolation modes. In each scan, one of these modes was selected to find how the interpolation feature influences the measurement.

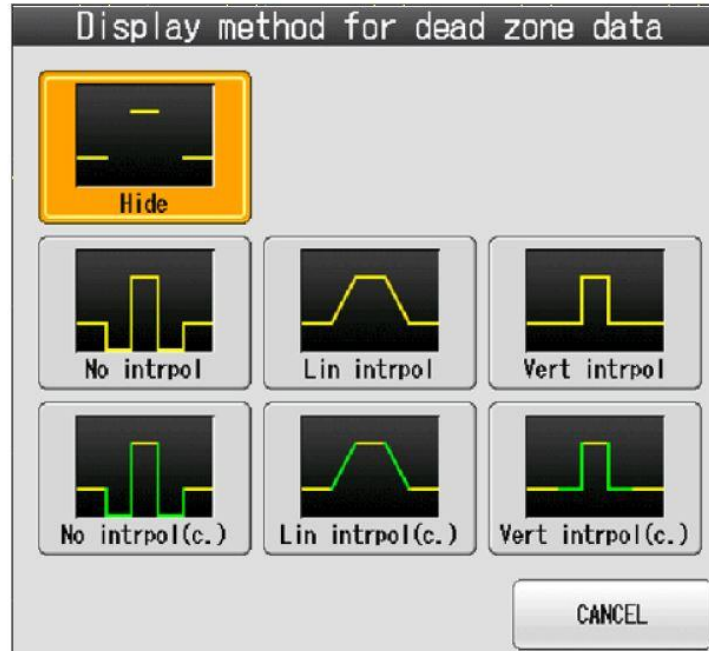
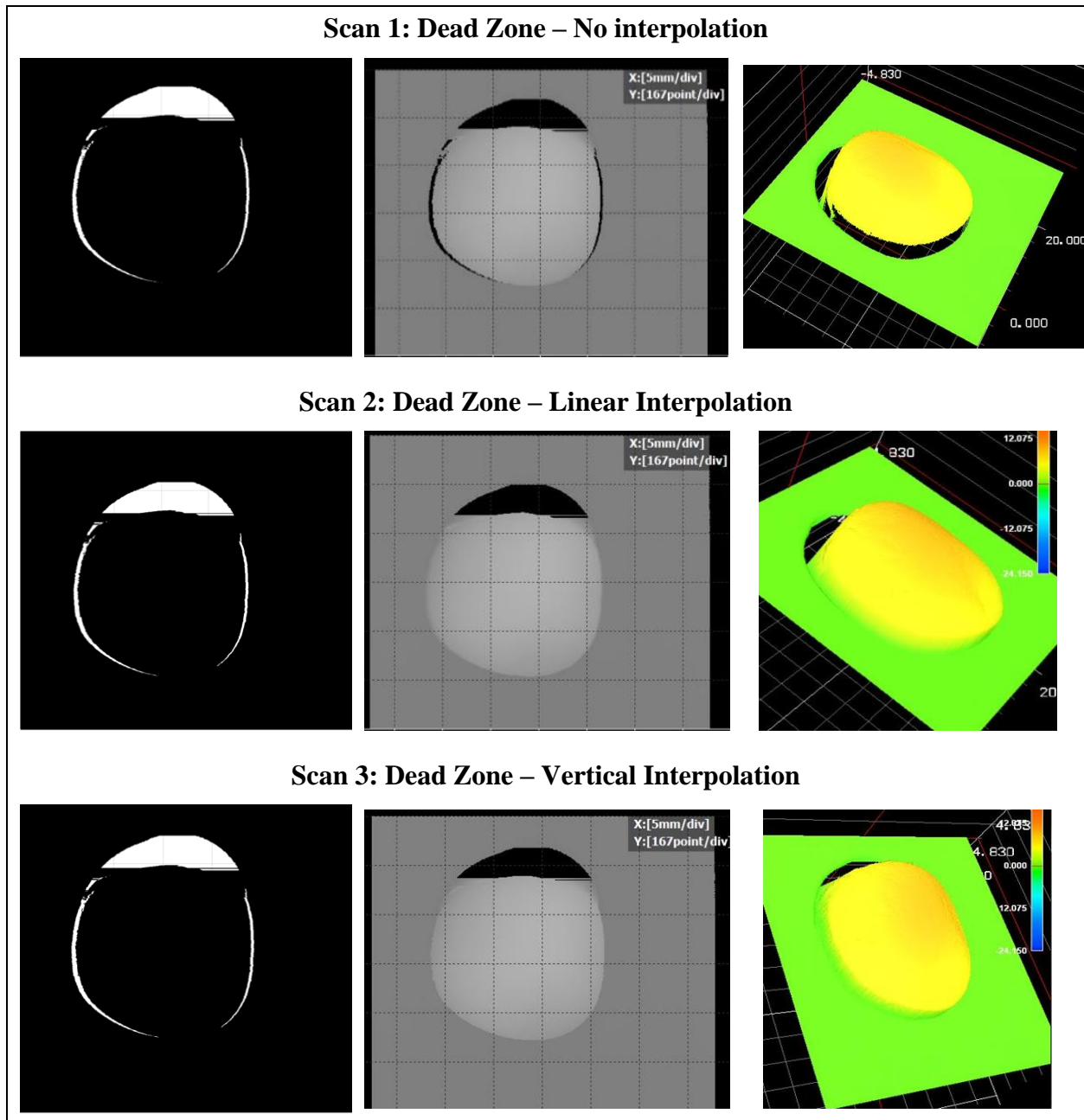


Figure 2.12 Three interpolation modes in the LJ-Navigator 2

The results of the scans are provided in Table 2.3. Each row consists of three figures corresponding to each scan. The first figure from the left show the X-Y view of the outputs in the Excel file in which the white area illustrates the dead zone. The second and the third figures in each row present the X-Y view and 3D view provided in the LJ-Navigator 2. It was found that once the negative dropouts are considered as dead zones, the interpolation modes only affect the display of the data in the LJ-Navigator 2 and no change is made on the stored data in the Excel file. The number of the negative dropouts was also counted in each scan and compared to each other. These results also indicated that the interpolation features do not impact the errors in the stored data.

Table 2. 3 Results of Test #2, Dead Zone and Interpolation Modes



2.8.5. Test #3

In this test, negative dropouts were considered as invalid data rather than dead zones. Linear interpolation mode was also selected. Figure 2.13 shows the difference between one profile in X-direction in dead zone selection versus invalid data selection. As apparent in this figure, for invalid data, the linear interpolation feature affects the negative dropouts at the edges of the aggregate and linearly interpolates them.

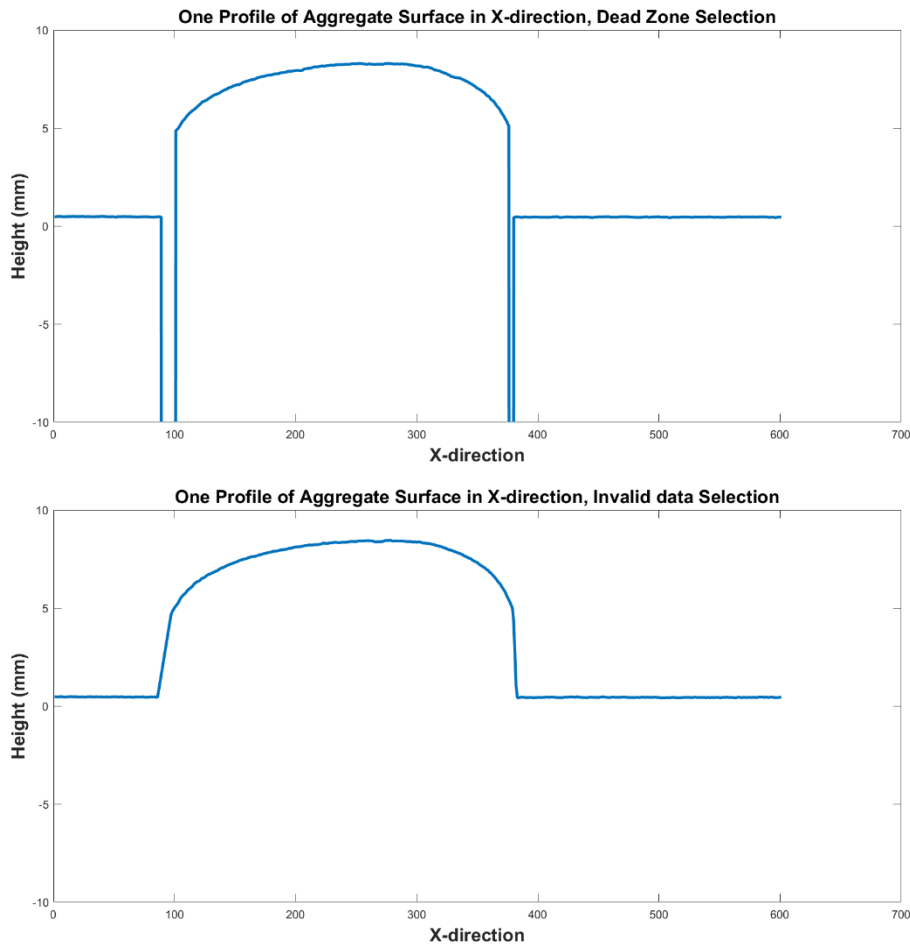


Figure 2.13 Comparing one X-direction profile of aggregate surface in dead zone and invalid modes

2.8.6. Test #4

The LJ-Navigator 2 also provides the invalid data processing feature in Y-direction. In order to apply this feature, processing time, which indicates the number of consecutive invalid data, must be selected appropriately. In this test, three numbers—10, 20, and 60—were selected. As shown in three plots of Figure 2.14, while the values 10 and 20 were less than the number of negative dropouts, 60 was an appropriate number for processing time. However, as illustrated in the last plot of Figure 2.14, the disadvantage of invalid data processing feature is that in Y-direction the negative dropouts observed in the early parts of the aggregate (black area) are completely replaced by the valid data captured from the background. However, it is not known that the black area is related to the background or the aggregate. Therefore, this feature did not help to restore the missing parts.

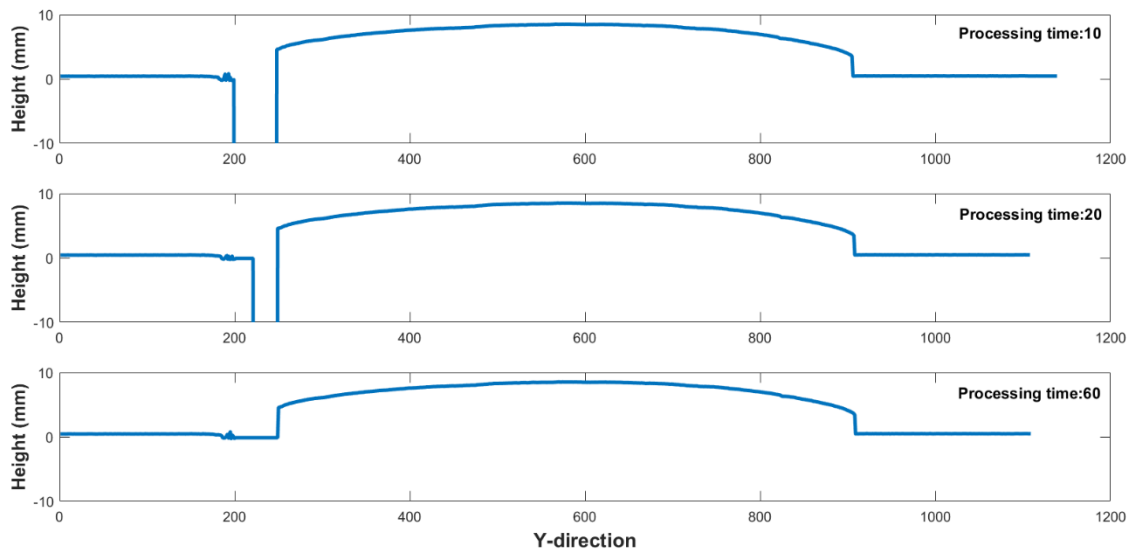


Figure 2.14 Comparing one Y-direction profile of aggregate surface in different processing time

2.9. Combining Two Scan Datasets

To overcome the negative dropouts resulted from the triangulation system used by the LLS, the research team decided to perform two scans on the object so that the object is rotated 180° in each scan. Then the scanned data were merged using a code developed in MATLAB. For this purpose, a metal plate was built, as shown in Figure 2.15, and the aggregate was glued to the plate. After the first scan, the plate was rotated 180° and scanned from the other direction. It should be noted that after rotation, the plate was kept in the same location to reduce additional noise in the measurements. In order to merge the two datasets, the data of the second scan was rotated 180° . Then using the cross-correlation command in MATLAB, the similar parts were determined and then the two datasets were overlaid. Figure 2.16 illustrates the two datasets brought on top of each other. The white area represents the data points which are common in both datasets. The green and pink areas are related to the first and second datasets, respectively. As can be seen in this figure, there are still some black areas and it is unknown whether they are part of the aggregate or the background. Currently, the research team is obtaining new laser heads that will allow them to acquire the data without any processing and, therefore, the unknowns related to the black areas will be avoided.

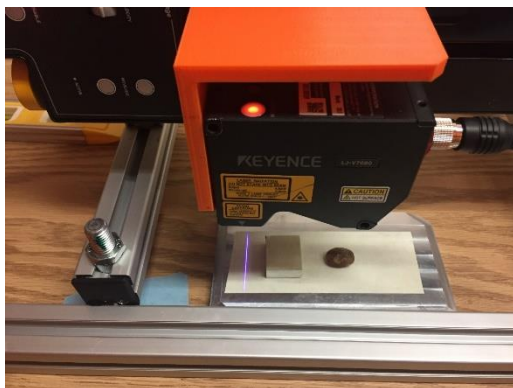


Figure 2.15 Metal plate

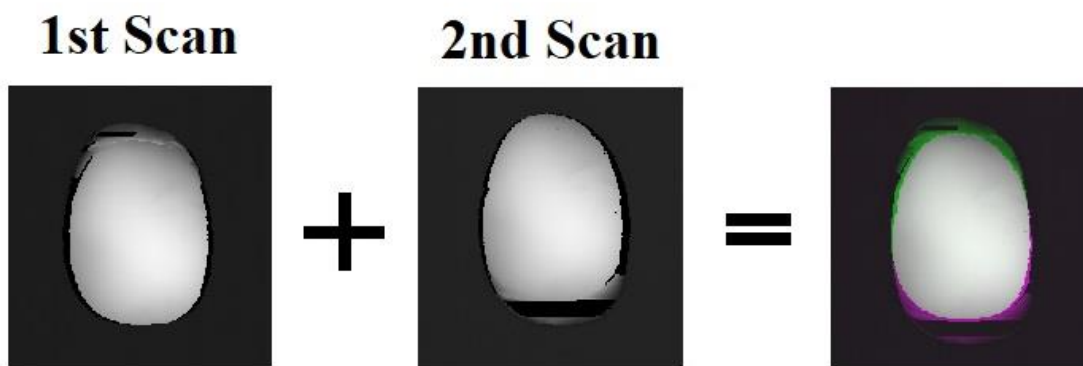


Figure 2.16 Black and white view of the first scan, second scan, and the two datasets on top of each other

Chapter 3. Investigating the Aggregate Texture

3.1. Introduction

Macro- and micro-texture of the pavement surface vary widely with the type and source of the aggregates (Ahammed and Tighe, 2008). Aggregates from various sources have different textures. Micro-texture of aggregates is a critical component of pavement texture as well as a major contributing factor in roadway safety, especially in low speed conditions. Comprehending the effects of specific wavelengths in micro-texture is essential in the design of pavements to achieve adequate skid resistance. This chapter describes the texture measurement of two different aggregate types using the developed LLS prototype. PSD analysis with two friction parameters, root mean square roughness and depth of surface roughness, were utilized to characterize the range of wavelengths that significantly contribute to the friction properties of the aggregates.

3.2. Material Preparation and Data Collection

In this study, two different types of aggregate commonly used for asphalt mixtures in Texas were obtained from two different quarries. Three particles were selected from each type of aggregate (Figure 3.1). These aggregates were provided by TxDOT's Construction Division in Austin. TxDOT's Construction Division regularly monitors the properties of aggregates produced in different sources based on the following tests:

- Abrasion of Coarse Aggregate Using the Los Angeles Abrasion Machine
- Soundness of Aggregate by Use of Magnesium Sulfate
- Degradation of Coarse Aggregate by Micro-Deval Abrasion
- Acid Insoluble Residue for Fine Aggregate

In Texas, the above tests are related to the frictional and durability properties of aggregates. Based on the results of these tests, aggregates are classified as Surface Aggregate Classes A through C. Class A, B, and C are allocated to the groups of aggregates that show high, moderate, and low frictional and durability characteristics respectively. The Surface Aggregate Classification is used in the Texas Wet Weather Accident Reduction Program (Behrens, 1999) to select appropriate materials for different regions with various friction demands.

The name of quarry, material type, and friction and durability test results of the selected aggregates for this research study are provided in Table 3.1. As this table indicates, group A of aggregates belongs to Surface Aggregate Classification (SAC) A and the other group was selected from SAC B. Figure 3.2 provides micro-scale view of 2.34 mm² of aggregates A and B, captured by microscope, in two modes: Intensity (the intensity of the reflected light for each pixel), and Range (height of each pixel) (Laurent, 2014).

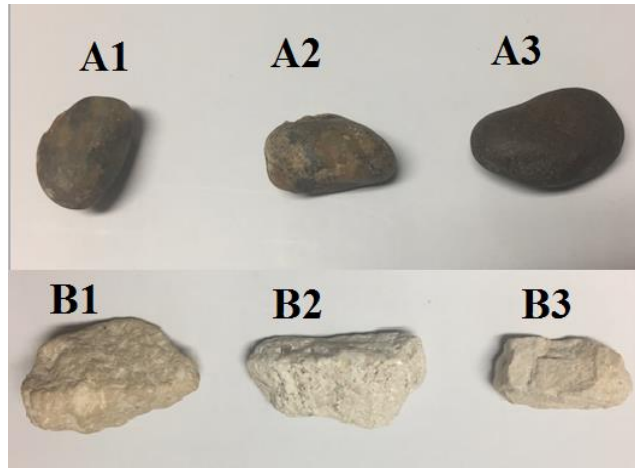


Figure 3.1 Aggregate particles

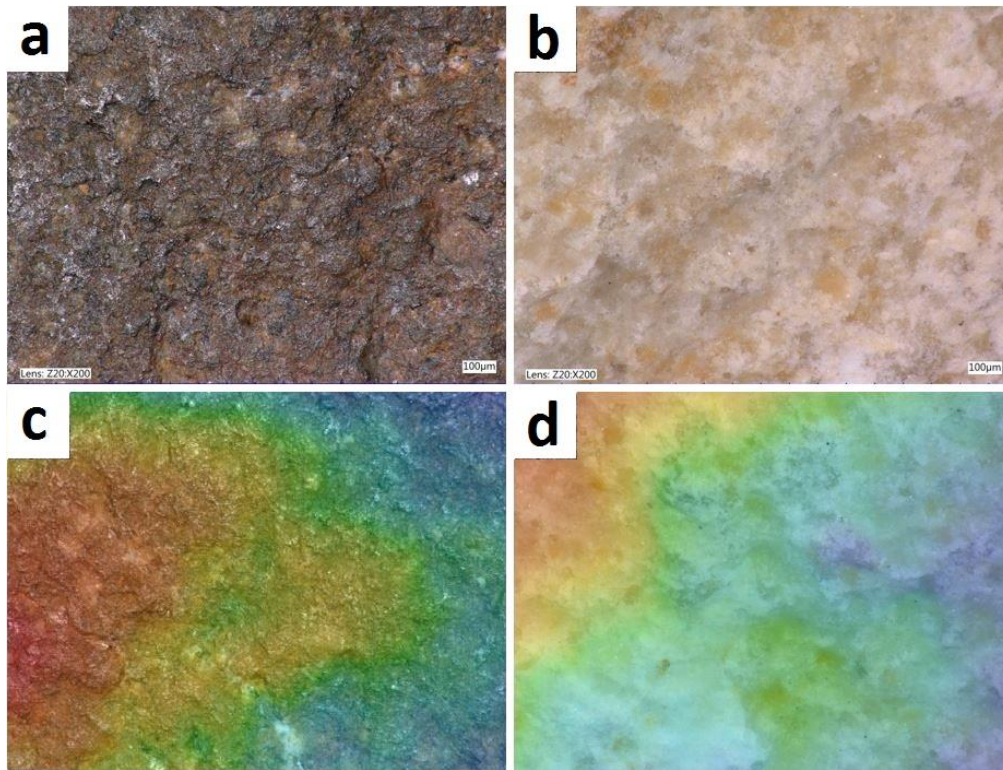


Figure 3.2 Microscopic view of texture surfaces of a) “intensity” of aggregate A, b) “intensity” of aggregate B, c) “range” of aggregate A, and d) “range” of aggregate B

Table 3. 1 Aggregates Properties (BRSQC, 2016)

Aggregate	Quarry	Used for	Material	Surface Aggregate Classification	RSLA	RSSM		RSMD	CA-RSAI
						HMAC	ST		
Aggregate A	Big Creek Sand & Gravel, Inc. Bear Creek Pit	HMAC, Surface treatment	Crushed Siliceous and Limestone Gravel	A	37	18	13	13	90
Aggregate B	Jones Brothers - Rankin	HMAC, Surface treatment	Crushed Limestone	B	30	28	24	24	1

RSLA: Rated Source Los Angles Abrasion
 RSSM: Rated Source Soundness Magnesium
 RSMD: Rated Source Micro-Deval
 HMAC: Hot Mix Asphaltic Concrete
 ST: Surface Treatment
 CA: Coarse Aggregate
 RSAI: Rated Source Acid Insoluble

The aggregates were first washed in order to remove any dust and undesirable particles. Then, the aggregate particles were oven-heated to 160°C for 24 hours followed by 4 hours of regulated air temperature and humidity to reach air-dry condition. The samples were scanned individually using the developed LLS prototype in Y-direction with resolution of 25 microns. During measurement, the optimum distance between the laser and aggregate samples was kept at 80 mm. Because the mechanism of the laser is based on projecting a light and capturing its reflection, all tests were performed in a laboratory with constant light condition to avoid any further signal noise associated to the light variation. Along with the light, the room temperature and humidity, 23°C and 45% respectively, were also kept constant during the experiments. The height profile located at the middle of each aggregate surface was selected for analysis.

3.3. Numerical Methods

A signal is a function of an independent variable, usually time or space, and it is generally used to describe physical phenomena over time or distance (Hsu, 1995; Oppenheim et al., 1998). Accordingly, the height profile captured from the aggregate surface can be considered as a signal. Signal processing theorems such as Fourier analysis and power spectral density (PSD) were employed to extract the embedded information in height profiles. Fourier analysis helps to show what wavelengths are included in a height profile and in what proportions. This section first provides a summary of types of signals and then presents explanations of Fourier Transform (FT) and PSD theorems. It is to be noted that this section focuses on time signals to explain the concepts, however the descriptions and theories can be applied to spatial signals.

Generally, signals can be categorized into the groups described in the following subsections.

3.3.1. Continuous and Discrete Signals

If a signal is defined as a function $x(t)$ where t is time, then the signal is continuous when t is continuous. On the other hand, if $x(t)$ happens at discrete times, $x(t)$ is classified as a discrete signal and represented by $x(t_n)$ or $x[n]$, where n is an integer (Hsu, 1995; Oppenheim et al., 1998). Figures 3.3(a) and 3.3(b) provide an example of continuous and discrete-time signals, respectively.

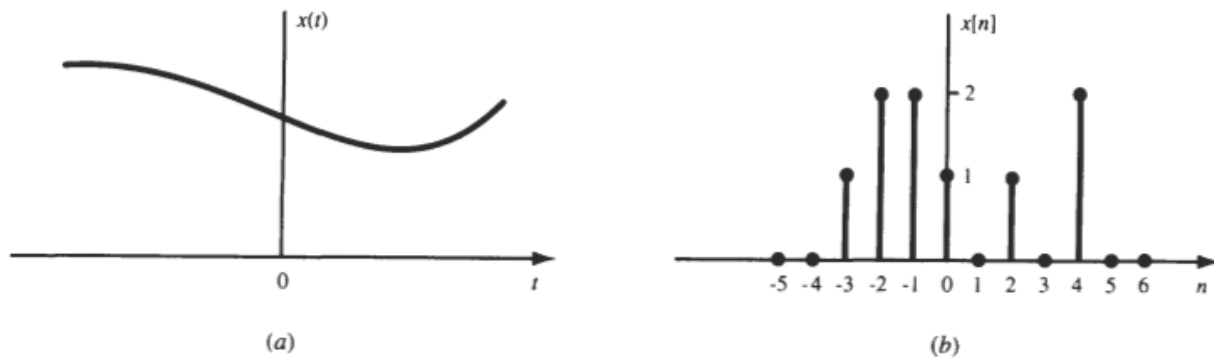


Figure 3.3 Graphical example of (a) continuous- and (b) discrete-time signals (Hsu, 1995)

3.3.2. Analog and Digital Signals

A signal $x(t)$ is analog if it happens in a continuous time interval, (t_1, t_2) (Hsu, 1995). Most of real phenomena in the world like the surface of aggregates are modeled by analog signals, but they cannot be analyzed using digital computers. To store and process analog signals using computers, they need to be converted to digital signals (Baraniuk, 2009). A digital signal is a set of discrete samples picked from a continuous signal at a given sampling interval (Hsu, 1995). Figure 3.4 shows an example of an analog and its digital samples. To digitize an analog signal, sufficient sampling is required to retain the information of that signal. In order to obtain valid data, sampling must occur at a particular time or distance called the sampling interval (Δ). The proper sampling interval is dictated by the largest frequency (Nyquist frequency) or the smallest period of interest. According to the sampling theorem, at least two samples must be considered for every cycle of the Nyquist frequency (f_N). In other words, the rate of sampling, f_s , should be at least twice of the f_N (Olshausen, 2009).

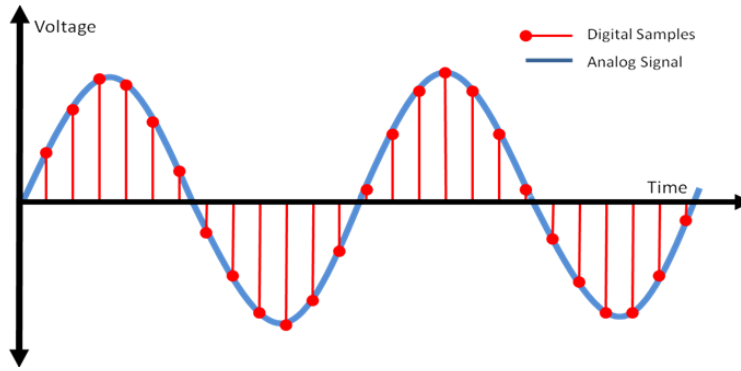


Figure 3.4 Example of analog and digital sampling (Alazartech)

Periodic and non-periodic signals:

A signal $x(t)$ is periodic provided that $x(t + T) = x(t)$ for all t . Figure 3.5 provides an example of a continuous periodic function with a period T equals to 2π . A periodic signal with period T , is also periodic with $K \cdot T$, where K is an integer number. The smallest T that satisfies the above condition is called the fundamental period of $x(t)$. It is to be noted that the period in space is measured by the wavelength λ (Osgood, 2007).

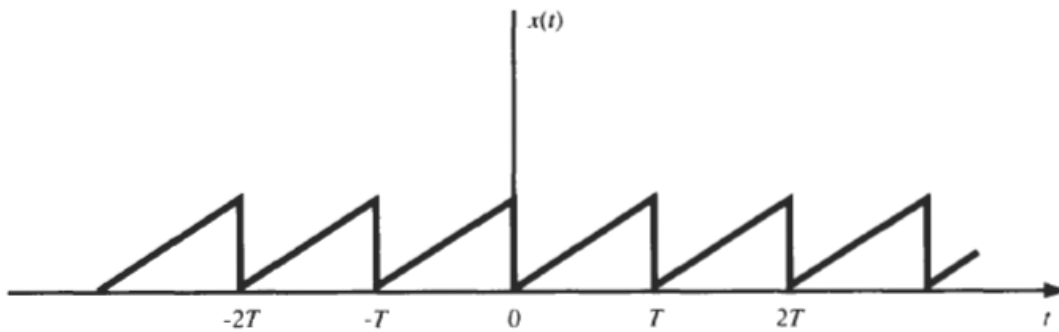


Figure 3.5 Example of a periodic continuous signal (Hsu, 1995)

Identically, a periodic discrete signal is a signal with the fundamental period N (a positive integer) that obeys the Equation 3.1. This signal is also periodic with $m \cdot N$, where m is an integer (Hsu, 1995).

$$x[n + N] = x[n] \text{ for all } n \quad \text{Equation 3.1}$$

Frequency of a signal is inversely related to the period through Equation 3.2; hence, given the period, one can calculate the frequency of a signal and vice versa (Mari et al. 1999).

$$\text{For a time signal: } T = \frac{1}{f} \quad \text{Equation 3.2}$$

$$\text{For a spatial signal: } \lambda = \frac{1}{f}$$

where f is frequency and T (or λ) is period.

3.3.3. Fourier Transform

According to the Fourier theory, all signals could be represented as the sum of sinusoidal waves of various amplitudes and frequencies. This approach helps to find the amplitudes corresponding to those sinusoids (Karrenberg, 2013; Yoo, 2001). Generally, Fourier analysis includes two parts: 1) Fourier series, and 2) FT. The former decomposes a periodic function into the sum of sinusoidal functions, whereas the latter expands general functions that are not necessarily periodic (Putman, 2007).

This section provides the FT formulation by which a non-periodic signal can be represented in the frequency domain. Figure 3.6-top shows a non-periodic finite wave that covers the time ranges between $-T_1$ and T_1 and is equal to zero outside of that range (Hsu, 1995). A periodic signal $x_{T_0}(t)$ (as shown in Figure 3.6-bottom) can be produced by repeating $x(t)$ with an arbitrary period of T_0 such that $\lim_{T_0 \rightarrow \infty} x_{T_0}(t) = x(t)$. The FT representation of $x_{T_0}(t)$ is expressed as Equation 3.4.

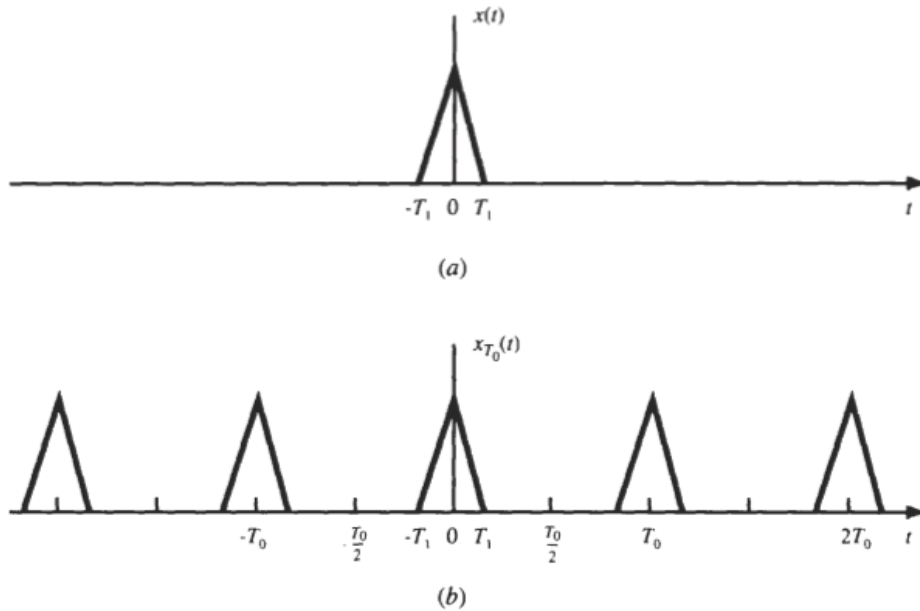


Figure 3.6 A non-periodic (top) and a periodic signal (bottom) (Hsu, 1995)

$$x_{T_0}(t) = \sum_{k=-\infty}^{\infty} C_k e^{i2\pi(\frac{k}{T_0})t} \quad \text{Equation 3.4}$$

where T_0 is period, k only gets integers from $(-\infty, \infty)$, i is equal to $\sqrt{-1}$, and C_k is known as the Fourier coefficient and is calculated using Equation 3.5.

$$C_k = \frac{1}{T_0} \int_{-\frac{T_0}{2}}^{\frac{T_0}{2}} x(t) e^{-[2\pi i (\frac{k}{T_0})t]} dt \quad \text{Equation 3.5}$$

Since $x(t)$ is zero outside of $(-T_1, T_1)$, the Fourier coefficient C_k for the non-periodic signal $x(t)$ can be rewritten as Equation 3.6:

$$C_k = \frac{1}{T_0} \int_{-\infty}^{\infty} x(t) e^{-[2\pi i (\frac{k}{T_0})t]} dt \quad \text{Equation 3.6}$$

3.3.4. Discrete Fourier Transforms (DFT)

Consider a discrete function $x(t)$ with N points at an interval of $\Delta T = 1$. Therefore, we have a discrete function, $x[n]$, with length of $N\Delta T = N$, and a finite number of samples. Discrete Fourier series (DFT) is the Fourier transform of this sampled function that transforms N discrete points of the signal to the N equally spaced discrete frequencies.

Using the DFT, we can transform a given function from time domain to frequency domain. In the case where we have $x[n]$, DFT provides the Fourier coefficients C_k (Oppenheim et al., 2009; Orfanidis, 1995). Equations 3.7 show the DFT formulation.

$$C_k = \frac{1}{N} \sum_{k=0}^{N-1} x[n] e^{-[2\pi i (\frac{k}{N})n]} \quad \text{Equation 3.7}$$

DFT is accomplished using effective computational algorithms: FFT in Matlab (Mathworks).

3.3.5. Power Spectral Density (PSD)

PSD is an analysis in the frequency domain that provides the power associated with constituent frequencies of a signal (Benbow et al., 2006; Elson and Bennett, 1995). In this case, the PSD provides the constituent wavelengths of a height profile. The PSD of a signal $x(t)$ can be calculated using Equation 3.8:

$$PSD = \frac{1}{N} \sum_{k=0}^{N-1} |C_k|^2 \quad \text{Equation 3.8}$$

where N is the total number of Fourier frequencies and C_k is the Fourier coefficients of the signal $x(t)$.

3.3.6. Root Mean Square Roughness and Depth of Surface Smoothness

Two parameters—the root mean square roughness (Rq) and the depth of surface smoothness (Rp)—were considered as quantitative measurement of aggregates surface friction. A research study conducted by Cafiso and Taormina found that there was a good correlation between these two parameters and surface friction (Cafiso and Taormina, 2007). Rq and Rp (calculated by Equations 3.9 and 3.10) are two statistical indicators obtained from the height profile of the aggregate surface and found to have significant correlation with the British Pendulum Number (BPN), which is widely used to measure pavement surface friction (Cafiso and Taormina, 2007).

$$Rq = \sqrt{\frac{1}{N} \sum (Z_i - \bar{Z})^2} \quad \text{Equation 3.9}$$

$$Rp = \frac{1}{N} \sum_i (Z_{max} - Z_i) \quad \text{Equation 3.10}$$

where Z_i is the generic ordinate, \bar{Z} is the average of Z_i values, Z_{max} is the maximum Z value, and N is the number of points.

The PSD parameters and height profile parameters were calculated for all aggregate particles to study the effect of the aggregate's micro-scale texture on its surface friction.

3.4. Result and Discussion

3.4.1. Effect of Orientation

In principle, aggregates tend to randomly arrange within the pavement surface layer. Hence, studying the aggregates' characteristics associated with surface texture using PSD plots might be affected by aggregates' orientations. To investigate the effect of orientation, aggregate A1 was scanned in four different directions ranging from 0° to 270° with an interval of 90° , as shown in Figure 3.7. The black areas in Figure 3.7 are the missing data in which the camera was not able to detect the laser line reflected from the aggregate surface specifically in the edges. For the texture measurement, these black areas did not have an effect on the results. Subsequently, the data were analyzed and the PSD values were plotted with respect to wavelengths in Figure 3.8. This figure shows that the PSD plots of different orientations cannot be differentiated and that all follow a similar pattern, so it was concluded that the orientation of aggregate particles does not have a significant effect on PSDs. These results are consistent with the outcomes of a study conducted by Wang et al., which indicated that the influence of aggregate orientation in profile images is negligible (Wang et al., 2005).

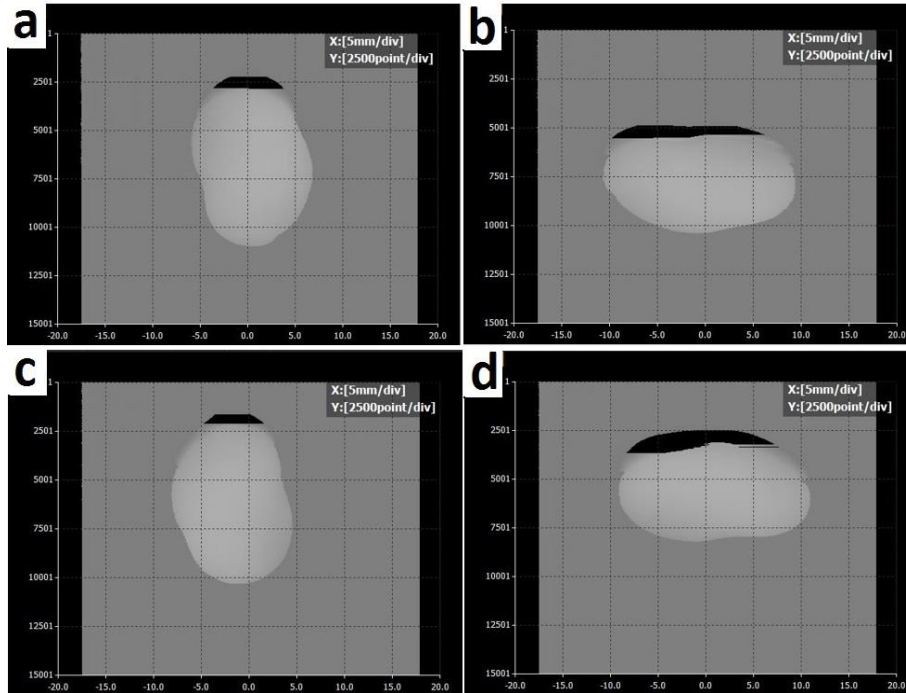


Figure 3.7 Scan of A1 in different angles a) 0°, b) 90°, c) 180°, and d) 270°

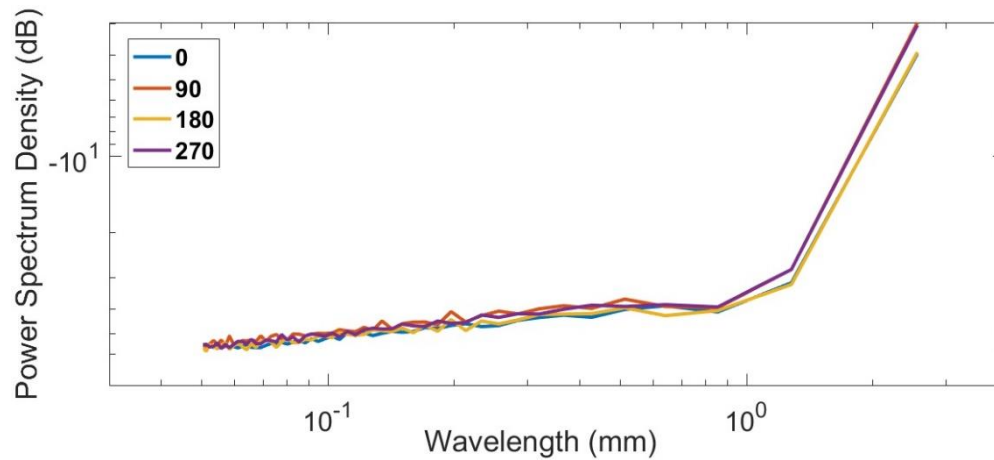


Figure 3.8 PSD of Aggregate A1 in different angles

3.4.2. Comparison of PSD Results

Figure 3.9 presents the PSD of two aggregate groups: A and B. According to this figure, the PSD values of aggregates within each group are similar in the first decade of micro-texture. Slight differences were observed in the first decade of macro-texture, which can be due to size variation of particles. These results suggest that the PSD of the aggregates in the first decade of micro-texture significantly depends on the mineralogical properties of the aggregates. Therefore, it can

be concluded that aggregates obtained from the same source behave similarly in the first decade of micro-texture.

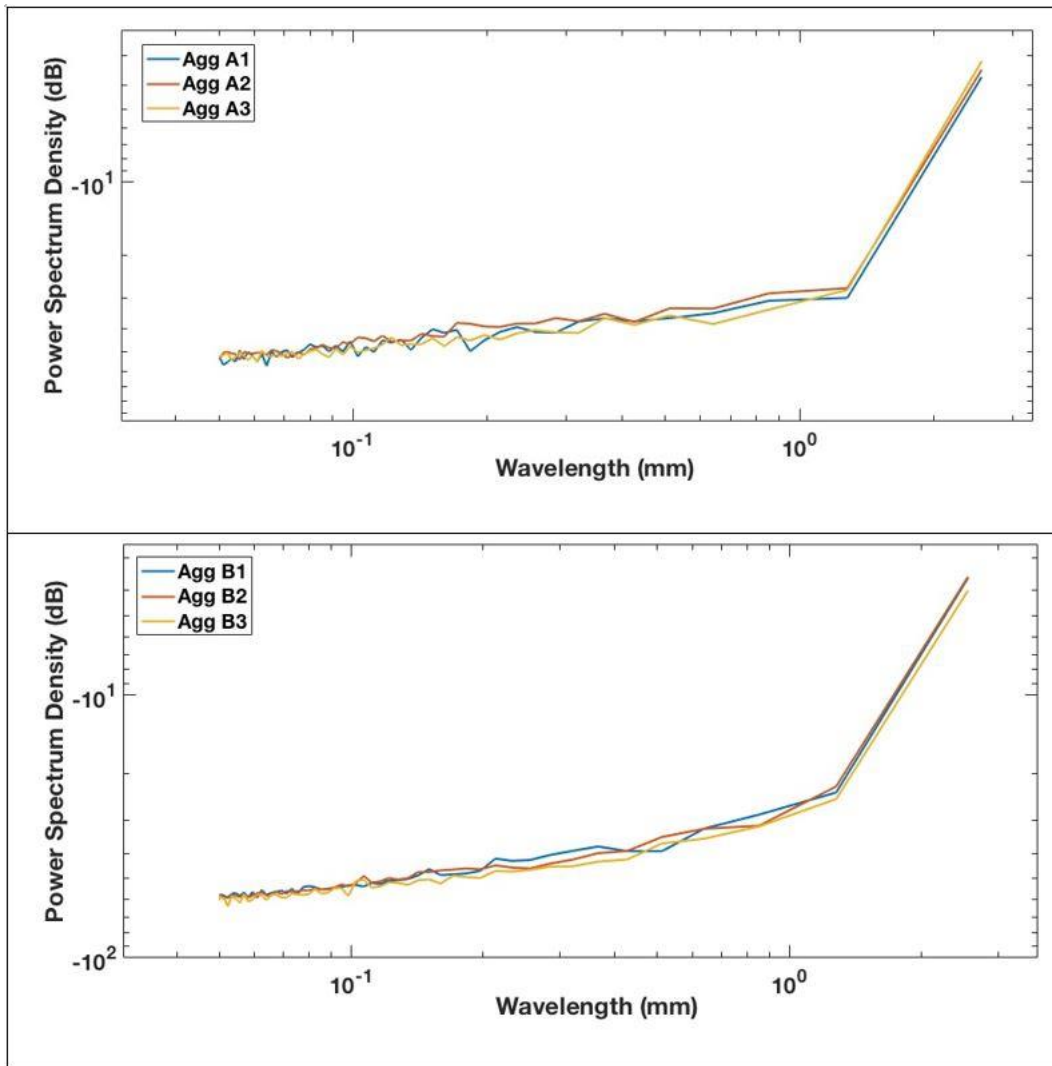


Figure 3.9 Comparison of PSD values of all aggregates

3.4.3. Paired t-test

To better quantify the aggregates' surface characteristics that contribute to the texture, two levels of wavelengths (first decade of micro-texture and first decade of macro-texture) were broken into smaller sub-bands so that the aggregates could be compared and analyzed in each sub-band in terms of their PSD values. For this purpose, the paired t-test was used. Table 3.2 provides the wavelength range of each sub-band along with the results of its paired t-test. The null hypothesis was that there is no statistical difference between the mean PSD values of aggregate A and aggregate B. According to the paired t-test results, the PSD data for aggregates in all micro-texture sub-bands can be differentiated; however, the test failed in the macro-texture sub-bands, indicating

that the PSD in those sub-bands could not be differentiated. Hence, the macro-texture data were eliminated and the micro-texture data were used for further investigation.

Table 3. 2 Sub-bands of Classification of Wavelengths

Sub-band	Range (mm)	t stat	P-value	Possibility of Differentiation
First part of micro-texture (L1)	0.05 – 0.075	19.9	0.00	Yes
Second part of micro-texture (L2)	0.075 – 0.1	25.6	0.00	Yes
Third part of micro-texture (L3)	0.1 – 0.25	11.2	0.00	Yes
Fourth part of micro-texture (L4)	0.25 – 0.5	6.54	0.002	Yes
First part of macro-texture (L5)	0.5 – 1.0	1.44	0.29	No
Second part of macro-texture (L6)	1.0 – 2.56	-1.46	0.38	No

3.4.4. Evaluation of Root Mean Square Roughness and Depth of Surface Smoothness

The spatial signals captured with the LLS from the aggregate’s surface texture were processed using band-pass filters in order to separate the micro-texture components. The profiles in the frequency domain were cut off between the wavelengths 0.05 to 0.075 mm, 0.075 to 0.1 mm, 0.1 to 0.25 mm, and 0.25 to 0.5 mm. These cut-off wavelengths were selected based on the defined sub-bands in Table 3.2 for the first decade of micro-texture. The filtered profiles were subsequently used to compute the texture parameters R_q and R_p at different levels of micro-texture. As an example, Figure 3.10 shows the height profile of aggregate A1 along with the four filtered profiles that were used to calculate the R_q and R_p value.

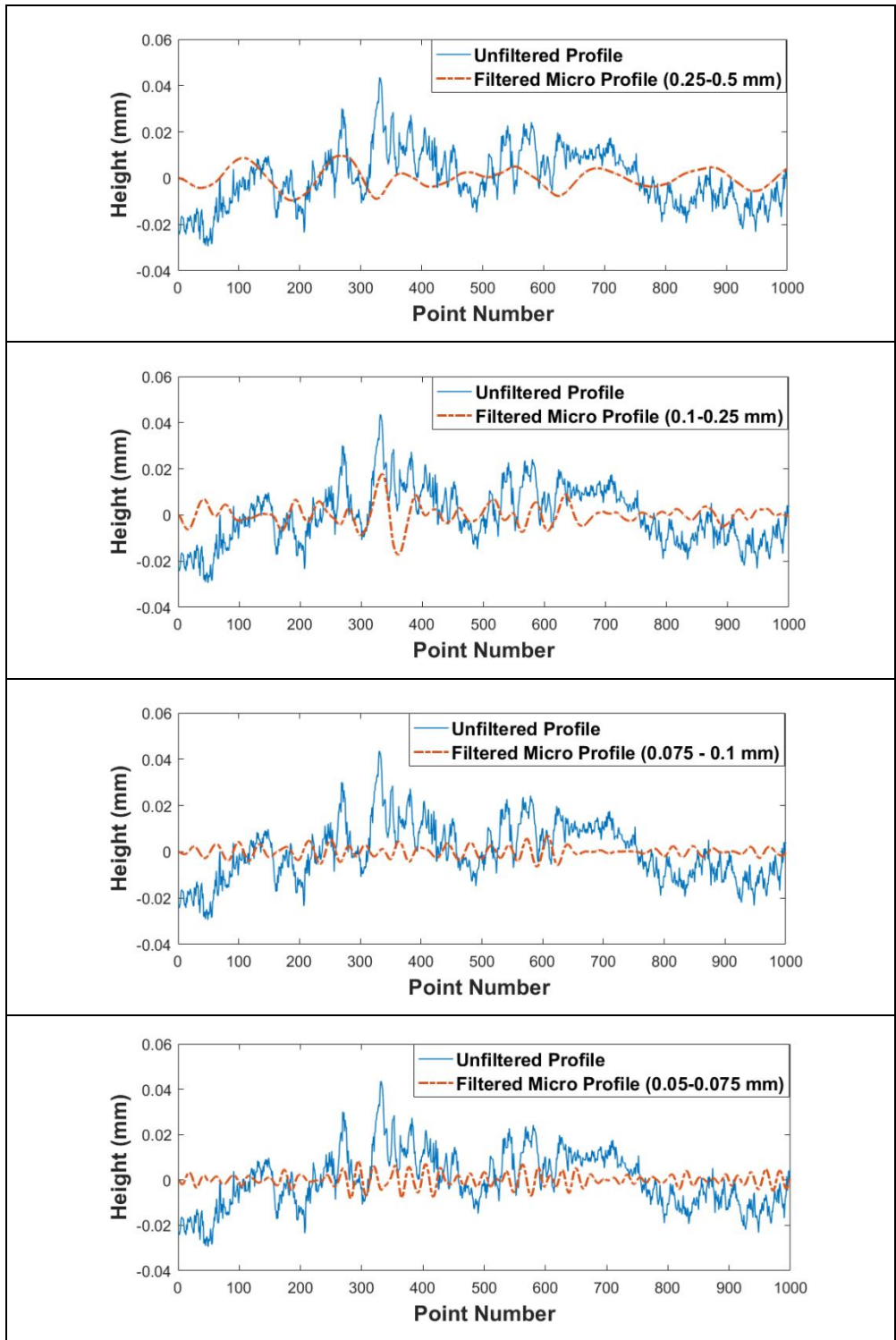


Figure 3.10 The profile of aggregate A1 with the micro-scale filtered profile

Figures 3.11 and 3.12 show the texture parameters R_q and R_p calculated in different sub-bands (L1 through L4). As these figures demonstrate, the R_q and R_p values of aggregate type A is significantly higher than those in aggregate type B in all sub-bands except L4 (0.25-0.5 mm). These findings can be interpreted to indicate that the aggregate type A has higher friction, which is consistent with the findings arising from the PSD plots. The difference between the R_q and R_p values is more significant in sub-bands L1 (0.05-0.075 mm), L2 (0.075-0.1 mm), and L3 (0.1-0.25 mm), potentially suggesting that lower wavelengths in surface micro-texture have higher impact on the surface friction behavior of aggregates.

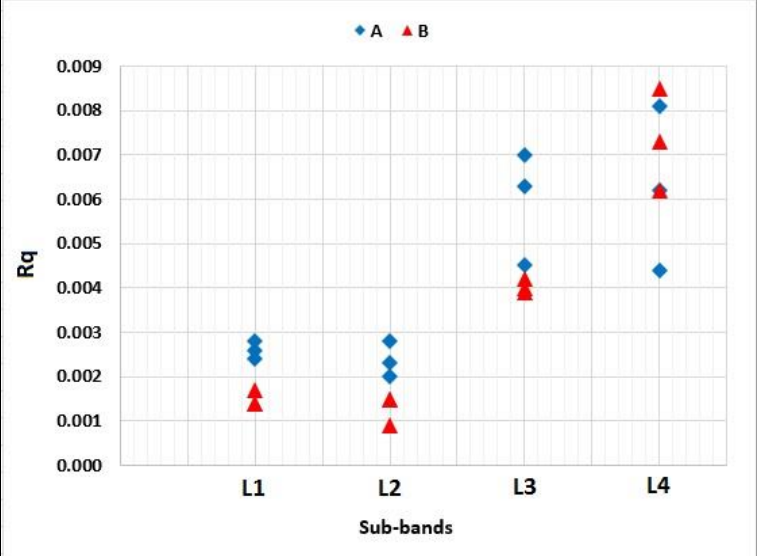


Figure 3.11 Root mean square roughness values in different sub-bands of wavelengths

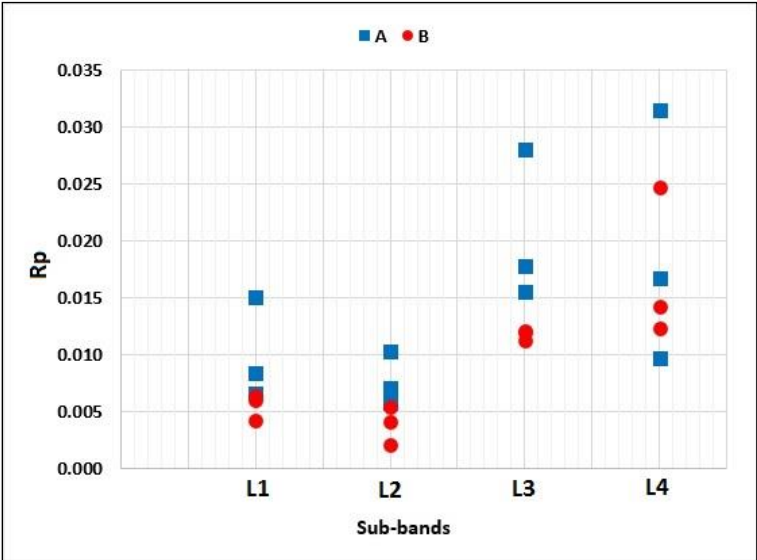


Figure 3.12 Values of depth of surface smoothness in different sub-bands of wavelengths

Table 3.3 provides a comparison between the texture parameters used in this study to differentiate aggregates in different ranges of wavelength. According to the table, the results of PSD, Rq, and Rp were consistent only in the wavelength range of 0.05 to 0.25 mm. It can be concluded that this range has the most effect on the aggregate surface texture. This the LLS demonstrated to be capable of differentiating between the micro-texture of the different aggregates, and therefore has the potential to be incorporated into the SAC classification to assess the friction potential of the aggregate particles.

Table 3. 3 Side-by-side Comparison of Texture Parameters in Different Wavelength Ranges

Texture Parameters	Wavelength Range (mm)					
	Micro-texture				Macro-texture	
	L1 (0.05-0.075)	L2 (0.075-0.1)	L3 (0.1-0.25)	L4 (0.25-0.5)	L5 (0.5-1.0)	L6 (1.0-2.56)
PSD	✓	✓	✓	✓	X	X
Rq	✓	✓	✓	X	NA	NA
Rp	✓	✓	✓	X	NA	NA

Chapter 4. An Automatic Method for Measuring Pavement Macro-Texture

4.1. Introduction

Mostly, highway agencies and DOTs rely on the SPT for pavement macro-texture measurement. Although the SPT is relatively simple and inexpensive, this test is subject to human errors and is affected by low repeatability and reproducibility. In recent years, efforts have been made to quantify the mean texture depth (MTD) of pavement surfaces by using two-dimensional (2D) surface profiles. For more comprehensive and accurate measurements of the texture depth, three-dimensional (3D) surface data are needed. No method has yet been provided for calculating the MTD using 3D models of the pavement surface. This study employed the 3D laser scanner developed at the University of Texas at Austin and proposed an algorithm to calculate the MTD based on 3D pavement data.

4.2. Research Methodology

4.2.1. Field-Data Collection

In this study several field tests were performed to collect data using the 3D laser scanner, measure the MTD using the SPT, and assess the variability of the SPT and the developed prototype. Nine test locations across Texas were selected. The chosen locations have different mix designs, ensuring a wide variety of surface textures. The test locations and their pavement mix designs are provided in Table 4.1. At each location, two sections were tested and scanned in the right wheel path. In each section, the SPT was conducted within the scanned pavement surface to provide consistent texture measurements. The SPTs were performed, as illustrated in Figure 4.1, according to the ASTM E965 Standard.

Table 4.1 Selected Test Locations

Test Location No.	District/Location	Pavement Mix design
1	Speedway St, Austin	Dense-Graded Type D
2	FM 1626, Austin	Thin Overlay Mixtures
3	RM 12, Austin	Thin Overlay Mixtures
4	FM 1431, Austin	Porous Friction Course
5	IH 20, Brownwood	Dense-Graded Type D
6	SH 36, Brownwood	Dense-Graded Type C
7	SH 195, Austin	Porous Friction Course
8	US 84, Bryan	Dense-Graded Type C
9	US 181, San Antonio	Novachip



Figure 4.1 3D Laser scanner and sand patch test

4.2.2. Sand Patch Test Computer Simulation

This section describes the development of a new automated MTD measuring algorithm. Once the surface data acquisition was complete, the scans were subjected to a preliminary filtering step. The filtering step is required because ignoring this step while creating the 3D models of the pavement surfaces could result in the miscalculation of the MTD. The outlier readings that must be removed are the portions that do not belong to the test section or were not captured by the laser detector. These outliers are the scanned points with invalid depth values. The filtering algorithm also removes the slope from the laser data. Examples of unfiltered and filtered pavement data are shown in Figure 4.2.

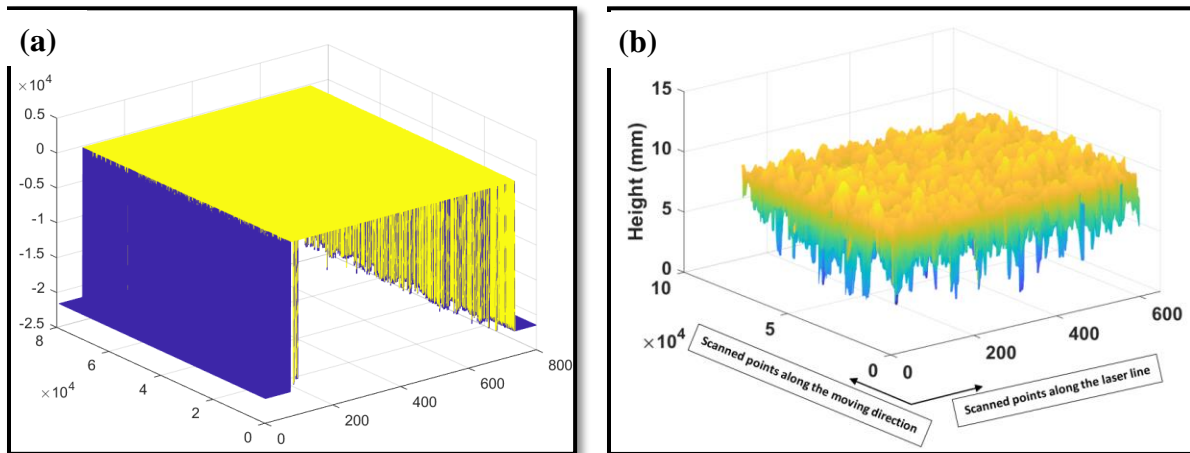


Figure 4.2 Laser measurement data a) before and b) after the filtering process

Previous studies have demonstrated that a reference line or point is required in the calculation process of the MTD (22,23). For instance, the ARAN software considers the point with the maximum height value as the reference to calculate the MTD of a road profile. However, for pavements with a few large surface stones or debris, the maximum height value could overestimate

the MTD. Accordingly, the first consideration in developing this simulation regards the choice of a general reference point. As seen in Figure 4.3(a), the sand filled the pavement surface voids, covering most but not all the peaks. An understanding of how high the sand typically fills the pavement surface depressions helps in deriving a general reference plane.

For this purpose, a MATLAB algorithm was developed to simulate the SPT on the 3D models of the pavement surfaces. For each test section, the area covered by the patch of sand (shown in Figure 4.3(a)) was calculated using the average diameter. To simplify the simulation process, a rectangle with an area equivalent to that of the circle was fitted on the pavement models in the same location as the SPT, as depicted in Figure 4.3(b). The width of the rectangle is equal to width of the scanned area. The length of the rectangle is equal to the calculated SPT area divided by the rectangle width. The center of the rectangle coincides with the center of the computer-generated surface model. Afterwards, the considered area was extracted (as shown in Figure 4.3(c)) and inputted into an iterative algorithm for the MTD calculation.

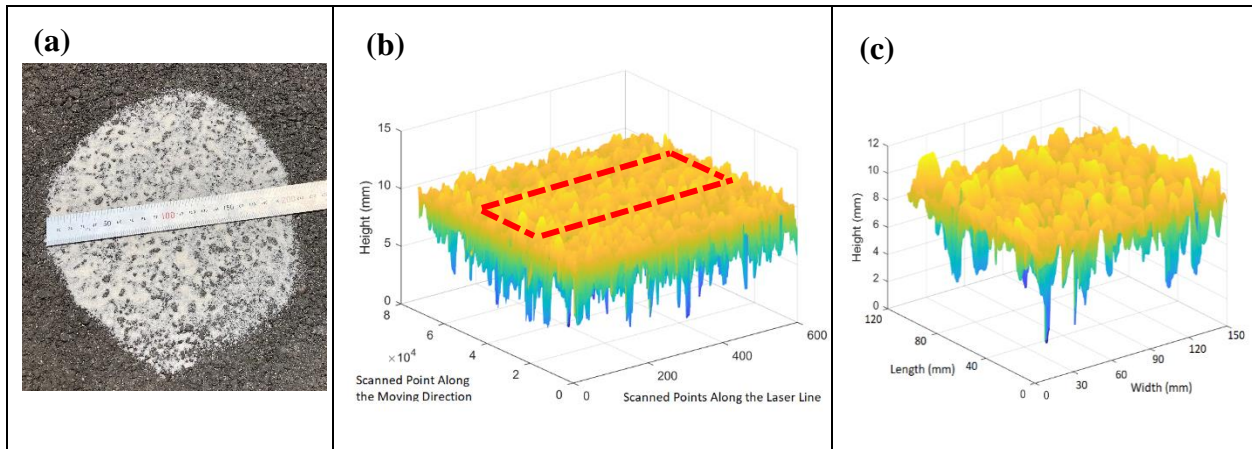


Figure 4.3 Schematic representation of a) the area of the sand patch on a pavement and b) the fitted rectangle on the corresponding 3D pavement model, and c) the data within the rectangle

A schematic illustration of the iterative algorithm is presented in Figure 4.4. In this iterative algorithm, the reference height is simulated at different percentile values of heights ranging from the 50th to 100th percentile. In each iteration, a uniform horizontal plane is created with a height equivalent to the iterated percentile value, i.e., from the 50th to the 100th. This plane intersects the pavement section, as shown in Figure 4.4, and the sand is assumed to fill the voids up to that height value. The pavement surface points below the reference plane are identified and counted. Then, the vertical distance between each point and the horizontal plane is calculated. Afterwards, the MTD is estimated as the mean of the vertical distances. The MTD values obtained from the SPT were compared to those obtained from the algorithm in order to determine a proper reference plane. ability to create a circular patch.

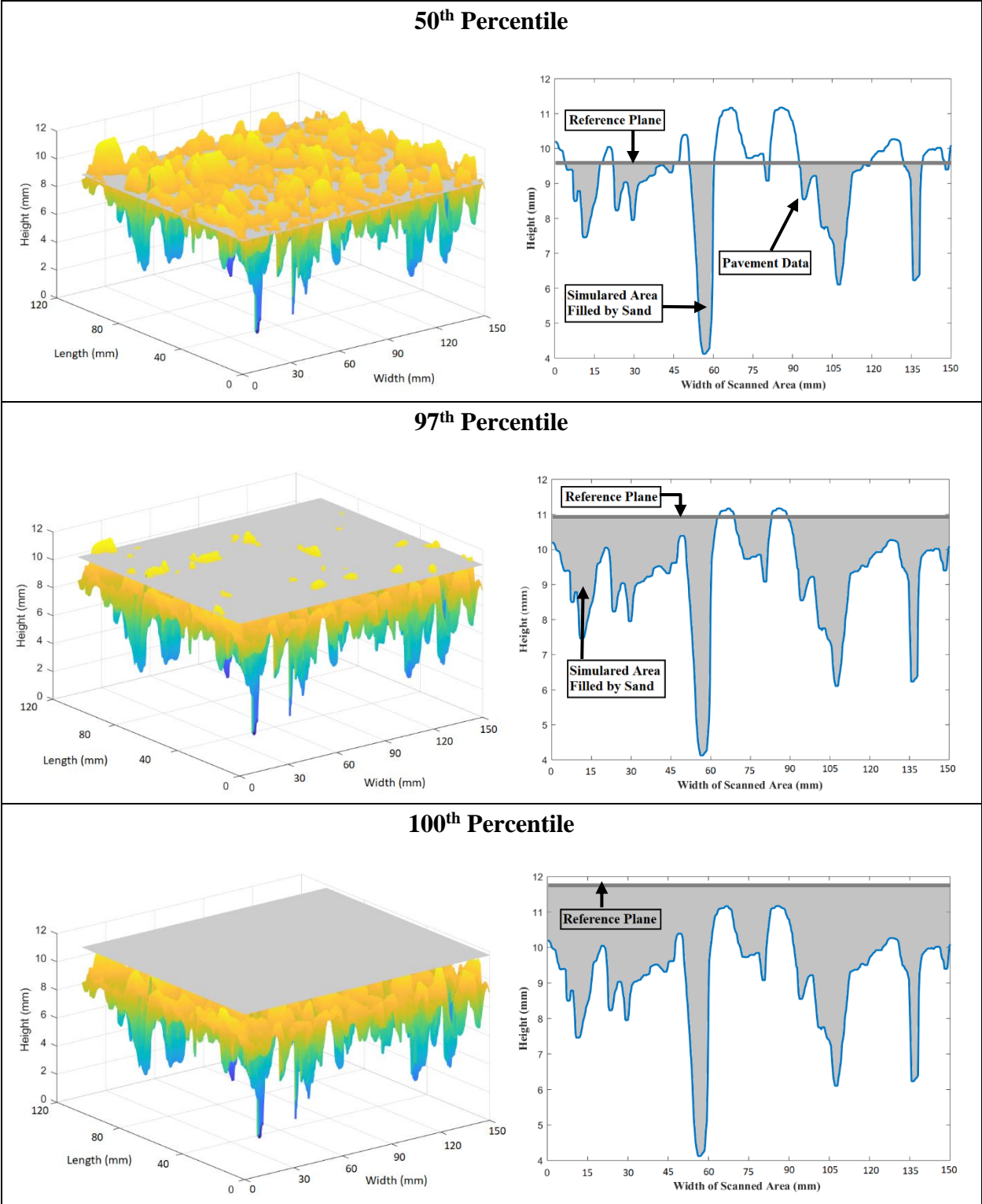


Figure 4.4 3D representation of the uniform, horizontal plane intersecting the pavement model at 50th, 99th, and 100th percentiles and 2D view of the simulated area between the crossing plane and the lower data points filled by sand

4.3. Results and Discussions

4.3.1. Variability of the SPT

In an effort to address operator's dependency of the SPT, the following field test was performed on two sections in Speedway Street in Austin, Texas. Seventeen operators each conducted one SPT per section, yielding a total of 34 tests. In each section, every operator performed their SPT attempt in the same location in order to limit any bias generated by surface non-homogeneity. Each operator measured the diameter of the sand patch four times along different axes.

Figure 4.5 provides the box plot of the measured diameters for seventeen operators in two different test sections. These boxplots show the lowest and highest diameters, the first and third quartiles, the median represented by a horizontal line, and the mean (indicated with an "X" mark). These plots illustrate the variation of the diameter measurements between the operators. It is evident that the sand patch results highly depend on the operator's perception of the edges of the sand patch.

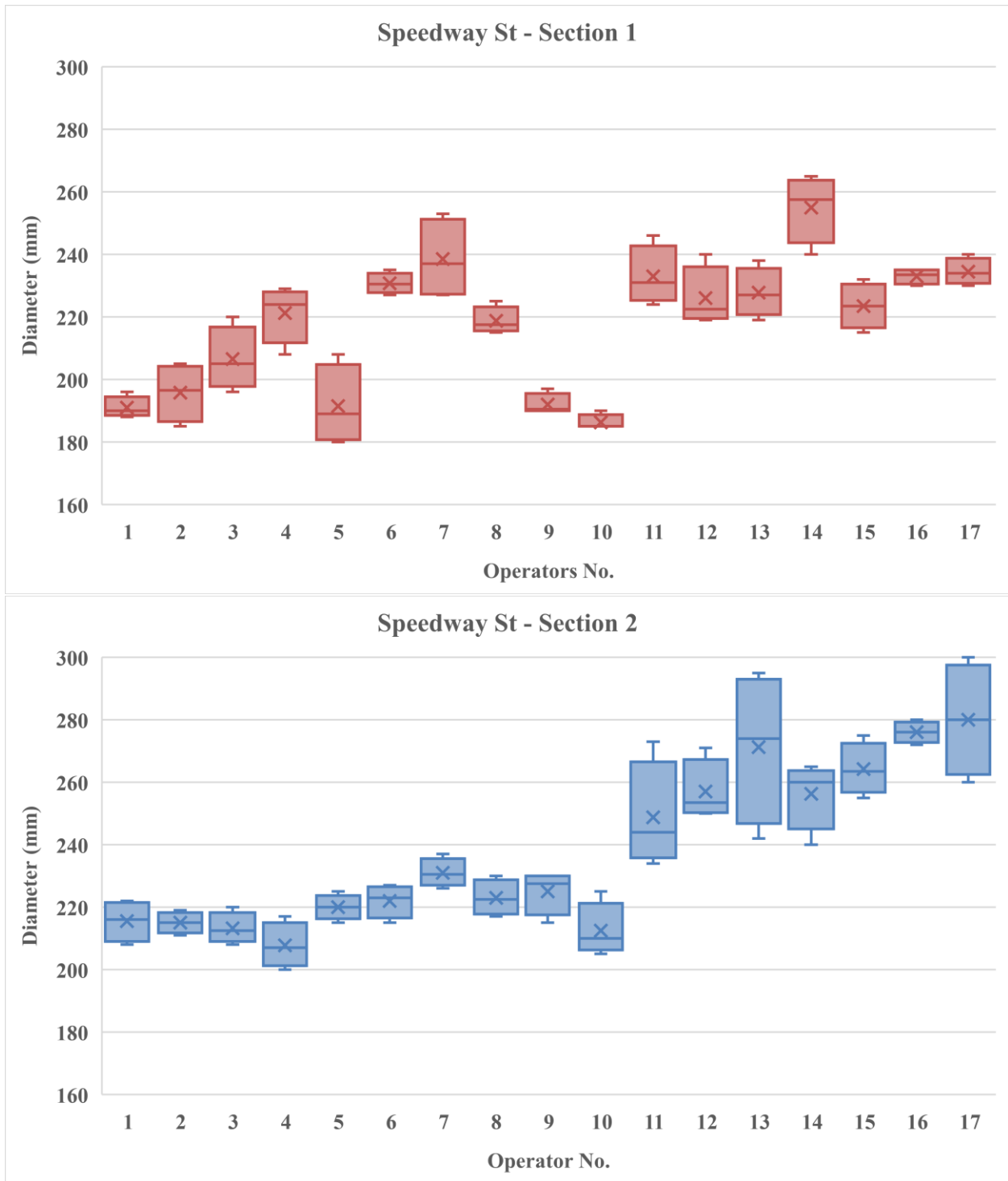


Figure 4.5 Box plots of the measured diameters by the different operators on two sections.

In addition to descriptive plots, a statistical analysis was performed on the measured diameters using one-way analysis of variance (ANOVA). This method compares the means of different groups (the means of diameters measured by operators in this case). The ANOVA tests the non-specific null hypothesis that all operators' means are equal. If the null hypothesis is rejected, then

it can be concluded that at least one of the operator's mean is different from at least one other operator's mean. This means that the underlying factor—the operator in this case—has a statistically significant effect on the measured diameters. If the null hypothesis is accepted, then it can be concluded that the operators' means are equal, and the operator does not have an effect on the measured diameter. A comprehensive explanation of the ANOVA calculations can be found in (24). It should be noted that the statistical p-value represents the probability that the means are the same and the factor is insignificant. Table 4.2 shows the ANOVA outputs. The results indicate that the p-values for both test sections are less than the significance level of 0.05. This indicates that the means are different, the null hypothesis is rejected, and the operator has a significant effect on the measured diameters.

Table 4.2 ANOVA Outputs of the Sand Patch Measurements

One-Way ANOVA – Underlying Factor: Operator							
Speedway St – Section 1				Speedway St – Section 2			
Operators No.	Measured Diameters per SPT	Average	Variance	Operators No.	Measured Diameters per SPT	Average	Variance
1	4	191	12.0	1	4	215.5	43.7
2	4	195.8	87.6	2	4	215	11.3
3	4	206.5	101.7	3	4	213.3	24.9
4	4	221.3	84.3	4	4	207.8	51.6
5	4	191.5	163.0	5	4	220	16.7
6	4	230.8	10.9	6	4	222	28.0
7	4	238.5	169.7	7	4	231	20.7
8	4	218.8	18.9	8	4	223	32.7
9	4	192	11.3	9	4	225	50.0
10	4	186.3	6.3	10	4	212.5	75.0
11	4	233	88.7	11	4	248.8	289.6
12	4	226	91.3	12	4	257	94.0
13	4	227.8	61.6	13	4	271.3	590.9
14	4	255	116.7	14	4	256.3	122.9
15	4	223.5	52.3	15	4	264.3	68.9
16	4	233	6.0	16	4	276	11.3
17	4	234.5	17.7	17	4	280	333.3
ANOVA Results – Section 1				ANOVA Results – Section 2			
Variation Source	SS	df	MS	Variation Source	SS	df	MS
Between Group	26468.3	16	1654.3	Between Group	40180.3	16	2511.3
Within Group	3299.5	51	64.7	Within Group	5596.5	51	109.7
Total	29767.8	67		Total	45776.8	67	
F - Statistic	25.6			F - Statistic	22.9		
P- value	7.5E-19			P- value	8.4E-18		

4.3.2. Finding the Reference Plane

The MTD values obtained from the SPTs were compared to those obtained from the laser scans and the proposed algorithm. The results of this analysis are presented in Table 4.3. The highlighted value in each column represents the computer-obtained MTD closest to that obtained by the SPT. The findings indicate that in 12 out of 16 sections, a reference plane between the 96th and the 99th percentile yielded results close to the SPT. Although the results in the remaining four sections were variable, they were all above the 84th percentile of the surface data. This variability is the result of the inherent subjectivity and variability of the SPT procedure.

Table 4.3 MTD Values

Test Locations	FM 1626		RM 12		FM 1431		IH 20		SH 36		SH 195		US 84		US 181	
Test Sections	1	2	1	2	1	2	1	2	1	2	1	2	1	2	1	2
MTD Obtained by Sand Patch Test	0.750	0.734	0.474	0.472	1.236	1.338	2.330	2.290	2.037	2.087	1.600	1.780	1.183	1.243	1.364	1.334
Percentiles	MTD Obtained by Simulation Model															
50th	0.533	0.556	0.286	0.288	1.099	1.127	1.312	1.081	1.422	1.418	1.132	1.167	0.304	0.362	0.908	0.944
60th	0.527	0.557	0.290	0.290	1.118	1.127	1.417	1.244	1.481	1.513	1.125	1.177	0.334	0.427	0.909	0.955
70th	0.530	0.566	0.299	0.299	1.141	1.148	1.584	1.425	1.532	1.638	1.146	1.210	0.386	0.511	0.924	0.972
80th	0.545	0.588	0.318	0.318	1.206	1.193	1.810	1.654	1.617	1.848	1.213	1.257	0.503	0.613	0.981	1.023
81st	0.548	0.591	0.321	0.320	1.214	1.201	1.838	1.678	1.629	1.876	1.224	1.265	0.521	0.628	0.990	1.030
82nd	0.551	0.595	0.324	0.323	1.223	1.210	1.869	1.703	1.642	1.907	1.235	1.272	0.540	0.643	0.999	1.039
83rd	0.554	0.599	0.328	0.326	1.233	1.219	1.903	1.726	1.657	1.939	1.246	1.280	0.559	0.661	1.009	1.048
84th	0.557	0.603	0.331	0.329	1.244	1.229	1.937	1.752	1.671	1.974	1.259	1.289	0.579	0.681	1.019	1.057
85th	0.561	0.608	0.335	0.333	1.256	1.238	1.968	1.781	1.687	2.015	1.273	1.298	0.603	0.702	1.031	1.067
86th	0.566	0.613	0.340	0.337	1.270	1.250	2.004	1.808	1.705	2.055	1.287	1.308	0.628	0.727	1.044	1.077
87th	0.571	0.618	0.344	0.341	1.285	1.261	2.048	1.835	1.726	2.098	1.303	1.319	0.657	0.751	1.059	1.088
88th	0.577	0.624	0.349	0.346	1.302	1.275	2.097	1.867	1.749	2.146	1.323	1.333	0.686	0.779	1.075	1.100
89th	0.583	0.631	0.354	0.351	1.322	1.290	2.151	1.901	1.774	2.198	1.344	1.349	0.715	0.814	1.090	1.115
90th	0.590	0.638	0.360	0.357	1.344	1.306	2.212	1.937	1.803	2.253	1.367	1.367	0.746	0.854	1.107	1.131
91st	0.598	0.646	0.367	0.363	1.369	1.324	2.279	1.983	1.832	2.314	1.390	1.387	0.779	0.898	1.126	1.148
92nd	0.607	0.655	0.375	0.370	1.397	1.344	2.347	2.041	1.862	2.374	1.415	1.410	0.819	0.944	1.149	1.169
93rd	0.617	0.666	0.383	0.379	1.429	1.367	2.417	2.102	1.899	2.443	1.446	1.435	0.871	1.001	1.177	1.191
94th	0.629	0.678	0.393	0.389	1.466	1.393	2.510	2.163	1.944	2.524	1.486	1.464	0.928	1.074	1.210	1.215
95th	0.644	0.693	0.404	0.400	1.511	1.424	2.613	2.259	1.998	2.620	1.535	1.497	0.990	1.148	1.246	1.244
96th	0.662	0.712	0.419	0.414	1.563	1.461	2.719	2.365	2.067	2.712	1.594	1.538	1.059	1.227	1.288	1.276
97th	0.684	0.736	0.437	0.433	1.632	1.510	2.857	2.504	2.162	2.841	1.673	1.589	1.156	1.341	1.349	1.320
98th	0.711	0.773	0.462	0.460	1.726	1.584	2.992	2.729	2.279	3.074	1.779	1.663	1.270	1.498	1.432	1.381
99th	0.756	0.834	0.505	0.503	1.859	1.723	3.155	3.083	2.472	3.360	1.927	1.791	1.412	1.913	1.564	1.490
100th	1.266	1.456	2.740	1.084	2.543	2.313	4.036	4.351	3.427	4.399	2.443	2.277	2.221	2.843	3.045	2.016

A reference plane at the 97th percentile value of the surface data seems to be the most likely plane because it captures the SPT and provides an adequate estimate of the MTD. In the developing step, for it to be comparable with the sand patch, the considered rectangular area from the laser measurement had an area equal to that of the SPT. However, the whole scanned surface can be used to provide a better estimate of the MTD. When more data points are used, more efficient surface texture estimates can be obtained.

4.3.3. Repeatability of the Developed MTD Prototype versus the SPT

To assess the repeatability of the developed MTD prototype, five scans and MTD measurements were conducted on the same section under the same conditions. Similarly, the SPT was also performed five times on the same section by one operator. The MTD values calculated using the prototype and the SPT are provided in Table 4.4. To assess the variation, the standard deviation, the coefficient of variation, and the range of the five measurements were calculated. The results indicate that the proposed prototype provides better repeatability than the SPT, and hence a much higher reliability.

TABLE 4.4 Repeatability Analysis Results

No. of Tests	Prototype Results	SPT Results
1	0.6304	0.7483
2	0.6305	0.7000
3	0.6303	0.7724
4	0.6300	0.7322
5	0.6301	0.6232
Comparing Results		
Standard deviation	0.0002	0.0578
Coefficient of variation (%)	0.0329	8.0781
Range	0.0005	0.1492

Chapter 5. Pavement Friction and Texture

Correlation

5.1. Introduction

Understanding the texture-friction relationship is valuable for transportation agencies and engineers for proper pavement maintenance and better design of asphalt mixtures, especially when higher skid resistance is needed. A few studies have been conducted in this regard (Torbruegge and Wies, 2015; Gunaratne et al., 2000; Kane et al., 2013), but the effects of pavement texture on the friction produced at the pavement surface are still not fully understood. Hence, in this study, the researchers used field collected data of pavement friction and texture to develop friction-texture relationships appropriate for Texas conditions.

5.1.1. Measurement of Skid Resistance

There are three main skid resistance measuring principles: longitudinal friction coefficient (LFC), transverse, and stationary or slow-moving (Descornet et al., 2006; Do and Roe, 2008). The LFC measurement principle aims to measure friction when a vehicle is traveling forward in a straight line. When the brakes are applied, both the angular velocity of the wheel and the overall velocity of the vehicle decrease. When the braking force on the wheels is too strong, the wheels are “locked” and consequently slide over a surface. LFC measurement devices have slip ratios that simulate the wheel slipping process when a wheel slides over a surface. More specifically, the slip ratio compares the vehicle’s velocity to the angular velocity of the wheel. When the slip ratio is 0, the angular velocity of the wheel is the same as the velocity of the vehicle (i.e., no slip between wheel and surface). When the slip ratio is 1, there is no angular velocity in the wheel (i.e., wheel is fully locked and slides over the surface). LFC devices can have either a fixed or a variable slip ratio (Kane et al., 2013; Do and Roe, 2008).

The transverse measurement principle has been developed to test the pavement friction for vehicles in curves. The stationary or slow-moving measurement principle is used in compact devices usually found in the laboratory or still testing. One such device uses a pendulum arm; others, such as the Dynamic Friction Tester (DFT), use a rotating head. Both devices use rubber sliders that use the surface friction to slow down the pendulum or the rotating head (Descornet et al., 2006; Do and Roe, 2008; Andriejauskas et al., 2014).

Table 5.1 summarizes LFC measurement devices commonly used around the world. LFC devices can measure between 5 and 140 km/h (3 and 87 mph) and can come in the form of compact trailers or large-capacity trucks. LFC devices use a watering system, requiring vehicles to carry a water tank for testing purposes. Transverse friction measurement devices are usually larger, more expensive, and can take measurements for longer distances since greater water capacity increases

maximum measurement distance. While inexpensive and easy to use, stationary or slow-moving devices must be operated manually (Andriejauskas et al., 2014).

Table 5.1 Comparison of the LFC Measuring Devices (Descornet et al., 2006; Do and Roe, 2008; Andriejauskas et al., 2014)

Device Name	Theoretical water film thickness (WFT), Speed, Tire type, Measurement interval (Interval)	Assembly	Device Picture
ADHERA	TWFT: 1 mm Speed: 40–120 km/h Tire type: Smooth PIARC tire 165R15 Interval: 20 m Country/Countries of Use: France	Assembly: Trailer that can be hooked up to vehicle Commercially Available: No	
BV-11	TWFT: 1 mm Speed: 20–160 km/h [C] Tire type: Trelleborg tire T49 Interval: 20 m Country/Countries of Use: England, Sweden, and Finland	Assembly: Trailer that can be hooked up to vehicle Commercially available: Yes	
Grip-Tester	TWFT: 0.5 mm Speed: 5–100 km/h Tire type: Smooth ASTM tire, 254 mm diameter Interval: 10 or 20 m Country/Countries of Use: United States, United Kingdom, and others	Assembly: Trailer that can be hooked up to vehicle. Commercially available: Yes	
ROAR DK	WFT: 0.5 mm Speed: 60–80 km/h Tire type: ASTM 1551 Interval: 5m + Country/Countries of Use: Denmark	Assembly: Trailer that can be hooked up to a vehicle Commercially available: No	
ROAR NL	TWFT: 0.5 mm Speed: 50–70 km/h Tire type: ASTM 1551 Interval: 5–100 m Country/Countries of Use: Netherlands	Assembly: Three-axle tanker truck with two measuring systems mounted at the rear of the chassis. (Tank capacity is about 12,000 liters.) Commercially available: No	

Device Name	Theoretical water film thickness (WFT), Speed, Tire type, Measurement interval (Interval)	Assembly	Device Picture
RWS NL	TWFT: 0.5 mm Speed: 50 – 70 km/h Tire type: PIARC smooth 165 R15 Interval: 5 – 100 m Country/Countries of Use: Netherlands	Assembly: Trailer that can be hooked up to a vehicle. Commercially Available: No	
Skiddometer BV-8	TWFT: 0.5 mm Speed: 40–80 km/h TT: AIPCR ribbed, 165 R15, with four longitudinal grooves Interval: 30–50 m Country/Countries of Use: Sweden	Assembly: Trailer that can be hooked up to a vehicle Commercially available: Yes	
SRM	TWFT: 0.5 mm Speed: 40–80 km/h TT: AIPCR ribbed, 165 R15, with four longitudinal grooves Interval: 20 m Country/Countries of Use: Germany	Assembly: The test wheels are mounted on the back of a tanker vehicle at the approximate location of a vehicle tire paths. Commercially available: No	
TRT	WFT: 0.5 mm Speed: 40–140 km/h Tire type: Smooth ASTM Interval: Typically, 20 m Country/Countries of Use: Czech Republic	Assembly: The measuring equipment is under a specially equipped vehicle Commercially available: No	
SRT-3	WFT: 0.5 mm Speed: 30–90 km/h Tire type: Tire with thread (200kPa) Interval: 100 m Country/Countries of Use: Poland	Assembly: Trailer that can be hooked up to a vehicle Note: SRT-3 is more sensitive to micro-texture changes than to macro-texture changes. Commercially Available: No	

Device Name	Theoretical water film thickness (WFT), Speed, Tire type, Measurement interval (Interval)	Assembly	Device Picture
IMAG	WFT: 1.0 mm Speed: up to 140 km/h Tire type: PIARC smooth profile tire Interval: N/A Country/Countries of Use: France, Germany, and Poland	Assembly: Trailer that can be hooked up to a vehicle Commercially available: Yes	

Among the measurement devices presented in Table 5.1, the Grip-Tester was selected because it showed the most promise for measuring pavement friction due to its wider range of test speed, better repeatability and reproducibility (depending on the operating speed), greater efficiency in water usage, and commercial availability. The Grip-Tester is a friction-measuring trailer that uses a fixed slip wheel to simulate anti-lock braking on a wet road surface. This is achieved by the Grip-Tester having three wheels: two have patterned treads and are connected by a drive axle, while the third is a smooth tread tire. The drive axle, connecting the two drive wheels, has a 27-tooth sprocket; it is connected by a transmission chain to the measuring wheel that has a 32-tooth sprocket (Thomas, 2008). The difference in sprocket teeth creates a 15% continuous slippage on the measurement tire. To create wet road conditions, a watering system supplies a constant water thickness specified by the user to the measuring wheel.

The axle connecting the measuring wheel outputs the dynamic friction by using strain gages to measure the horizontal drag force and vertical load force. The information is used to estimate the Grip Number (GN), or coefficient of friction, in real-time (Thomas, 2008). As shown in Equation 5.1, the GN is the ratio between the fraction of tractive drag force (F_d) and the load force (Q).

$$GN = \frac{F_d}{Q} \tag{Equation 5.1}$$

The Grip-Tester (Figure 5.1(a)) requires a vehicle capable of towing the trailer as well as a water tank to supply water to the measuring wheel.

Along with the Grip-Tester, the DFT was used to measure the friction of the pavement at different speeds. This piece of equipment is specified under ASTM E1911. The DFT (shown in Figures 5.1(b) and 5.1(c)) consists of a rotating disk and three rubber pads attached to the bottom of the disk. The disk is pushed by an electric motor to rotate until it reaches the target speed set by an operator. At the same time, water is applied to the pavement surface. The disk drops and the rubber pads come into contact with the wet area. Each rubber pad is loaded vertically at 11.8 N (2.65 lb). The friction force developed between pads and the pavement slows down the disk. The DFT measures the friction coefficient continuously until the disk stops completely (Huang and Pan,

2006). As provided in Equation 5.2, the coefficient of friction (μ) is the ratio between the friction force or horizontal torque force (F) and the applied vertical load on the rubber sliders of the DFT (Austroads, 2005).

$$\mu = \frac{F}{Q}$$

Equation 5.2

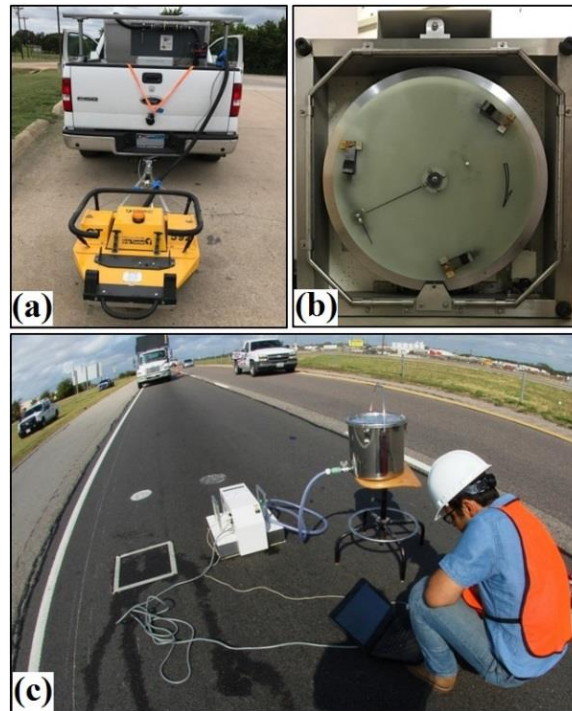


Figure 5.1 a) The Grip-Tester attached to a vehicle, b) bottom view of the DFT, and c) the DFT connected to a water tank and DCC measuring the friction at the lane center path

5.1.2. Measurement of Pavement Surface Texture

CTM is a common static method used to measure the macro-texture of the pavement surface. According to the ASTM E2157, the CTM (Figures 5.2(a) and 5.2(b)) consists of a laser-displacement sensor that rotates over a circle with a diameter of 284.5 mm (11.2 in.) and measures the profile of pavement surface texture. The profile includes 1,024 points scanned at an interval of 0.87 mm (0.034 in.). Using the instructions provided by ASTM E 1845, the measured profile then is sectioned into eight equal parts (Abbas et al., 2007; Mataei, 2016). Along with the CTM, the developed LLS prototype was also utilized to study the pavement texture.

The mean profile depth (MPD) is calculated from the height profile obtained from both the CTM and LLS following ASTM E1845. The first step is to quantify the inclination slope of the height profile such that a regression line is calculated and then subtracted from the height profile and so the initial profile will be converted to a zero-mean profile. As a second step (Figure 5.3), the height

profile is divided into two segments with the length of $\frac{L}{2}$ for which the maximum height is detected. By using Equation 5.3, MPD is calculated as the average of the two determined maximum heights.

$$MPD = \frac{\text{Max Height of 1st Segment} + \text{Max Height of 2nd Segment}}{2} \quad \text{Equation 5.3}$$

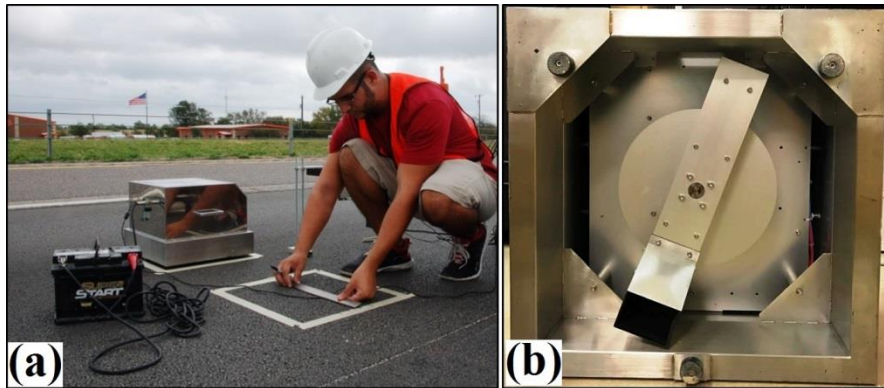


Figure 5.2 a) The CTM powered by a battery measuring the texture at the right wheel path, and b) bottom view of the CTM

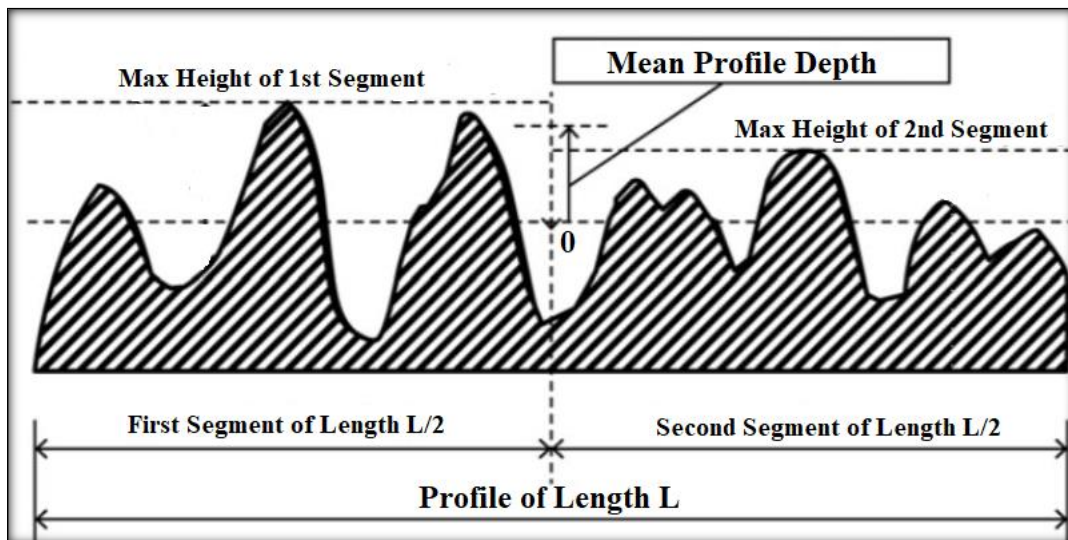


Figure 5.3 Graphical illustration of MPD calculation (ASTM E1845)

5.2. Data Collection

Three test sections, each more than five years old, were selected. Each section had established measurement data for the DFT, CTM, and LLS. The sections chosen provide a variety of mix designs, ensuring variation of surface texture for the test. The test sections are located in Bastrop, Bryan, and Fort Worth of Texas:

- Bastrop:
 - Mix design: Porous Friction Course (PFC)
 - Average annual daily traffic (AADT): 13,972
- Bryan:
 - Mix design: Dense-Graded Type C
 - AADT: 5,843
- Fort Worth:
 - Mix design: Dense-Graded Type D
 - AADT: 57,385

At each location, six samples were taken: three in the right wheel path and three in the center of the lane, with a 12.5 m (41 ft) distance between the locations (Figure 5.4). Within each location, one CTM and one DFT measurements were obtained. The CTM and DFT testing followed ASTM E2157 and ASTM E1911 procedures, which state the equipment should be placed in the same location.

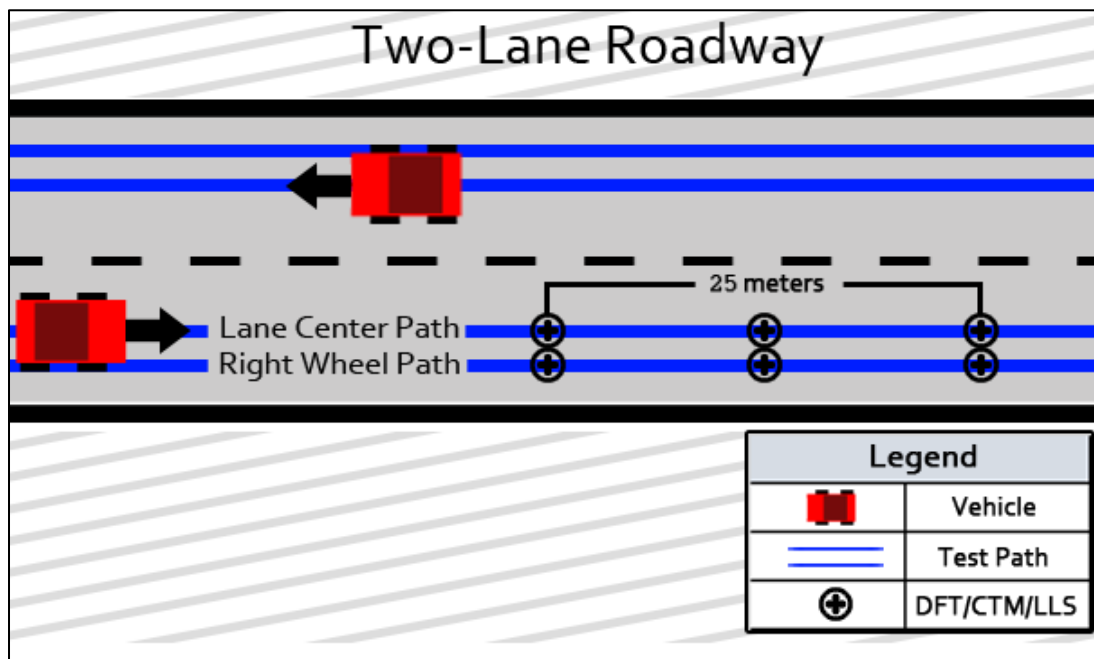


Figure 5.4 Illustration of test section and test location

To maintain consistency in the surface measurements, the LLS was placed in the same locations described for the CTM. Note, however, that these devices operate differently due to the mechanism of motion in each: the CTM measures in a circle and the LLS measures linearly. For the CTM, eight segments of 111.5 mm (4.39 in.) arcs are scanned by the laser, which results in a full circle. To ensure an equitable comparison with the CTM's measurements, the LLS was configured to

scan a 120 mm (4.72 in.) length at a linear speed of 8 mm/s (0.31 in./s) with a sampling frequency of 1 kHz. The area scanned by the LLS was the same as the segment of the CTM that was parallel to the direction of traffic.

For the Grip-Tester, the test consisted of two target speeds (50 km/h and 70 km/h) to evaluate the dependency of speed on friction. The speed needs to be maintained within 5% of the target speed. The 70 km/h (44 mph) target was selected to enable a direct comparison to the DFT equipment, which has a speed range of up to 80 km/h (50 mph).

5.3. Results and Discussions

5.3.1. Repeatability of Developed LLS Prototype

The LLS results were compared to those from the CTM to investigate the repeatability and reliability of the developed LLS. The MPD, as a surface characteristic, was calculated for all test locations. Then, single values of MPD for the right wheel path and the center were obtained by averaging the three respective samples. This was done for both LLS and CTM as graphed in Figure 5.5(a)—the -R and -C represent the right wheel path and center lane path, respectively. As this figure illustrates, the MPD values obtained by the LLS, denoted as *MPD-by-LLS*, are very close to the MPD values of CTM, denoted as *MPD-by-CTM*. There were no observable biases between the MPD values with which to draw a general conclusion.

Repeatability of the developed LLS prototype was evaluated by calculating the average and standard deviation of three MPD-by-LLS and MPD-by-CTM values obtained at each test section from their respective test paths. Then, the standard deviation of each group of data was compared. For example, the three MPD-by-LLS values for the pavement surface under the right wheel path at the Bryan test section were compared to each other with respect to their standard deviation. Due to the short distance between test locations, similar texture characteristics were expected at those locations. As Figure 5.5(b) indicates, the standard deviations of MPD-by-LLS data were significantly lower than MPD-by-CTM in three test sections (Bastrop-R, Bastrop-C, and Bryan-R). Comparable MPD values were observed at the rest of the sections. According to these results, one can suggest that the developed LLS prototype is capable of providing an accurate and precise measurement of the pavement surface texture.

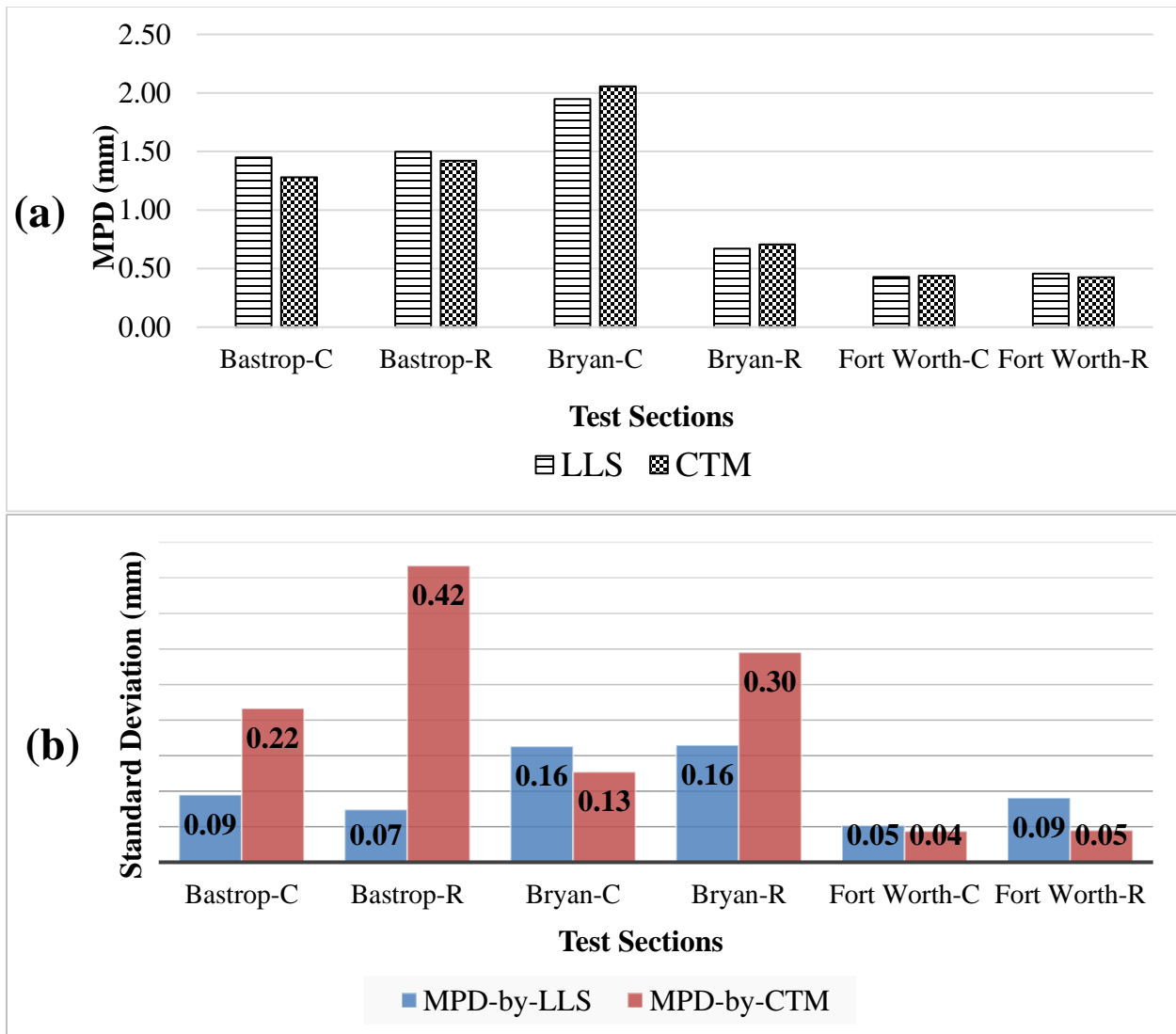


Figure 5.5 a) Comparison of mean MPD values obtained from developed LLS prototype and CTM, b) Standard deviation of MPD values measured by developed LLS prototype and CTM at six test sections

5.3.2. Grip-Tester Results

Figures 5.6(a) and 5.6(b) show the GN of all test locations plotted against the DFT values at two different speeds of 50 and 70 km/h (31 and 44 mph). As these figures illustrate, the GN values have a strong relationship with DFT values, with R^2 of 0.93 and 0.91 at the two different speeds. It can be concluded that this relationship is independent of the test speed.

These findings indicate that the Grip-Tester is a reliable alternative for the DFT and does not require traffic control, therefore, it is safer and more efficient. Besides, the Grip-Tester enables engineers to obtain continuous friction data over a long pavement section.

Based on the literature, no given speed has been specified by agencies to perform the test. Hence, understanding the effect of speed on GN would help researchers and practitioners interpret the friction results in different cases when the test speed is a variable. The results plotted in Figure 5.6(c) show that the GN decreased when the speed increased. This finding is reasonable but contrasts with the results of a study conducted at the University of Auckland by Wilson et al. in 2013, in which they stated that at speeds less than 75 km/h, the GN may not be affected by test speeds (27).

According to Figure 5.5(a), the MPD value of the section Bryan-R, which is about 0.70 mm (0.027 in.), is lower than Bastrop-R with MPD of 1.50 mm (0.06 in.). However, interestingly, in Figure 5.6(c), the GN at Bryan-R is higher than that of Bastrop-R. It should be mentioned that, in these test locations, the water film thickness of 0.5 mm (applied by Grip-Tester) can only cover a portion of surface texture depth. The surface pavement type of the Bastrop test section is PFC; therefore, the lack of small-size aggregates results in higher MPD values. On the other hand, the mix design of the Bryan test section is dense-graded type C, which contains all ranges of aggregate size and thus results in a lower MPD value but a greater tire-pavement contact area. In this case, it can be suggested that the adhesion factor is decisive in friction.

Although a PFC mix design increases the surface MPD (and thus causes more hysteresis), PFC's design also decreases the chance of the aggregates being fully exposed and coming into contact with the tire (thus decreasing the contact area and adhesion). A smooth surface is associated with more contact area and better adhesion, but it significantly decreases the MPD that results in lower hysteresis. Therefore, the balance between adhesion and hysteresis in the pavement surface should be optimized in order to maximize the surface friction and skid resistance. This is achievable by using an appropriate mix design providing both macro-texture and micro-texture.

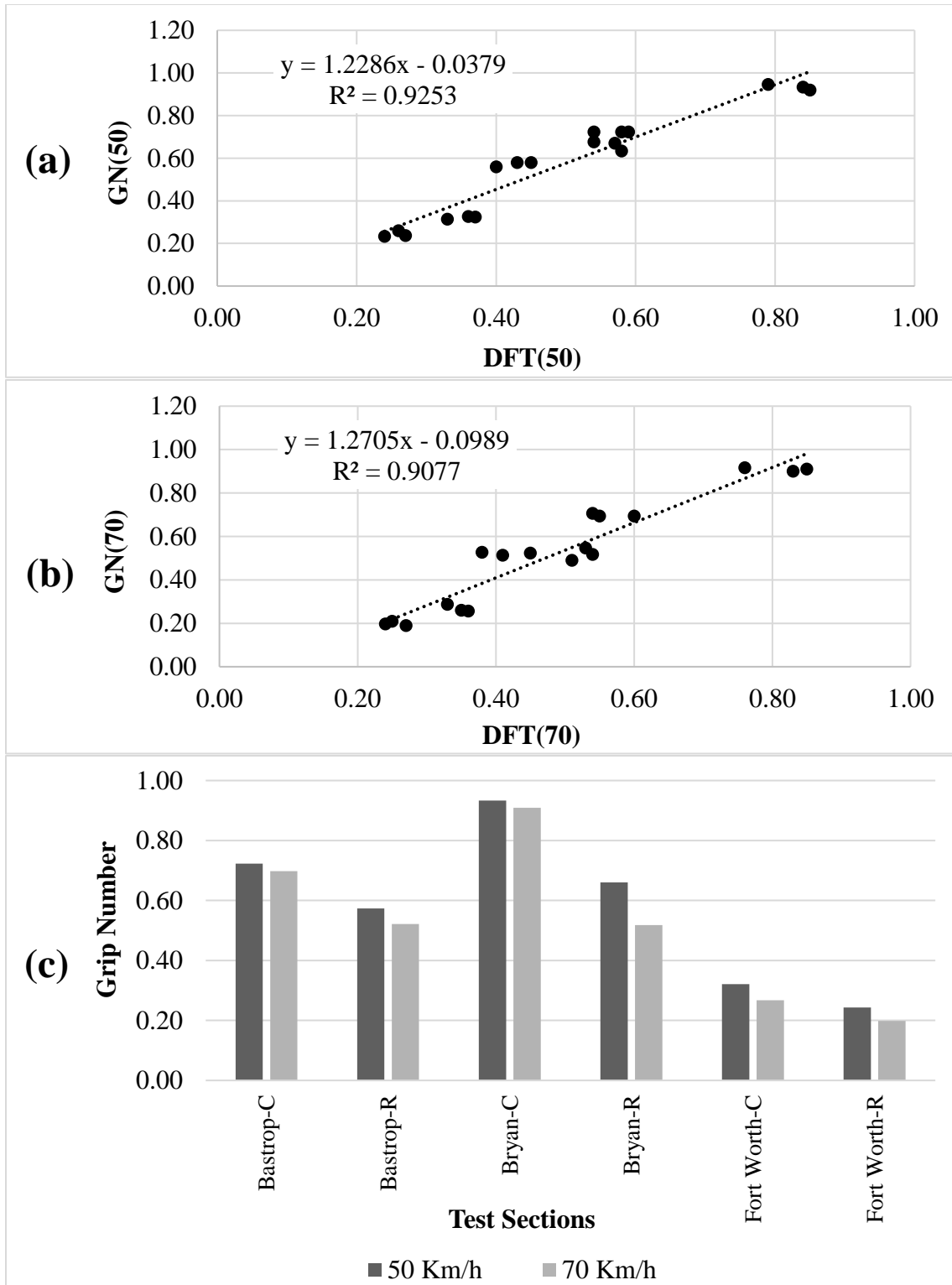


Figure 5.6 Correlation between GN and DFT values at two speeds of 50 and 70 km/h

The lowest friction was observed in the Fort Worth test sections where the MPD values were below 0.46 mm (0.018 in.). Considering the water film thickness of 0.5 mm (0.019 in.) applied by the

Grip-Tester for wetting purpose, it can be concluded that the surface texture was fully covered by water. In this case, the water trapped in the V- or U-shaped areas of the pavement surface bears the load from the tire and prevents the tire penetrating the spaces between the aggregates—thus reducing the contribution of the aggregate surface to the friction force by decreasing the tire-aggregate contact area (28).

5.3.3. Relationship between the Texture and Friction

The GN and DFT values both represent the friction properties of the pavement surface; however, the MPD values obtained by the LLS and CTM reflect the texture characteristics of the surface. To explore the relationship between the friction and texture, those two groups were plotted against each other in four different forms: GN vs. CTM, GN vs. LLS, DFT vs. CTM, and DFT vs. LLS.

Using statistical analysis, the correlation coefficient (R) was used to evaluate the relationships. The R ranges from -1 to +1, where negative and positive signs represent the negative or positive linear correlation respectively.

The statistical analysis shows that the relationship between the GN values and MPDs is strongly linear with high correlation coefficients (Figure 5.7). For the Grip-Tester performed at 50 km/h, the $R = 0.83$ was found for GN-CTM, and $R = 0.82$ for GN-LLS. In addition, higher correlation coefficients were observed at the speed of 70 km/h. The R values of 0.88 and 0.89 show a strong linear relationship between GN as a friction parameter, and MPDs of CTM and LLS, respectively.

From the results provided in Figure 5.7, the Grip-Tester data have a better relationship with texture compared to the DFT data in terms of the calculated R^2 values. Thus, it can be suggested that friction and skid resistance could be estimated by means of texture measurement data with high confidence.

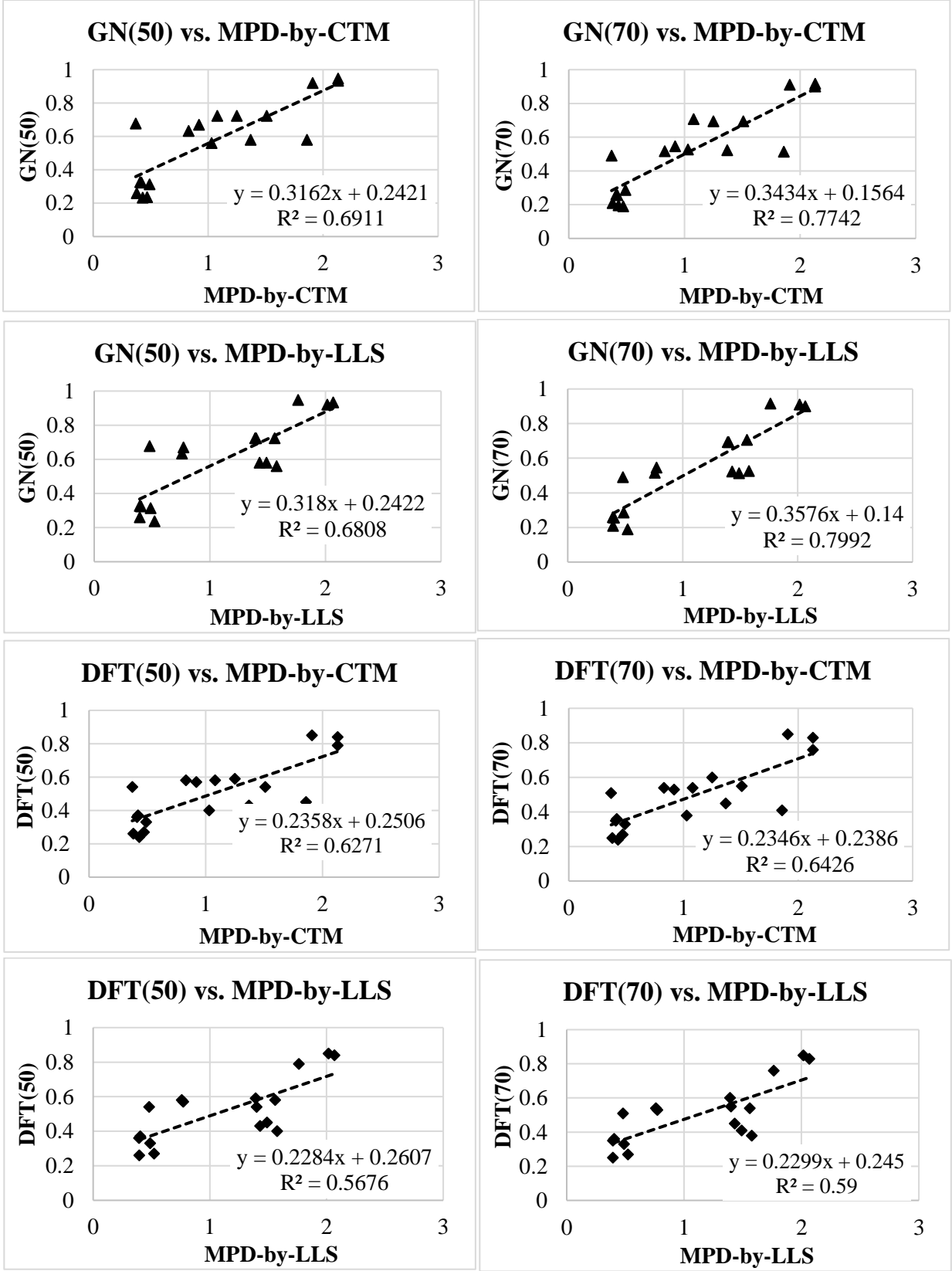


Figure 5.7 Plotted texture-friction data points including GN, DFT values, and MPD value

Chapter 6. Summary and Conclusions

In this research study a laser scanning prototype was developed that can capture both micro- and macro-texture. This prototype consists of a line laser scanner (LLS) mounted on a linear translation stage that can travel over a target and scan its surface. Several experiments, such as error and tilt correction, developing a LabVIEW program, and repeatability tests, were conducted by the research team to improve the developed LLS prototype's functionality. The application of the LLS prototype was evaluated in different areas of pavement texture characterization. From this research project, the following conclusions have been extracted and are presented in three parts addressing the various technical objectives set for this study.

6.1. Part 1: Aggregate Texture Measurement

The main scope of this project component was to investigate the variation of wavelength ranges of aggregates surface to find those that affect the aggregate texture characteristics. The developed LLS prototype was used to capture the texture data of aggregates, and numerical methods were utilized to analyze the captured data. Some key findings of this study are summarized as follows.

- To study the effect of orientation, an aggregate was scanned in different orientations of 0° , 90° , 180° , and 270° . Comparison of PSD plots of data obtained at different orientations showed that the effect of aggregate orientation at the time of scanning is negligible.
- The PSD values of aggregates obtained from the same source were found to behave similar in the first decade of micro-texture. It can be concluded that the aggregate PSD values in the first decade of micro-texture significantly depend on their mineralogical properties.
- Based on the analysis conducted using the paired t-test, the PSD values of two aggregate types vary in the first decade of micro-texture. However, the PSD values could not be differentiated within the first decade of macro-texture since the PSD lines were nested in that range.
- The spatial signals were processed by means of band-pass filters to separate the micro-texture components. The texture parameters of R_q and R_p calculated in different filtered profiles were consistent with the PSD values within the wavelength range of 0.05 to 0.25 mm. It could be concluded that the wavelengths within this range make the greatest contribution to the texture friction and this range of wavelength can be used to differentiate aggregate particles.
- The results of PSD, R_p , and R_q were consistent with the Surface Aggregate Classification provided by TxDOT in which the aggregate A exhibited higher frictional properties compared to the aggregate B.

- The developed LLS prototype is capable of differentiating aggregates at the micro-texture levels, and it is recommended that micro-texture should be included into the SAC classification to address the potential of the aggregate to provide surface friction.

6.2. Part 2: An Automatic Method for Measuring Pavement Macro-Texture

This study proposes an algorithm to calculate the MTD based on 3D pavement data. The LLS prototype was used to scan and collect pavement data. The repeatability and variability of the developed MTD algorithm were compared with those of the SPT.

- The experimental results proved the high repeatability of the proposed prototype.
- Additional advantages to this prototype are high testing speed and larger area coverage. In contrast, the SPT is a tedious test and is limited to few test sections. Using this prototype, larger representative sections along both the width and the length of the road can be assessed.
- This approach both increases the efficiency of assessing the pavement texture and provides a better understanding of the pavement surface texture.
- It is recommended that the developed prototype should be considered as an efficient alternative to the SPT.

6.3. Part 3: Correlation between Pavement Texture and Friction

During this study, the LLS prototype was used to measure the texture data along with the CTM. The MPD was adopted as a pavement texture indicator. DFT and Grip-Tester were employed for friction measurement. The efficiency and repeatability of the developed LLS were explored through comparison to the CTM results.

- The results of the repeatability analysis and standard deviation showed the reliability of the developed LLS prototype for pavement texture measurement. In all the test sections, the MPD calculated from the LLS data was similar to that calculated from the CTM data. Therefore, it is recommended that the developed LLS prototype should be considered as an efficient alternative to the CTM device, especially when three-dimensional texture data are needed.
- Regardless of the test speed and pavement type, the friction number obtained by the Grip-Tester showed a strong linear correlation with DFT measurements. Due to the reliable results of the Grip-Tester, its wider range of friction measurement, and the lack of need to control traffic, this device is recommended for use by state DOTs for friction measurement.
- The quality of the friction data obtained by a Grip-Tester seemed to be somewhat sensitive to the test speed, because the GN decreased slightly when the test speed increased from 50

km/h to 70 km/h (31 to 44 mph). This finding implies that keeping the test speed fixed at different test sections is important to achieving comparable results.

- The findings of the statistical analysis pointed to a strong positive linear correlation between texture and friction in pavements. The highest linear correlation coefficients (R) were observed between the GNs obtained at 70km/h (44 mph) and texture data obtained using either the LLS or the CTM.

References

- Ahammed, M.A., and S.L., Tighe. Pavement Surface Mixture, Texture and Skid Resistance: A Factorial Analysis. Conference of Airfield and Highway Pavements, ASCE, 2008.
- Alazartech, Variable Frequency ADC Clock. <http://www.alazartech.com/Technology/Variable-Frequency-ADC-Clock>, Accessed January 1, 2017.
- Andriejauskas, T., V. Vorobjovas, and V. Mielonas. Evaluation of skid resistance characteristics and measurement methods”, 9th International Conference of Environmental Engineering, Vilnius, Lithuania, 2014.
- Anochie-Boateng, J. K., Komba, J. J. and Mvelase, G. M. Three-dimensional laser scanning technique to quantify aggregate and ballast shape properties. *Journal of Construction and Building Materials*, Vol. 43, 2013, pp. 389–398.
- Asi, I.M. Evaluating skid resistance of different asphalt concrete mixes. *Journal of Building and Environment*. Vol. 42, 2007, pp. 325–329.
- Austrroads, 2005: Guide to the Management of Road Surface Skid Resistance. Sydney, Australia: Austrroads, 2005.
- Baraniuk, R. *Signals and Systems*. Rice University, Houston TX, 2009.
- Behrens, M.W. (1999), “Wet Weather Accident Reduction Program (WWARP)”, Highway Design Division Operations and Procedures Manual, Texas Department of Transportation, Austin, Texas.
- Cafiso, S. and S. Taormina. Texture analysis of aggregates for wearing courses in asphalt pavements. *International Journal of Pavement Engineering*, Vol. 8, 2007, pp. 45-54.
- Chamberlin, W. P., and Amsler, D. E. Measuring Surface Texture by the Sand-Patch Method. *American Society for Testing and Materials*, 1982.
- Characterization of Pavement Texture by Use of Surface Profiles. ISO 13473-1, 1997, International Organization for Standardization.
- Characterization of Portland Cement Concrete Pavements. *Journal of Computer-Aided Civil and Infrastructure Engineering*, Vol. 22, 2007, pp: 197–209.
- Descornet, G., B. Schmidt, M. Boulet, M. Gothie, M.T. Do, J. Fafie, M. Alonso, P. Roe, R. Forest, and H. Viner. HERMES Project: Harmonization of European Routine and research Measuring Equipment for Skid Resistance. FEHRL report, 2006.
- Do, M.T., and P. Roe, Report on state-of-the-art of test methods. TYROSAFE project deliverable D04, 2008.
- Flintsch, W. G., León, E., McGhee, K., and Al-Qadi, I. Pavement Surface Macrotecture Measurement and Application. Virginia Tech Transportation Institute, 2003.
- Freitas, E., Pereira, P., Antunes, M. L., and Domingos, P. Analysis of Test Methods for Texture Depth Evaluation Applied in Portugal, *C-TAC – Comunicações a Conferências Nacionais*, 2008. <http://hdl.handle.net/1822/14550>.

- Gunaratne, M., N. Bandara, J. Medzorian, M. Chawla, and P. Ulrich. Correlation of Tire Wear and Friction to Texture of Concrete Pavements. *Journal of Materials in Civil Engineering*, Vol. 12, 2000, pp. 46-54.
- Halil S., Nicholas, F., and Patrick, L. *Validation of ODOT's Laser Macrottexture System*. Publication FHWA/OH-2008/12, Ohio Department of Transportation, 2008.
- Hall, J.W., K.L. Smith, L. Titus-Glover, L.D. Evans, J.C. Wambold, and T.J. Yager. *NCHRP Project 01-43: Guide for Pavement Friction*. Transportation Research Board, Washington, D. C., 2009.
- Hanson, D.I., Prowell, B.D. Evaluation of Circular Texture Meter for Measuring Surface Texture of Pavements. NCAT Report 04-05, National Center for Asphalt Technology, Auburn, AL, 2004.
- Hao, X., Sha, A., Sun, Z., Li, W., and Zhao, H. Evaluation and Comparison of Real-Time Laser and Electric Sand-Patch Pavement Texture-Depth Measurement Methods. *Journal of Transportation Engineering*, 2016.
- Henry, J.J. NCHRP Synthesis of Highway Practice 291: Evaluation of Pavement Friction Characteristics. Transportation Research Board, National Research Council, 2000.
- Hoerner, T.E., and K. D. Smith. High performance concrete pavement: Pavement texturing and tire-pavement noise. Publication FHWA-DTFH61-01-P-00290. FHWA, U.S. Department of Transportation, 2002.
- Hogervorst, D. Some Properties of Crushed Stone for Road Surfaces. Bulletin of the International Association of Engineering Geology—Bulletin de l'Association Internationale de Géologie de l'Ingénieur, 10, 59-64, 1974.
- Hsu, H.P. Schaum's Outlines of Theory and Problems of Signals and Systems. McGraw-Hill Companies, USA, 1995.
- Hu, L., D. Yun, Z. Liu, S. Du, Z. Zhang, and Y. Bao. Effect of three-dimensional macrottexture characteristics on dynamic frictional coefficient of asphalt pavement surface. *Journal of Construction and Building Materials*, Vol. 126, 2016, pp. 720–729.
- Huang, Y. H. Pavement Analysis and Design. 2nd Edition. New Jersey: Pearson/Prentice Hall, 2003.
- Kane, M., I. Artamendi, and T. Scarpas. Long-term skid resistance of asphalt surfacings: correlation between Wehner–Schulze friction values and the mineralogical composition of the aggregates. *Wear*, Vol. 303, 2013, pp. 235–243.
- Karrenberg, U. *Signals, Processes, and Systems*. Third edition, Springer Heidelberg Dordrecht London New York, 2013.
- Kogbara, B.R., E.A. Masad, E. Kassem, A.T. Scarpas, and K. Anupam. A state-of-the-art review of parameters influencing measurement and modeling of skid resistance of asphalt pavements. *Journal of Construction and Building Materials*, Vol. 114, 2016, pp. 602–617.
- Laurent, J., Fox-Ivey, R., Dominquez, F.S., and Garcia, J.A.R. (2014), 'Use of 3D Scanning Technology for Automated Inspection Tunnels,' Proceeding of the World Tunnel Congress 2014, Foz Do Iguaçu, Brazil.

- Mari, J.L, F. Glangeaud, and F. Coppens. *Signal Processing for Geologists and Geophysicists*. Editions OPHRYS, 1999.
- Masad, E. *The development of a computer controlled ImageAnalysis System for measuring aggregate shape properties*. Final report, NCHRP-IDEA Project 77. Transportation Research Board of the National Academies, Washington, D.C., 2003.
- Masad, E., A. Rezaei, A. Chowdhury, and P. Harris. *Predicting Asphalt Mixture Skid Resistance Based on Aggregate Characteristics*. FHWA/TX-09/0-5627-1, Texas A&M University, 2009.
- Mataei, B., H. Zakeri, M. Zahedi, and F. M. Nejad. Pavement Friction and Skid Resistance Measurement Methods: A literature Review. *Journal of Civil Engineering*, Vol. 6, 2016, pp.537-565.
- MathWorks Inc. *Matlab-Getting Started Guide*. Natick, MA, 2016.
- Meegoda J. N., Hettiarachchi, C.H., Rowe, G.M., Bandara, N., and Sharrock, M.J. *Correlation of Surface Texture, Segregation, and Measurement of Air Voids*. Publication FHWA-NJ-2002-026, FHWA, 2002.
- Olshausen, B.A. *Aliasing, – Sensory Processes*. PSC 129, October 10, 2000, <http://redwood.berkeley.edu/bruno/npb261/aliasing.pdf>, Accessed January 1, 2017.
- Oppenheim, A., A.S. Willsky, and S.H. Nawab. *Signals & Systems*. Second edition, Pearson Education, 1998.
- Oppenheim, A.V., R. W. Schafer, and J.R. Buck. *Discrete-Time Signal Processing*. Third Edition, Prentice-Hall Signal Processing Series, Pearson Education, 2009.
- Orfanidis, S.J. *Introduction to Signal Processing*. US ed Edition, Prentice Hall, 1995.
- Osgood, B. *Lecture Notes for the Fourier Transform and its applications*. Electrical Engineering Department Stanford University, 2007. <https://see.stanford.edu/materials/lsoftae261/book-fall-07.pdf>, Accessed January 1, 2017.
- Pidwerbesky, B., Waters, J., Gransberg, D., Stemprok, R. Road Surface Texture Measurement Using Digital Image Processing and Information Theory. Land Transport New Zealand Research Report 290, 2006.
- Poon, C.Y., and B. Bhushan. Comparison of surface roughness measurements by stylus profiler, AFM and non-contact optical profiler. *Wear*, 1995, pp.76-88.
- Prowell, B.D., Hanson, D.I. Evaluation of circular texture meter for measuring surface texture of pavements. Transportation Research Record 1929, 2005, pp. 88–96.
- Putman, J.A. *Signal Processing Techniques*. 2007. https://www.eeginfo.com/research/researchpapers/Signal_Processing.pdf, Accessed on Dec 21, 2016.
- Roadway Departure Safety - Safety | Federal Highway Administration".Safety.fhwa.dot.gov. N.p., 2017. https://safety.fhwa.dot.gov/roadway_dept/, Accessed on February 20, 2017.
- Rose, J. G. *Surface Texture versus Skidding: Measurements, Frictional Aspects, and Safety Features of Tire-Pavement Interactions*. ASTM Special Technical Publication 583, 1975.

- Sandberg, U. Influence of Road Surface Texture on Traffic Characteristics Related to Environment, Economy, and Safety: A State-of-Art-Study Regarding Measures and measuring Methods. *VTI notat53A-1997*, 1998, Swedish National Road Association, Linköping, Sweden.
- Sengoz, B., Topal, A., and Tanyel, S. Comparison of Pavement Surface Texture Determination by Sand Patch Test and 3D Laser Scanning. *Journal of Periodica Polytechnica Civil Engineering*, 2012. Vol. 45, pp. 73-78.
- Serigos, A.P., A.F. Smit, and J.A. Prozzi. Incorporating Surface Microtexture in the Prediction of Skid Resistance of Flexible Pavements. *Journal of the Transportation Research Board*, Washington, D.C., 2014, pp. 105–113.
- Sherrington, I., and E.H. Smith. Modern Measurement Techniques in Surface Metrology: Part II; Optical Instruments. *Wear*, 1988, pp.289-308.
- Slimane, A.B., M. Khoudeir, J. Brochard, and M.T. Do. (2008), “Characterization of road microtexture by means of image analysis”, *Wear*, Vol. 264, 2008, pp. 464-468.
- Standard Practice for Calculating Pavement Macrottexture Mean Profile Depth*. ASTM E1845 – 2015, Philadelphia, Pennsylvania, American Society for Testing and Materials.
- Standard Practice for Calculating Pavement Macrottexture Mean Profile Depth*. ASTM E1845 – 2015, Philadelphia, Pennsylvania, American Society for Testing and Materials.
- Standard Terminology Relating to Vehicle-Pavement Systems*. ASTM E867 – 2012, Philadelphia, Pennsylvania, American Society for Testing and Materials.
- Stefan Torbruegge, S., and B. Wies. Characterization of pavement texture by means of height difference correlation and relation to wet skid resistance. *Journal of Traffic and Transportation Engineering*, Vol. 2, 2015, pp. 59-67.
- Texas Department of Transportation (TxDOT), (2016), “Bituminous Rated Source Quality Catalog (BRSQC)”, Construction Division, Materials & Pavements (CST-M&P). <ftp://ftp.dot.state.tx.us/pub/txdot-info/cmd/mpl/brsqc.pdf>,
- Thomas, L. Grip-Tester MK2 D-type Maintenance Manual. Issue 4, Findlay, Irvine Limited, Scotland, 2008.
- Thomas, L. Grip-Tester MK2 D-type Maintenance Manual. Issue 4, Findlay, Irvine Limited, Scotland, 2008.
- Vorburger, T.V., and J. Raja. *Surface Finish Metrology Tutorial*. NISTIR 89-4088, 1990.
- Wang, D., P. Liu, H. Wang, A. Ueckermann, and M. Oeser. Modeling and testing of road surface aggregate wearing behavior. *Journal of Construction and Building Materials*, Vol. 131, 2017, pp. 129–137.
- Wang, H., and Z. Wang. Evaluation of pavement surface friction subject to various pavement preservation treatments. *Journal of Construction and Building Materials*. Vol. 48, 2013, pp. 194–202.
- Wang, L., X. Wang, L. Mohammad, and C. Abadie. Unified Method to Quantify Aggregate Shape Angularity and Texture Using Fourier Analysis. *Journal of Materials in Civil Engineering*, Vol. 17 (5), 2005, pp. 498-504.

- Wang, W., Yan, X., Huang, H., Chu, X., and Abdel, N. Design and Verification of a Laser based Device for Pavement Macrotecture Measurement. *Journal of Transportation Part C*, 2011. 19: 682-694.
- Yaacob, H., Hassan, N. A., and Hainin, M. R. Comparison of Sand Patch Test and Multi Laser Profiler in Pavement Surface Measurement. *Jurnal Teknologi*, 2014: 70(4), 103-106.
- Yoo, Y. *Tutorial on Fourier Theory*. 2001.
http://www.cs.otago.ac.nz/cosc453/student_tutorials/fourier_analysis.pdf, Accessed on January 18, 2017.
- Zhang, X., T. Liu, C. Liu, and Z. Chen. Research on skid resistance of asphalt pavement based on three-dimensional laser-scanning technology and pressure-sensitive film. *Journal of Construction and Building Materials*, Vol. 69, 2014, pp. 49–59.

Appendix A: Enhancing Chip Seal Design Using the LLS Prototype

INTRODUCTION

Chip seal, as the most widespread pavement preventive treatment, is regularly applied on existing pavements that are still in good structural condition to increase the pavement serviceability. Chip seal consists of spraying a layer of asphalt binder on the existing pavement surface, spreading a layer of one-aggregate-thick chips, and compacting the whole structure. The asphalt binder is sprayed to seal any cracks in the existing pavement, waterproof the surface, hold the aggregates in place, and essentially bind the new system to the existing one (Islam, 2007). Almost immediately after spraying the binder, the aggregates are spread and compacted to enrich the surface macro-texture and provide adequate skid resistance (Elmore et al., 1995; Patrick, 2008; Epps et al, 1981). The effectiveness of this dual system is directly related to the adequate estimation of both the binder application rate (BAR) and the aggregate application rate (AAR). The amount of binder needed is directly proportional to the average least dimension (ALD) of aggregates, volume of voids in the covering aggregates and the texture of the existing pavement surface. Inadequately assessing the ALD and the voids in the system leads to an inappropriate amount of binder. A poorly designed chip seal compromises the safety of the users due to distresses such as raveling and bleeding (Senadheera et al., 2000).

This research consists of two phases: Phase I involves reviewing the existing methods highway agencies use to measure the ALD of aggregates. In this phase a methodology for measuring ALD by using the LLS prototype is proposed. Phase II first discusses how distinctive chip seal design methods account for the voids in the existing surface texture, then proposes a test procedure to objectively measure the voids in the existing surface texture using the LLS prototype.

Phase I

EXISTING ALD MEASUREMENT METHODS

The ALD refers to the overall average of the least dimension (LD) of the aggregate particles spread on the binder layer in chip seals. The ALD of aggregate is essential to calculate the application rate of asphalt binder. Under traffic movement, aggregate particles are rotated until they sit on their flattest sides; hence, the LD value of aggregates is critical to assure proper coverage of the asphalt binder and prevent bleeding. The ALD of aggregates is mainly calculated as the average of the least dimension value of the representative particles. Test methods to determine the ALD vary among highway agencies. Mulry et al. (2015) grouped the existing ALD computation methods as follows:

1. A Vernier caliper, a dial gauge, or a slotted gauge

These devices directly measure the LD of aggregate samples. Although these apparatuses are simple and low cost, their measurement processes are slow and involve human errors.

2. ALD machine developed in South Africa

The ALD machine (Figure A.1(a)) is used to calculate the LD of aggregate particles manually. The advantage of this device compared to previous devices is that the LD values of samples are stored in a computer. However, similar to the previous devices, the ALD machine measures the LD of aggregate particles one by one, which is time-consuming.

3. Jackson Nomograph and Equation

Jackson (1963) developed a nomograph (Figure A.1(b)) based on nominal size and flakiness index of aggregate particles to calculate the ALD. He stated that the nominal size of aggregate particles merely is not sufficient to calculate the ALD because flaky particles and cubical particles might have the same nominal size, but their LD values are different. To calculate ALD using the nomograph, first, the median size of particles and flakiness index are obtained through laboratory tests. Then, the values of these parameters are marked in the nomograph. The ALD is obtained by drawing a line between these two values. Later, the following equation was formulated by Jackson in 1963 based on the ALD nomograph. Two factors—median particle size and flakiness index—are required to determine the ALD.

$$ALD = \frac{M}{1.139285 + 0.011506 FI} \quad \text{Equation A.1}$$

where,

M = median particle size from sieve analysis; and

FI = Flakiness Index (%).

4. Dumas Method

In 2004, Dumas criticized the model developed by Jackson (ALD nomograph and equation) claiming that the median size cannot fully represent the particle size distribution and instead proposed using five sieves corresponding to 10, 25, 50, 75, and 90% passing of particles rather than using only the median size. In this method, the ALD is measured by performing a sieve analysis and complex calculations (Murly et al., 2015; Dumas, 2001).

The existing test methods used to measure the ALD are subjective and laborious. A rational method is required to measure the LD values of aggregate particles more quickly and accurately. In recent years, the use of image and laser scanning technique in engineering surveys is gaining an increasing interest due to the advantages of being non-contact, rapid, and highly accurate. Several researchers have used image-based techniques to improve methods for measuring aggregate properties. In an effort, Masad developed the Aggregate Imaging System (AIMS), which is capable

of analyzing the shape properties of coarse and fine aggregates (Masad, 2003). The drawback of using the AIMS is that it is only capable of taking 2D images. Therefore, there is some uncertainty in measuring the LD values of aggregates. For more extensive measurements of the aggregates, it is preferable to obtain a 3D data of the particles. Anochie-Boateng et al. have conducted several studies on the use of 3D laser scanner technologies to measure aggregate properties such as shape, surface area, and angularity. The results of those studies showed that the laser could provide reliable and precise measurements. However, the 3D laser scanner developed by Anochie-Boateng et al. has a chamber with the capacity of only one aggregate for scanning and measurement.

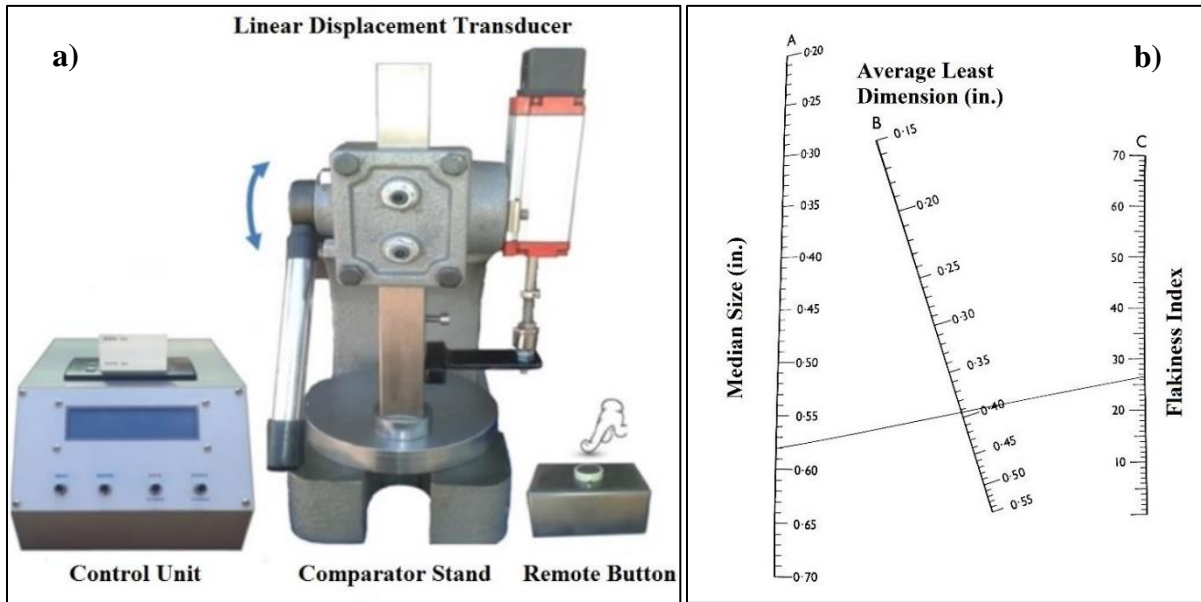


Figure A.1 a) ALD machine developed in South Africa, b) Jackson ALD nomograph

PROJECT APPROACH

The goal of this study is to evaluate the feasibility of using the LLS prototype to measure the LD value of particles. The LLS prototype is capable of scanning 100 particles simultaneously at high speed, with a resolution of 0.025 mm resulting in 3D data from the scan. Therefore, the limitations of the 2D image-based techniques can be overcome by using the LLS prototype and a more rigorous measurement of aggregates can be achieved. In this study, the repeatability, reliability, and performance of the LLS prototype are evaluated by comparing its results to those of a caliper.

RESEARCH METHODOLOGY

Aggregate Selection and Preparation

Table A.1 shows the master gradation ranges of the most common chip seal aggregates used in Texas. According to Table A.1, aggregate retained on top of the sieve size 12.5 mm to aggregate retained on top of sieve size 2 mm might be included in chip seal applications given the selected gradation. A sample of particles retained on top of sieves of sizes 12.5, 9.5, 6.3, 4.75 and 2 mm

(0.49, 0.37, 0.25, 0.19, 0.08 in.) was selected to evaluate the capability of the new system in measuring variable-sized particles. Aggregates used for this study were provided by Texas Department of Transportation (TxDOT) Construction Division in Austin, TX. The aggregates were first washed to remove any dust. Then, the aggregate particles were oven-heated to 160°C for 24 hours followed by 4 hours of in room temperature to reach air-dry condition.

MEASUREMENT PROCESS AND RESULTS

Within the scope of this study, the reliability of the developed prototype was tested in three steps: (i) testing the repeatability, (ii) evaluating the effect of particle’s orientation angle on measurements, and (iii) measuring the LD values of particles of variable sizes all together. The results of the developed LLS prototype were compared to that of a digital caliper.

Repeatability of the Developed LLS Prototype

One aggregate particle was put in the scanning area of the prototype and scanned ten times in the same conditions to check the repeatability of the scanning system. Scanned data collected by the developed LLS prototype were stored on the computer for processing using MATLAB software. There are some points with very high or low values around the edge of the particle where the laser cannot see the reflection of light or due to the particle’s shadow (where the light might reflect several times and cause noise in data processing). These invalid data need to be dealt with before calculating the LD value of particle. The scanned data were first converted to a binary image which has a black background and a white object. This is followed by creating a boundary around the white object to separate the data associated to the aggregate from the background. It is to be noted that the LD value of the aggregate when sitting on its flattest side is a key factor in chip seal design. Therefore, in all tests, aggregate particles were arranged manually with their flattest side down. Accordingly, the elevation of the highest point within the boundary provides the LD value of that particle relative to the reference line.

Table A.1 Common Aggregate Gradations for Texas Chip Seal (TxDOT, 1995)

Size (mm)	Grade 3	Grade 4	Grade 5
19	0	-	-
16	0 – 2	0	-
12.5	20 – 40	0 – 2	0
9.5	80 – 100	20 – 35	0 – 5
6.3	95 – 100	-	-
4.75	-	95 – 100	40 – 85
2	99 – 100	99 – 100	98 – 100
0.85	-	-	99 – 100

Note: Values are percent retained on sizes shown.

The LD value of the selected particle was also measured for ten times using a digital caliper with a specified accuracy of 0.01 mm, and then the measurements results were compared to the LLS results. Table A.2 provides a side-by-side comparison of two measurements. As can be seen in the table, the mean value and the standard deviation of the ten measurements captured by the developed LLS prototype is 6.931 mm and 0.009 mm (0.273 and 0.0004 in.) respectively. The mean value and the standard deviation of the ten measurements captured by the caliper are 7.01 mm and 0.065 mm (0.276 and 0.0026 in.) respectively. This table also shows the maximum, minimum, and the range of measurements captured by two devices. These results show that the measurements by the LLS have smaller standard deviation and range compared to the caliper. One can suggest that the developed LLS prototype provides better repeatability.

Effect of Aggregate Orientations on ALD Measurement

An aggregate particle tends to lie randomly on the asphalt binder layer; however, its LD value does not change by the rotation. To evaluate the effect of orientations on the accuracy of the developed LLS prototype, an aggregate particle was rotated in four different directions ranging from 0° to 270° with an interval of 90° with respect to the laser line and then scanned. The result and the figure associated with each direction are provided in Figure A.2. The black areas in the figures represent the parts very close to the edge of the aggregate where the laser was not able to see the light projection and missed the data. Since this area is related to the edge of the aggregate, the missing data did not impact the LD value measurement. The variability between measurements is calculated by the standard deviation which is equal to 0.011 mm (0.0004 in.) shows that the effect of the orientation is negligible.

Table A.2 Side-by-Side Comparison of the Measurement Results of LLS and Digital Caliper

Descriptive Statistic	LLS	Caliper
Mean	6.931 mm	7.01 mm
Standard Deviation	0.009 mm	0.065 mm
Minimum	6.917 mm	6.88 mm
Maximum	6.941 mm	7.09 mm
Range	0.024 mm	0.21 mm

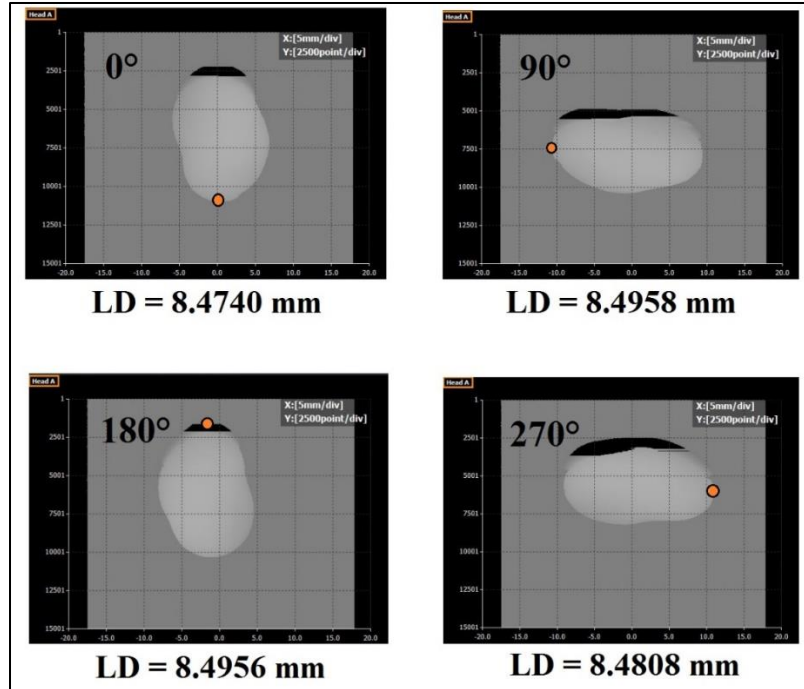


Figure A.2 LD values of a particle at different orientations

Measurement of Particles with Variable Sizes

Devices like calipers measure the LD values of representative particles separately. In addition, timely sieve analysis tests are required in approaches like Jackson and Dumas's methods to measure the LD values of a sample of particles altogether. To evaluate the speed of the developed LLS prototype and its feasibility to measure the LD values of numerous particles, 100 variable-sized particles (in the range of 2 to 12.5 mm) were arranged manually in the scanning area. The developed LLS prototype has a scanning area of 160×600 mm (6.3×23.62 in.) within which particles must be spread. As shown in Figure A.3(a), the particles should stand within that area to reduce the error in analysis. Particles were scanned, and the collected data were stored in the computer. As explained in the previous step, after converting the data to a binary image, aggregate particles were discriminated from the background by finding a boundary around each particle and labeling them. The height points within each boundary were exported to a separate Excel sheet to determine the LD value of the corresponding particle. To evaluate the accuracy of the process, as shown in Figure A.3(b), each particle was also calipered several times to find the LD value of that particle and compared to the developed LLS prototype measurements.



Figure A.3 a) 100 particles spread in the developed LLS prototype scanning area, and b) making measurement using a caliper

Figure A.4 shows the plot of measurements captured by the developed LLS prototype versus those of the caliper. The best-fit line to the plotted data with correlation coefficient, R , of 0.99 (the square root of R^2) was calculated which presents a strong relationship between developed LLS prototype measurements and the caliper outcomes. As a result, the developed LLS prototype is capable of calculating the LD values of variable-sized particles simultaneously. While the measurement of 100 particles by the caliper took about 4 hours, the measurement processes by LLS prototype (including capturing data, data processing and attaining results) were done in less than 10 minutes. Accordingly, the developed LLS prototype saves time and cost. In addition, more particle samples can be measured to obtain a precise ALD estimation.

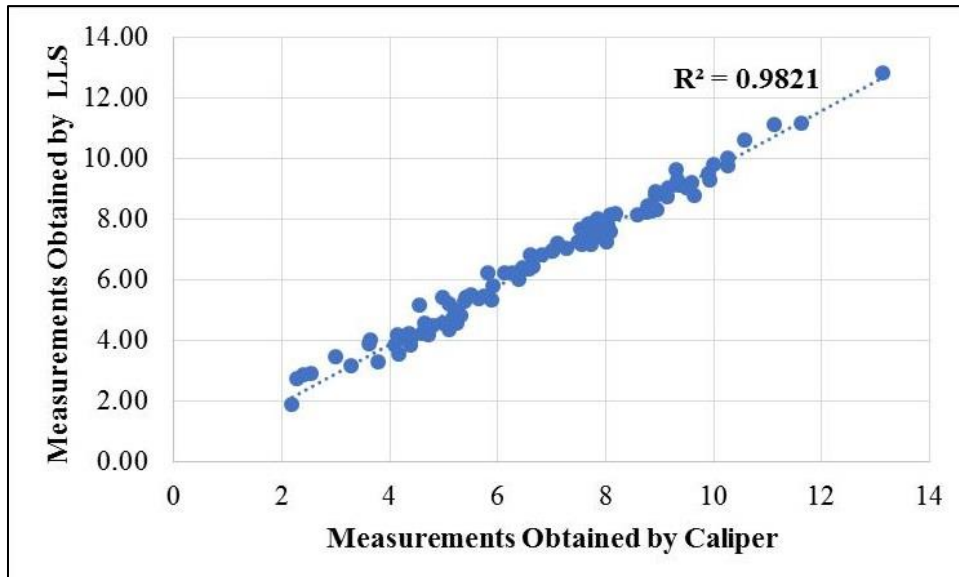


Figure A.4 Plot of LD values of 100 particles captured by the developed LLS prototype and digital caliper

Phase II

CHIP SEAL DESIGN METHODS

Hanson Method, New Zealand 1935

According to Hanson, the BAR is determined such that not all the voids in the aggregates are filled with binder, but a sufficient portion is in place to hold the one-stone-thick layer of aggregates in place, preventing bleeding and raveling. Based on Hanson's experience, the aggregates will be held in position if the binder occupies 50 to 70% of the voids. However, the volume of voids in the aggregates decreases with time. As shown in Figure A.5, the aggregates are subject to short-term compaction by using rollers that reduce the volume of voids from 50% to 30%. This is followed by a long-term continuous compaction by means of trafficking where the voids ultimately occupy 20% of the compacted depth.

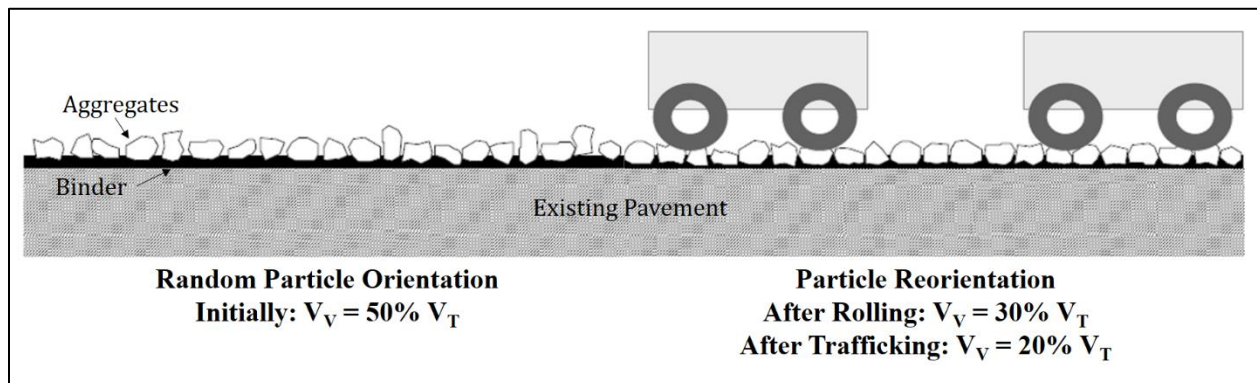


Figure A.5 Change in the proportion of voids with time

Hanson concluded that the BAR is calculated such that 60 to 75% of the ultimate proportion of voids, i.e., 20%, is filled with binder (Gransberg et al., 2005; Hanson, 1935; New Zealand, 2005). After determining the BAR based on the volume of voids in aggregates, Hanson suggested that adjustments should be made to accommodate for the voids in the existing surface texture. Unfortunately, this design method does not provide any recommendations on how to account for them.

Kearby Method; United States, 1953

The Kearby method suggested that the BAR is dependent on the ALD, percentage of voids in the aggregates, the hardness of aggregates, and the voids in the existing surface texture. However, the actual BAR is calculated as a function of the average chip seal layer thickness, the percentage of aggregate embedment, and the percentage of voids in aggregates, which is determined in the laboratory. Kearby did not provide any guidance on how to correct for the voids in the existing surface texture (Kearby, 1953). Instead, visual inspections are required to correct the application

rates based on experience and personal judgement (Gransberg et al., 2005; Senadheera et al., 2000).

McLeod Method; Canada, 1969

McLeod's method first calculates a basic BAR as a function of both the ALD of the aggregates and the volume of voids in them. Accordingly, a correction factor is applied to account for the voids in the existing surface texture. These correction factors are obtained from a table that provides a dosage correction based on a visual rating of the surface texture (McLeod, 1969; Alderson, 2006).

Modified Kearby Method; United States, 1981

Epps et al. modified Kearby's design method by incorporating the correction factors that were missing from the original Kearby method. This design method calculates the voids in the aggregates based on laboratory tests of dry loose unit weight and dry specific gravity. The BAR is determined as a function of the average chip seal layer thickness, the desired embedment depth, and the experimented proportion of voids in the aggregates. Afterwards, empirical corrections for the voids in the existing surface texture are applied (TxDOT, 2017; Epps et al., 1981). Sound engineering judgement is required to provide a description of the existing surface condition and adopt the recommended correction factor.

Australian, British, French, and South African Design Methods; 2005, 2016, 2017, and 2007

The philosophy behind these design methods is that there is a predefined set of AARs and BARs tested to perform well under "benchmarked" site conditions (Alderson, 2006; Bateman, 2016; Institut, 2017; South African, 2007; AFNOR, 2007). Subsequently, corrections are applied to account for differing site-specific conditions including the volume of voids in existing surface texture among others. To estimate the volume of voids in the existing surface texture, the Australians, French and South Africans rely on the mean texture depth (MTD) measured by the SPT (Alderson, 2006; Institut, 2017; South African, 2007); whereas, the British rely on "*a subjective assessment that should be carried out by an experienced person*" (Bateman, 2016). So, it is only in the 2000s that a texture characterization method was incorporated into some seal coat designs.

THE NEED FOR OBJECTIVE QUANTITATIVE METHODS

There is a consensus between different design methods that the voids in the surface texture play a key role in the surface-treatment design methods. Different agencies have attempted to determine the BAR of chip seals based on the volume of voids in the aggregates as represented in Figure A.6a. However, they rely on different subjective methods to estimate the voids in the existing surface texture (illustrated in Figure A.6b) to empirically correct the BARs. As depicted in Figure A.6c, the existing surface texture provides a surplus of voids in excess to those accounted for when considering the aggregate matrix on a flat surface. Some design methods rely on measuring the

MTD obtained from the SPT as an estimate of the volume of voids in the existing surface. Many studies have tested the variability of the SPT and concluded that it is quite variable and operator dependent. The identified variations were mostly caused by human and sampling errors. The findings also indicate that the SPT has a poor repeatability and an even lower reproducibility (El Hachem et al., 2018; Chamberlin et al., 1982). Hence, an operator-independent and objective procedure capable of accurately quantifying the volume of voids in the surface texture is required. Consequently, the measured voids need to be incorporated in the design methods to avoid incorrect estimations of the BAR and, ultimately, a poor chip seal design.

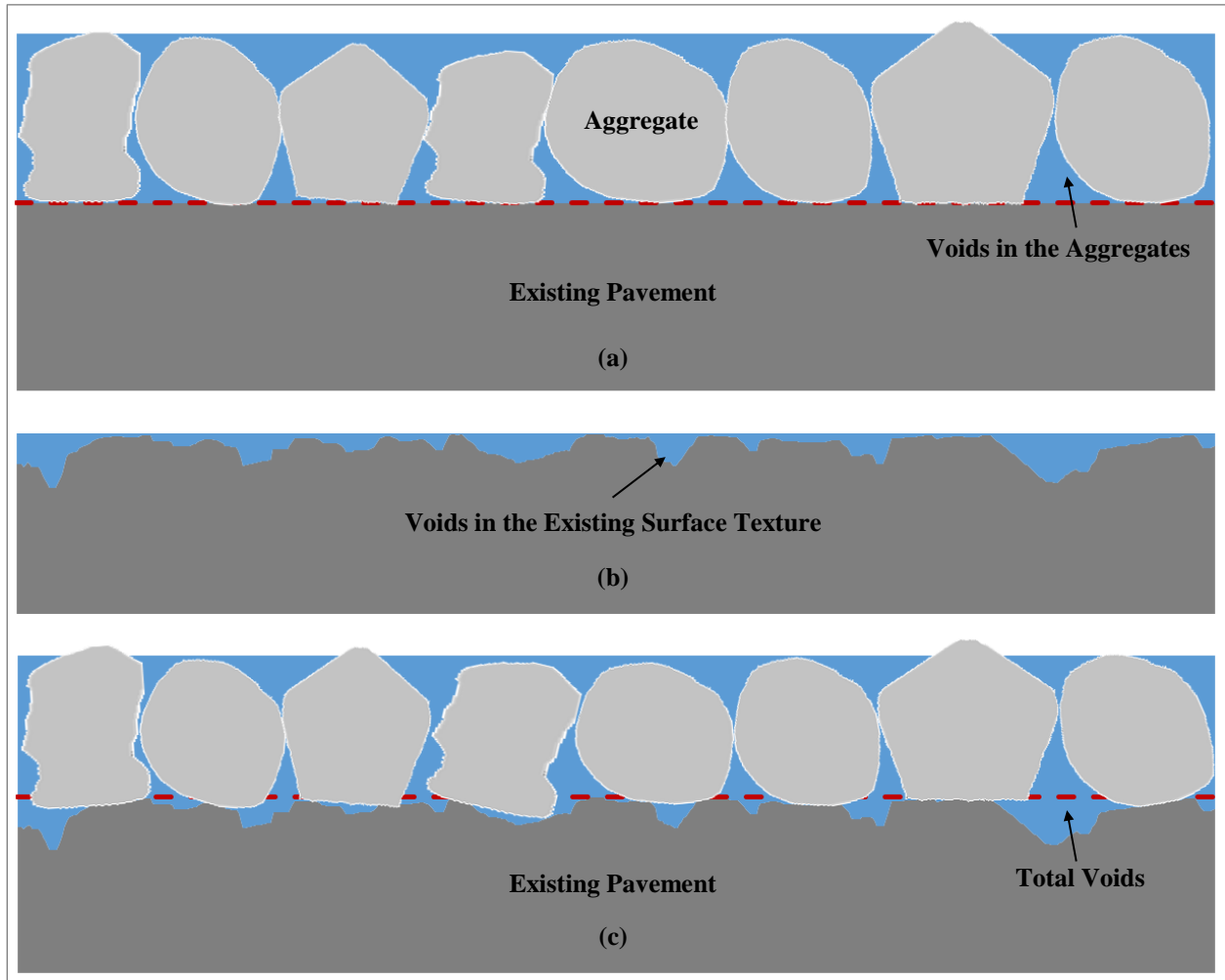


Figure A.6 Voids in the chip seal structure

PROJECT APPROACH

The challenge of designing chip seals has been the reliability of using empirical factors to correct for site-specific conditions, such as the voids in the surface texture, without compromising the performance. With recent advances in the light amplification by stimulated emission of radiation (laser) technology, highway agencies, Departments of Transportations (DOTs), and research

institutes are gearing towards improving and employing such developments that could contribute towards better chip seal designs. The advantage of using laser technology is the ability to capture 3D data of pavement surfaces using a quick, and simple operation. These versatile lasers can be used in both the laboratory and the field for design, quality assurance, and quality control. The goal of this study is to employ the 3D laser scanner (developed at the University of Texas at Austin) to accurately, automatically, and objectively quantify the volume of voids in the existing surface texture and incorporate it in the existing chip seal design methods to improve the BAR calculation. To achieve the goal of this study, the steps, listed below, were required:

- Conducting field tests to collect 3D scans of different pavement sections using the laser system and measure the MTD using the SPT to comply with existing design methods;
- Developing the algorithm that determines the volume of voids in the scanned 3D model of the surface and comparing the results with those of the SPT;
- Adjusting the existing chip seal design methods.

RESEARCH METHODOLOGY

Measurement Process and Testing

This study was conducted on nine pavement sections, each with different mix designs. In each pavement section, two to three locations were selected where a SPT was conducted in accordance with ASTM E956 followed by a laser scan. To limit any bias generated by surface non-homogeneity, the SPT was conducted in the same location as that of the laser scan.

3D Data Filtering

The collected data was filtered to obtain a 3D model relevant to the pavement surface. The filtering process, shown in Figures A.7a to 7d, includes discarding or correcting the dead points, shown in blue, at the ends of the line laser that were not captured by the detector. Afterwards, the slopes in the transverse and longitudinal directions are subtracted. Finally, the noise is removed from the data and a 2D mean filter is applied to correct evident outliers.

Reference Plane and Volume of Voids Philosophy

As mentioned earlier, some design methods adjust the BAR by estimating the volume of voids in the surface texture using the MTD obtained from the SPT (New Zealand, 2005; Alderson, 2006; Institut, 2017; South African, 2007). The MTD provides an average value of the deviations of the pavement surface from a true planar surface (ASTM E956). However, the SPT is a subjective and an operator-dependent test. Thus, previous research attempted to replace the SPT with laser-based devices that eliminate the bias associated with the operator. These studies scanned the pavement surface and demonstrated that a reference point, line, or plane is required for the calculation of the MTD (Hao et al., 2016). For instance, the automatic road analyzer algorithm relies on the maximum point as a reference to estimate the MTD of a road profile (Meegoda, 2002; Fugro, 2017). However, pointing tips, debris, or few large stones can skew the reference point and

overestimate the results. When it comes to chip seal design, the reference plane should mimic the binder flowing over the pavement surface and filling almost all the voids. Since the surface, as shown in Figure A.7a, is not homogeneous, smaller square elements (30 by 30mm [1 in = 25.4mm]) of the surface texture were considered. Each square has its own reference plane based on the data heights contained within it. Figure A.7d displays the 3D scanned surface with one of the square regions for illustration. The square in the picture looks like a rectangle because the two axes have different scales. Note that the size of square elements can be changed to meet the needs of the user and the data at hand. Nevertheless, a sensitivity analysis showed that this specific size was the most adequate for estimating the voids in the surface texture.

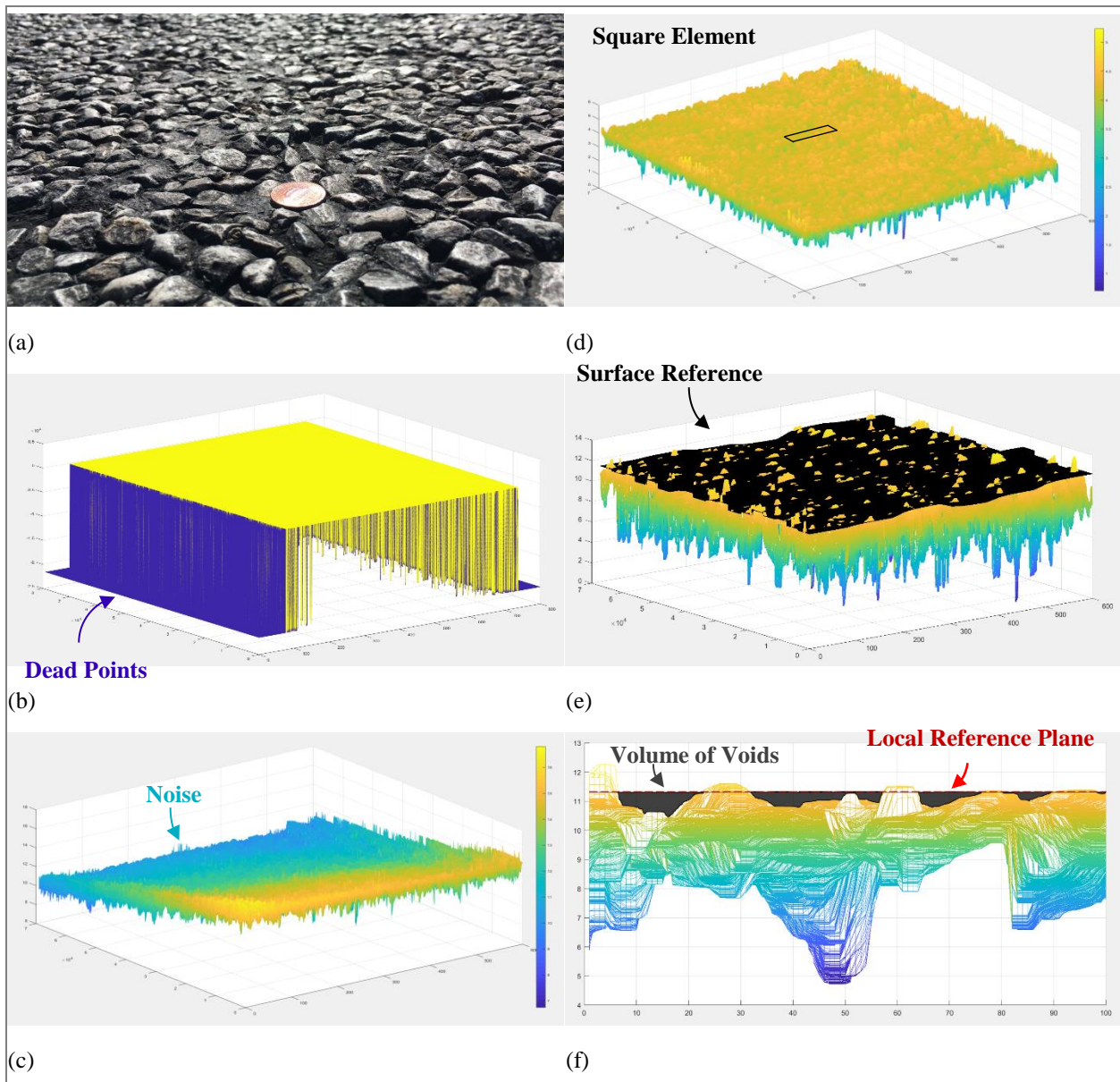


Figure A.7 a) Scanned surface b) Raw data c) Filtered data d) De-trended surface e) Surface with reference plane f) 2D view of the surface texture voids in one square

To calculate the volume of voids, an algorithm was developed. First, the scanned surface is divided into smaller square regions 30 by 30mm. The reference plane for each region is set at different percentiles of the data heights. The distance between the reference plane and each data point below it is calculated. The average depth is determined for the considered square element. The volume of voids in the square element is the product of the square area (30 by 30mm) and the average depth of the scanned surface from its reference plane. The same procedure is reiterated for each square region over the whole scanned area. The total volume of voids in the whole scanned area is the sum of the volume of voids in each individual region. The total volume of voids can then be divided by the total area of the scanned surface to obtain an estimate of the volume of voids per unit area.

RESULTS AND DISCUSSION

Determining the Reference Plane

The purpose behind the reference planes, which are local to each 30 by 30 square, is to calculate the volume of the voids in the existing surface texture and simulate the binder within these voids. Different simulations of the reference planes were performed at different percentiles, and the respective volume of voids were calculated as shown in Table A.3.

Table A.3 Volume of voids in existing surface textures

Test Section	SPT MTD (mm)	Volume of Voids in Texture V_{VES} (L/m ²) with the reference plate at				
		95 th Perc.	96 th Perc.	97 th Perc.	98 th Perc.	99 th Perc.
Speedway (1)	0.64	0.52	0.54	0.57	0.61	0.66
Speedway (2)	0.63	0.52	0.54	0.56	0.59	0.63
FM 1431 (1)	1.24	1.46	1.50	1.55	1.62	1.72
FM 1431 (2)	1.34	1.46	1.50	1.55	1.61	1.70
FM 1431 (3)	1.24	1.60	1.65	1.70	1.77	1.87
FM 1626 (1)	0.75	0.64	0.66	0.69	0.72	0.78
FM 1626 (2)	0.73	0.67	0.69	0.71	0.75	0.80
FM 1626 (3)	0.68	0.69	0.71	0.74	0.78	0.84
IH 20 (1)	2.33	2.62	2.72	2.82	2.93	3.08
IH 20 (2)	2.29	2.33	2.41	2.50	2.61	2.76
IH 20 (3)	2.10	2.57	2.66	2.75	2.88	3.05
RM 12 (1)	0.45	0.39	0.41	0.43	0.46	0.51
RM 12 (2)	0.47	0.39	0.40	0.42	0.45	0.51
RM 12 (3)	0.47	0.39	0.41	0.43	0.46	0.51
SH 36 (1)	2.23	2.27	2.33	2.41	2.51	2.66
SH 36 (2)	2.04	2.21	2.27	2.35	2.45	2.61
SH 36 (3)	2.09	2.34	2.41	2.50	2.61	2.76
SH 195 (1)	1.60	1.39	1.44	1.50	1.58	1.70
SH 195 (2)	1.78	1.50	1.55	1.60	1.67	1.77
SH 195 (3)	2.16	1.59	1.64	1.70	1.78	1.90
US 84 (1)	1.07	0.88	0.94	1.00	1.08	1.18
US 84 (2)	1.18	0.93	0.99	1.06	1.14	1.23
US 84 (3)	1.24	1.02	1.07	1.13	1.21	1.31
US 181 (1)	1.36	1.22	1.26	1.32	1.38	1.46
US 181 (2)	1.33	1.12	1.15	1.20	1.25	1.33
US 181 (3)	1.24	1.29	1.33	1.38	1.44	1.54

By comparing the results obtained by the laser to that estimated using the SPT, it can be observed that there are no evident outliers. Although, the values do not precisely match, they are within the normal variability of the SPT. Unfortunately, there is no research that could be found that focuses on determining the volume of voids in the surface texture to compare the developed model to. Nevertheless, it is worth mentioning that the developed prototype can mimic the flow of binder within the existing surface voids and is highly repeatable and reproducible.

Several graphical representations of the flow of binder on the surface were generated in order to visualize the appropriate reference needed to determine the volume of voids in the existing pavement surface. Figure A.8 shows a side view of the scanned pavement with the reference plane at four different percentile levels of the surface depth. The volume of voids in the surface texture, highlighted in black, is calculated as the volume between the scanned surface and the reference plane. The 98th percentile shows the most promising and consistent plane for simulating the flow of the binder and calculating the volume of voids in the existing surface texture. Hence, the reference plane of the whole scanned surface is the collection of the 98th percentiles of each of these smaller data blocks as represented in Figures A.7d to 7f.

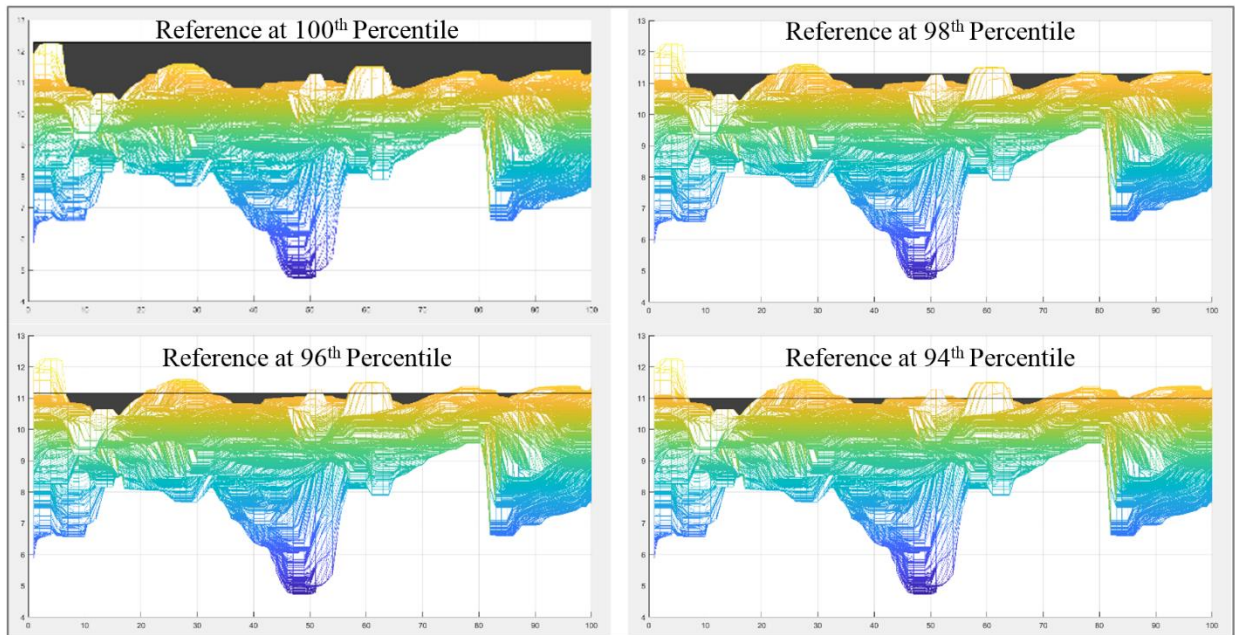


Figure A.8 Simulated texture voids filled by binder up to four different reference planes

Incorporating the Total Volume of Voids in the Existing Design Methods

The performance of the chip seal design is directly related to the adequate estimation of the required BAR and AAR. Almost all the current techniques measure the voids in the aggregate layer, determine the BAR, and correct for voids in the texture. Since the binder is a function of the voids in the chip seal system, the ability to measure the total volume of voids enhances the BAR estimation. At the same time, the existing surface texture is highly variable along both the width and the length of the road section. Conventional methods rely on testing few locations within the job site and applying a one-fits-all BAR. This leaves the rough-textured locations with underestimated binder and the smooth-textured areas with overestimated binder, compromising the performance of the treatment. However, the laser can mitigate this challenge by measuring the texture of the roadway at several, if not all the locations, and modifying the BAR accordingly.

To improve the calculation of the BAR, the measured volume of voids in the existing surface texture should be added to the estimated volume of voids in the aggregate matrix before calculating the BAR. This eliminates the need to empirically correct for the existing surface texture. The following discussion presents the needed modifications to two of the existing design methods, as an example, to better calculate the BAR.

Hanson Design Method

Hanson suggests that the volume of voids in the compacted aggregate matrix occupies 20% of the total compacted volume and is given by:

$$V_{V_{Agg}} = 20\% \text{ of Compacted Aggregate Volume} = 0.2 \times \frac{ALD}{1000} \quad \text{Equation A.2}$$

where $V_{V_{Agg}}$ is the volume of voids in the aggregate matrix in m^3/m^2 , and ALD is the average least dimension of the aggregates in mm.

Note: The compacted aggregate volume has a compacted depth of ALD over an area of $1m^2$.

However, the total volume of voids, $V_{V_{Total}}$, in the chip seal matrix is the sum of the volume of voids in the aggregate matrix, $V_{V_{Agg}}$, and the volume of voids in the existing surface texture, $V_{V_{ES}}$. Hence, the total volume of voids in the chip seal is given by:

$$V_{V_{Total}} = V_{V_{Agg}} + V_{V_{ES}} \quad \text{Equation A.3}$$

Hanson's experience with chip seals has shown that chips will be held in position if the bitumen occupies 70% of the void volume; however, Hanson was not able to account for the volume of voids in the existing surface texture. Instead, the BAR is calculated based on the volume of voids in aggregates. Alternatively, the volume of voids in the existing surface texture can be incorporated in the BAR that is calculated in l/m^2 as:

$$BAR = 0.7 \times V_{V_{Total}} = 0.14 \times ALD + 0.7 \times V_{V_{ES}} \quad \text{Equation A.4}$$

Modified Kearby Method

The modified method of Kearby determines the BAR in gal/yd^2 based on the average mat depth, the desired embedment depth, and the experimented proportion of voids in the aggregates. Consequently, a correction factor for predicted traffic and another factor for volume of voids in existing surface texture are applied as follows:

$$BAR = 5.61E \left(1 - \frac{W}{62.4 \times G} \right) (T) + V \quad \text{Equation A.5}$$

where E is the embedment depth in inches, which is a percentage of the average mat depth d , $\left(1 - \frac{W}{62.4 \times G}\right)$ is the proportion of voids in the aggregate matrix, W is the dry loose unit weight of aggregates, G is the dry bulk specific gravity of aggregates, T is the traffic correction factor, and V is the empirical correction for existing surface texture in gal/yd².

In lieu of the existing method, the total volume of voids can be used to estimate the BAR without the need to empirically correct for the existing surface texture. The proportion of voids in the original equation, (Equation A.4), is relevant to the volume of voids found in the aggregate matrix. This portion of the equation is replaced by a proportion of voids relevant to the whole chip seal system as follows:

$$\text{Proportion of Voids} = 1 - \frac{\text{Volume of Solids}}{\text{Total Volume}} = 1 - \frac{\frac{W}{62.4 \times G} \times d}{d + V_{VES}} = 1 - \left\{ \frac{W}{62.4 \times G} \times \frac{d}{d + V_{VES}} \right\} \quad \text{Equation A.6}$$

Consequently, the BAR is calculated as follows:

$$\text{BAR} = 5.61E \left(1 - \left\{ \frac{W}{62.4 \times G} \times \frac{d}{d + V_{VES}} \right\} \right) (T) \quad \text{Equation A.7}$$

where $\left(1 - \left\{ \frac{W}{62.4 \times G} \times \frac{d}{d + V_{VES}} \right\} \right)$ is the proportion of voids in the entire system.

This proposed design philosophy helps highway agencies and state DOTs to better assess the required BAR and improve the performance of the chip seal system. The ability to incorporate an automated and accurate method of calculating the volume of voids in the existing surface texture (instead of depending on a subjective texture judgement that dictates an empirical correction) is a significant enhancement in the field of pavement preservation in general and chip seal treatments in particular. This enhancement leads to a better design and, consequently, significant savings in taxpayer dollars.

REFERENCES FOR APPENDIX A

- AFNOR. *Surface Dressing Requirements: French European Standard*. Association Francaise de Normalisation, La Plaine Saini-Denis, 2007.
- Alderson, A. *Update of the Austroads Sprayed Seal Design Method*. Austroads Incorporated, Sydney, 2006.
- American Society of Testing and Material. ASTM E956 Standard Test Method for Measuring Pavement Macrotecture Depth Using a Volumetric Technique. ASTM International, West Conshohocken, 2015.

- Anochie-Boateng, J. K., Komba, J. J., and Tutumluer, E. Aggregate surface area quantified through laser measurements for South Africa asphalt mixtures. *Journal of Transportation Engineering*, Vol. 138, 2010, pp. 1006–1015.
- Anochie-Boateng, J. K., Komba, J. J., and Mvelase, G. M. Three-dimensional laser scanning technique to quantify aggregate and ballast shape properties. *Journal of Construction and Building Materials*, Vol. 43, 2013, pp. 389–398.
- Chamberlin, W. P., and Amsler, D. E. *Measuring Surface Texture by the Sand-Patch Method*. American Society for Testing and Material, West Conshohocken, 1982.
- Dumas, B. The determination of the average least dimension of surfacing aggregates by computation. *20th South African Transport Conference*, South Africa, 2001.
- El Hachem, Y. G., Kouchaki, S. and Prozzi, J. A. Assessing the Variability of the Sand Patch Test and Determining the Limitation of its Use. Submitted to the 98th Transportation Research Board 2019 Annual Meeting, Washington, D.C., 2018.
- Elmore, W. E., Solaimanian, M., McGennis, R. B., Phromson, C., and Kennedy, T. W. Performance-based seal coat specifications. Research Report No. 1367-1, Center for Transportation Research, Austin, T.X., 1995.
- Epps, J. A., Gallaway, B. M., and Hughes, C. H. Field Manual on Design and Construction of Seal Coats. Research Report No. 214-25. Texas A&M Transportation Institute, College Station, Texas, 1981.
- Gransberg, D. D., and James, D. B. *Chip Seal Best Practices. NCHRP Synthesis 342*, Transportation Research Board, Washington D.C., 2005.
- Hanson, F. M. *Bituminous Surface Treatment of Rural Highways*. New Zealand Society of Civil Engineers, Wellington, 1935.
- Hao, X., Sha, A., Sun, Z., Li, W., and Zhao, H. Evaluation and Comparison of Real-Time Laser and Electric Sand-Patch Pavement Texture-Depth Measurement Methods. *Journal of Transportation Engineering*, July 2016. Volume 142, Issue 7.
- Islam, M. D. S. *Evaluation of Lightweight Aggregates in Chip Seal*. MSc Thesis, Department of Civil Engineering, Kansas State University, Manhattan, Kansas, 2007.
- Jackson, G. P. *Surface dressing*. Shell International Petroleum Co., London, 1963.
- Masad, E. *The development of a computer controlled Image Analysis System for measuring aggregate shape properties*. Final report, NCHRP-IDEA Project 77. Transportation Research Board of the National Academies, Washington, D.C., 2003.
- McLeod, N. W. *A General Method of Design for Seal Coats and Surface Treatments*. Association of Asphalt Paving Technologists, Toronto, 1969.
- Meegoda, J. N., Rowe, G. M., Hettiarachchi, C. H., Bandara, N. and Sharrock, M. J. *Correlation of Surface Texture, Segregation, and Measurement of Air Voids*. Publication FHWA-NJ-2002-026. FHWA, U.S. Department of Transportation, 2002.
- Mulry, B., K. Feighm, and T. Casey. The use of average least dimension in surface dressing design. *Civil Engineering Research in Ireland*, 2016.

- New Zealand Transport Agency. *Chipsealing in New Zealand*. Transit New Zealand, Road Controlling Authorities & Roading New Zealand, Wellington, 2005.
- Patrick, J. The Evolution of the New Zealand Chip seal Design Methodology. *1st Sprayed Sealing Conference*, Adelaide, Australia, 2008.
- Senadheera, S., Gransberg, D. and Kologlu, T. *Statewide Seal Coat Constructability Review*. Report No. TX-97/0-1787-3. Texas Tech University, Lubbock, Texas, 2000.
- TxDOT. *Seal Coat and Surface Treatment Manual (2017)*. Texas Department of Transportation. <http://onlinemanuals.txdot.gov/txdotmanuals/scm/scm.pdf>. Accessed March 14, 2017.
- TxDOT. *Standard Specifications for the Construction and Maintenance of Highways, Streets, and Bridges*, Texas Department of Transportation, 1995.